TEMPERATURE DEPENDENCE OF THE MAGNETIC EXCITATIONS IN IRON AND NICKEL

A THESIS

Presented to

The Faculty of the Division of Graduate

Studies and Research

By

Jeffrey Whidden Lynn

In Partial Fulfillment

of the Requirements for the Degree

Doctor of Philosophy

in the School of Physics

Georgia Institute of Technology

April 1974

TEMPERATURE DEPENDENCE OF THE MAGNETIC EXCITATIONS

IN IRON AND NICKEL

Approved:

Harold A. Gersch, Chairman

Herbert A. Mook

Robert M. Nicklow

Donald C. O'Shea

Michael K. Wilkinson

Date approved by Chairman: 15 April 1974

ACKNOWLEDGMENTS

The author would like to express his deepest appreciation to Drs. H. A. Mook, R. M. Nicklow, J. F. Cooke and M. K. Wilkinson for their expert professional guidance and personal encouragement during the course of this work, and for the donation of a very generous amount of their time to the author. Sincere appreciation is also extended to Drs. H. G. Smith and H. L. Davis for the consideration given the author during this work. The author would like to especially thank these people for making his stay in Oak Ridge not only professionally very rewarding, but also personally very pleasurable.

The author would like to extend his sincere appreciation for the personal encouragement and expert professional guidance provided by Dr. H. A. Gersch during the entire graduate education of the author. Appreciation is also extended to the Department of Physics of the Georgia Institute of Technology for the financial assistance provided during the early years of the author's graduate studies, and for the consideration extended by Dr. J. R. Stevenson, Director. The author would also like to thank Dr. D. C. O'Shea for serving on the reading committee.

This research was conducted in the Solid State Division of the Oak Ridge National Laboratory operated by Union Carbide Corporation for the U.S. Atomic Energy Commission. The author is grateful for having at his disposal the excellent facilities of the Laboratory and

the scientific expertise of the members of the Solid State Division. The many helpful discussions with the Laboratory personnel are appreciated, in particular those discussions with Drs. N. Wakabayashi, M. E. Mostoller, W. C. Koehler, R. M. Moon, J. W. Cable, H. R. Child and T. Kaplan. The invaluable experimental assistance of Mr. J. L. Sellers is gratefully acknowledged.

The author would like to express his sincere appreciation to his wife, Linda, for her encouragement, assistance, patience and personal sacrifice during the author's entire career in physics.

The author would like to thank Mr. D. L. Holcomb and Mr. A. C. Kimbrough for design and construction of the high temperature vacuum furnace used in these studies.

Special gratitude is extended to Mrs. Ethel Lynn Cagle, whose secretarial skills are obvious throughout this final manuscript. Her patience and helpful suggestions during the painstaking task of preparing the preliminary drafts and the final dissertation are gratefully acknowledged.

While performing this thesis research, the author was an Oak Ridge Associated Universities Graduate Participant from the Georgia Institute of Technology, and the financial assistance provided is gratefully acknowledged.

TABLE OF CONTENTS

TABLE OF CONTENTS (continued)

LIST OF FIGURES

LIST OF FIGURES (continued)

LIST OF FIGURES (continued)

SUMMARY

The coherent magnetic inelastic scattering of neutrons has been used to measure the magnetic excitations in iron and nickel from low temperatures to well above the ferromagnetic transition temperatures. In contrast to the behavior observed in the small wavevector region, where the spin waves were found to become overcritically damped just below T_C, the spin waves at larger values of $\vec{q}$ are found to persist as well defined excitations up to the highest temperatures measured (1.4 T_C for iron and 2.0 T_C for nickel). The dispersion relations are only moderately renormalized up to T_C, and then remain constant as the temperature is increased further. The overall spin wave intensities are reduced at higher temperatures, but the abrupt decrease in the spin wave intensity at high energies, interpreted as the intersection of the spin wave spectrum with the Stoner continuum band of spin-flip excitations, is found to be insensitive to the temperature. Measurements of the linewidths show that the spin waves do broaden considerably as the temperature is raised to T_C. Above T_C, they continue to broaden slowly in nickel, while in iron they show no additional broadening. The spin wave energies and lifetimes are found to be isotropic in $\vec{q}$ over the entire temperature range covered, and no interaction of the spin waves with the phonons is observed.

The experimental results for nickel at low temperatures are best described by calculations of the generalized susceptibility based on

band structures in which the electron correlations are treated as accurately as possible. The correlations in iron are more difficult to handle, and calculations of the density of Stoner spin-flip excitations have been performed which indicate that in order to explain on a quantitative basis the disappearance of the spin wave modes in iron the band splitting will need to be reduced from the values that have been obtained from band structure calculations.

Calculations of the temperature dependence of the generalized susceptibility are much more difficult to do. The general procedure has been to use a molecular field approximation for the band structure, in which the band splitting is set proportional to the magnetization. The temperature dependent results for iron and nickel indicate that this is not even qualitatively correct. The electron correlations at elevated temperatures will need to be incorporated into the theory more accurately in order to produce the strong short range spin correlations necessary to support propagating modes above the ferromagnetic transition temperature. Clearly more theoretical effort will be needed in order to bring theory into agreement with experiment.

CHAPTER I

INTRODUCTION

The magnetism of solids arises from the "uncompensated" spin and orbital magnetic moments of the electrons. These "magnetic" electrons reside in partly occupied energy bands, or "shells" of atoms, which are often the highest occupied energy states in the solid. Thus these electrons may also contribute to the binding energy and bulk thermodynamic properties of the solid. An understanding of the origin of their magnetic behavior can therefore lead not only to an understanding of magnetism itself, but also to other solid state properties of fundamental and technological importance.

The quantity of interest in understanding these magnetic systems is the wavevector and frequency dependent generalized magnetic susceptibility $\chi(\vec{K},\omega)$. This is because with a knowledge of $\chi(\vec{K},\omega)$ the response of the system to any magnetic disturbance can be found, so that χ contains a complete description of the magnetic properties of a system. $\chi(\vec{K},\omega)$ is directly related to the coherent inelastic scattering of neutrons, which in fact is the only experimental technique available to measure the general wavevector and frequency dependence of the susceptibility. Thus neutron scattering gives fundamental information about the system which can be obtained with no other method. The study reported here is concerned with measuring the temperature dependence of

the generalized susceptibility of iron and nickel using the neutron coherent inelastic scattering technique.

Localized Versus Itinerant Models of Magnetism

Since the source of the magnetism in solids is the electrons, theories of magnetism are based on calculations of the quantum states of the electrons in a solid. Of course, the underlying physical principle which correlates the space and spin distributions of the electrons, the Pauli exclusion principle, is the same for all models of magnetism. However, two contrasting viewpoints concerning the types of states the magnetic electrons occupy have been used over the years as bases for these models of magnetism.[1] One viewpoint is that the electrons that give rise to the magnetism are localized on atomic sites. They are then Hund's Rule coupled to give a localized magnetic moment, which then couples to moments on other sites via a direct or indirect exchange interaction. The alternate view (for metals) is that the magnetic electrons spend relatively little time on any particular site, undergoing band motion, but in a highly correlated manner. The magnetism then results from the electron-electron spin correlations produced by their mutual Coulomb interactions. Of course, the models which are now categorized as localized or itinerant have been greatly modified and generalized from the original models introduced by Heisenberg and Bloch. Still a first-principles explanation of ferromagnetism remains as one of the most challenging many-body problems in solid state physics.

3d Metals

Since these models are conceptually quite different, it might appear at first that it would be relatively easy to choose the most appropriate one for the 3d transition metals. However, experiments show that the d-electrons appear in some cases to be well localized and in other cases itinerant. For example, the static paramagnetic susceptibilities are strongly temperature dependent, the spatial distributions of the magnetic moments in both the ferromagnetic[2-4] and paramagnetic[5-7] phases are similar to 3d free-atom electron distributions, and distinct spin waves having many of the properties of a Heisenberg ferromagnet are observed in these metals.[8] On the other hand, the number of unpaired electrons per atom is far from an integral number, and these "magnetic" electrons also contribute to the electrical conductivity and low temperature specific heat. Furthermore, measurements of the Fermi surfaces[9-15] show they have rather complicated structures which are in general agreement with band structure calculations.

These opposing attributes can be reconciled with each other by considering the electrons as undergoing a highly correlated band motion, with the spin correlations arising in the following manner.[16] Since the charge distribution of a d-electron is fairly compact, there is some meaning in considering a d-electron as "on" an atom at a particular time. Suppose we have a partly filled d-band of noninteracting electrons,* and "watch" the total spin of an atom. As a function of time

*If the band is more than half full, we really need to consider "holes" instead of electrons.

the spin will fluctuate randomly both in magnitude and direction as the electrons "hop" on and off the atom, the hopping time being roughly of the order of $\hbar/\Delta$, where Δ is the d-electron bandwidth. If the electron interactions are turned on, we can use Hund's Rule as a guide to see that the mutual intra-atomic interactions tend to produce correlations favoring alignment of the electron spins. Suppose an atom has at some instant a net spin direction. Then as the electrons undergo their band motion, the atom will tend to favor replacing an electron which hops off it by another electron with the same spin direction, to preserve the atom's net spin. Hence the spin alignment will tend to be self-perpetuating, so that if the correlations are strong enough the spin state will persist for a time which is long compared to the hopping time of the d-electrons. Thus we may be able to associate a net spin with the atom rather than accounting for each individual electron spin, and the possibility of a localized description becomes apparent. These localized properties may be particularly apparent in experiments which involve measuring-times which are long compared to the d-electron hopping time, or which average over a large spatial region.

Previous Experiments on Iron and Nickel

The magnetic properties of iron and nickel have been under intensive investigation for many years. In fact, they have probably been studied by more researchers and with a wider variety of techniques than any other magnetic materials. The experimental evidence strongly favors the view that the d-electrons in these metals occupy relatively narrow energy bands which are itinerant in character, although the strong electron correlations present give rise to some properties which are similar

to the behavior of localized moments. Many of these experiments have been performed with the idea of determining the appropriateness of various models which are either itinerant or localized in character. In addition to the examples already discussed, there are a few recent experiments which should be described in more detail.

Wohlfarth[17] has pointed out that the high-field behavior of the magnetic moments should lead to a clear distinction between the localized and itinerant models. At low temperatures, the high-field static susceptibility should approach zero if the moments are localized, since the magnetic system will become completely saturated. However, if the spin-up and spin-down bands in the band model are both only partially occupied, a finite susceptibility should be observed well above technical saturation. The high field magnetization measurements of Foner et al.,[18] favor the itinerant model.

The spin polarization of electrons near the Fermi surface has been measured by photoemission,[19] field emission,[20] and tunneling[21] experiments. The most naive expectation is that the polarization measured in these experiments should be directly proportional to the polarization of the band-theoretical density of states at the Fermi energy. For Co and Ni the spin polarization of the calculated density of states is negative at E_F, whereas for Fe it is positive. The photoemission and tunneling experiments (on thin films) measured a positive (majority spin electrons predominating) polarization for Fe, Co, and Ni, and this was taken as evidence against the applicability of the Stoner-Wohlfarth-Slater band model. However, the field emission experiments made on a

single crystal of Ni showed a strong directional dependence to the polarization, being positive in the [111] crystallographic direction and negative in the [100], [110] and [137] directions. The polarization from a polycrystalline sample was negative and it was thus argued that the discrepancy with the photoemission and tunneling experiments could be caused by preferred orientation in the films. This speculation was enhanced by the fact that the measured polarizations in the latter experiments depended on the method of film preparation.

Of course, there is no reason to believe that the polarization of the electrons escaping from a ferromagnetic metal should really be proportional to the density of quasi-electron states at E_F. This would have to mean (among other things) that the matrix elements coupling the initial and final states do not depend significantly on the wave functions of those states, and that many-body effects are negligible. Hertz and Aoi[22] have found that these effects can dominate the tunneling measurements, and in fact obtain good agreement with the data when these effects are included. The calculations of Politzer and Cutler[23] agree in sign and magnitude with the field emission measurements, and Smith and Traum[24] were able to obtain the proper sign, but not the right magnitude, for the polarization of the photoemitted electrons from Ni. It is becoming evident that many-body effects may well be important for these types of experiments.[25]

The energy distributions of photoemitted electrons from iron[26,27] and nickel[28,29] have also been studied as a function of temperature. These measurements have been compared to band structure calculations in

which the temperature dependence was introduced by setting the splitting between up- and down-spin bands proportional to the magnetization. For nickel the observed effects were smaller than the calculated results, whereas for iron the results varied from "excellent numerical agreement" with the band theory to very poor agreement. Unfortunately, in comparing experiment with theory a number of approximations have been made. Once again the matrix elements are assumed constant and many-body effects are neglected, so that the energy distribution of photoexcited electrons is directly related to the joint density of initial and final states. This can then be calculated from some appropriate ferromagnetic band structure. To get the energy distribution of photoemitted electrons, a classical scattering probability for the electrons to travel to the surface is assumed, as well as a semi-classical threshold function for escape through the surface. This result must then be convoluted with the experimental resolution function for comparison with the observations. Finally, the procedure is repeated with a paramagnetic band structure to compare with the ferromagnetic results. The paramagnetic calculations are made by setting the splitting between up- and down-spin bands equal to zero. This is an important assumption since with no band splitting above T_C (even a "local" band splitting) there is no allowance for any electron spin correlations. However, our own results show that there are spin correlations above T_C, strong enough in fact to support spin waves. These short-range spin correlations exist for times which are long compared to the time it takes to excite an electron in a photoemission process. It is therefore not clear that much difference should

be expected between the "snap-shot picture" a photon takes at low temperatures and the "picture" taken above the transition temperature, particularly if many-body effects are indeed important.

Neutron Scattering from Magnetic Systems

Before discussing the measurements already made on iron and nickel, it will be worthwhile to briefly outline the main features expected for the inelastic magnetic scattering of neutrons.[30]

General Features

If a small sinusoidally varying magnetic field $H(\vec{K},\omega)$ of wavevector $\vec{K}$ and frequency ω is applied to a system, the magnetic linear response $M(\vec{K},\omega)$ of the system is given by

$$M(\vec{K},\omega) = \chi(\vec{K},\omega)\ H(\vec{K},\omega)\ , \qquad (1)$$

where $\chi(\vec{K},\omega)$ is the wavevector and frequency dependent generalized (dynamic) susceptibility. Any magnetic perturbation imposed upon a system can be represented as a series of Fourier components $H(\vec{K},\omega)$. The magnetic scattering of a neutron, though, corresponds to a disturbance of a single wavevector and frequency. Fortuitously, for neutrons with wavelengths comparable to the interatomic spacings in solids, the neutron energies are comparable to the energies of the elementary excitations usually encountered in solids. Thus the full wavevector and frequency dependence of $\chi(\vec{K},\omega)$ can be obtained by neutron scattering via a direct measurement of $M(\vec{K},\omega)$.

In order to compare theory and experiment, then, a calculation of the susceptibility $\chi(\vec{K},\omega)$ is needed. As a simple example, consider the nearest-neighbor isotropic Heisenberg ferromagnet at T = 0°K. The elementary excitations in this case are the well-known spin waves with a dispersion relation $\omega_{\vec{q}}$ given by (cubic lattice)

$$\hbar\omega_{\vec{q}} = 2zJS\left(1 - \frac{1}{z}\sum_{\vec{\delta}} e^{i\vec{q}\cdot\vec{\delta}}\right), \tag{2}$$

where z is the number of nearest-neighbors located at positions $\vec{\delta}$, S is the atomic spin, J is the exchange constant, and $\vec{q}$ is the wavevector of the spin wave. The dynamic susceptibility is then

$$\chi(\vec{K},\omega) \sim \frac{1}{\omega - \omega_{\vec{q}}}, \tag{3}$$

so that a resonant response of the system occurs only when the wavevector* and energy change of the neutron corresponds to a pole in the susceptibility. This pole corresponds to the creation of a spin wave, which is, of course, the only way the system can gain energy.

For an itinerant electron ferromagnet the magnetic excitation spectrum can be considerably more complicated than for the simple

*Here $\vec{q}$ and $\vec{K}$ are related by $\vec{K} = \vec{\tau} + \vec{q}$, where $\vec{\tau}$ is the reciprocal lattice vector which brings $\vec{q}$ into the first Brillouin zone.

Heisenberg ferromagnet just considered. One reason for these complications is that in the localized system the total spin angular momentum on a site, $\vec{S}_j$, is determined by the strong Hund's Rule coupling present, so that $(\vec{S}_j)^2 = S(S + 1)$ is a constant of the motion. The spin wave states are made up from linear combinations of the states of S_j^z (j = 1, ..., N). For an itinerant system, however, the intra-atomic coupling is not strong enough to give a total $\vec{S}_j$ on a site, so that the remaining states of different total angular momentum cannot be removed from the calculation. In general, however, all isotropic ferromagnets[31,32] have an acoustic spin wave mode at long wavelengths (small $\vec{q}$) with a dispersion relation given by

$$\hbar\omega_{\vec{q}} = D|\vec{q}|^2 \tag{4}$$

(for small $\vec{q}$, equation 2 yields $D = 2JSa^2$, where a is the lattice parameter). At higher energies and larger $\vec{q}$ there can also be other excitations in an itinerant system, for example optical spin wave modes (even when there is only one magnetic atom per unit cell) and single particle (spin-flip) Stoner excitations. These excitations may in fact overlap and interact with each other. For instance, the acoustic spin wave mode may not exist over the entire Brillouin zone, in contrast to the localized model. This can happen if it enters a region of high density of Stoner excitations, where it will become strongly damped and disappear.

At elevated temperatures the theoretical problems become even more complicated. Generally, one expects that the spin wave energies

should decrease (renormalize) and the linewidths increase with increasing temperature. The Stoner-type excitations should also lower in energy as the band spin-splitting collapses. At long wavelengths, of course, the spin waves should become overcritically damped as the temperature passes through T_C. However, the general behavior of $\chi(\vec{K},\omega)$ as a function of temperature is unknown.

Neutron Scattering Experiments on Iron and Nickel

The magnetic scattering of thermal neutrons has been used extensively to study the properties of the magnetic moments in iron and nickel. The techniques of small angle scattering, diffuse scattering, and the "diffraction method" have been used to measure the long wavelength spin dynamics.[33-59] From these experiments it was inferred that the low temperature dispersion relations are isotropic in $\vec{q}$, with the dispersion relation being given approximately by equation 4. Above T_C, considerable information was obtained about the nature of the diffusive modes, as well as revealing the presence of strong short-range spin correlations. Unfortunately, however, the interpretation of these types of experiments, in which the direction but not the energy of the scattered neutron is measured, depends on a number of assumptions.

With the advent of high-flux reactors, $\chi(\vec{K},\omega)$ could be determined directly. Collins et al.[60] (for Fe) and Minkiewicz et al.[61] (for Ni) used the triple-axis technique to measure the critical scattering in detail. They found that in the small wavevector region the spin dynamics are well described by the dynamic scaling theory,[62] except for the spin diffusion constant Λ.[63] The spin wave stiffness parameter

D(T) was found to follow a power law of the reduced temperature, with the spin waves becoming overcritically damped just below T_C. However, no central diffusive mode was observed below T_C, in contrast to some antiferromagnets, and there was evidence in iron that a highly damped propagating mode existed in the "transition" region. Borankay and Collins[64] extended the iron measurements to higher values of $\vec{q}$. They found that the spin wave damping was in excellent agreement with dynamic scaling theory, except at the highest wavevector measured (0.26 Å^{-1}). The damping there was anomalous, and this anomaly was tentatively attributed to a conduction electron screening effect.

Lowde, Windsor and collaborators[65,66] have made temperature dependent measurements of the scattering in nickel using the neutron time-of-flight method, and their results have served as a first step in the overall determination of $\chi(\vec{K},\omega)$ for nickel. They found that away from the immediate vicinity of the critical region the scattering evolved smoothly through the Curie point and that above T_C there was a "hump" of scattering, indicative of short range correlations. This "hump" evolved into the limiting form of paramagnetic scattering at higher temperatures ($\sim 2\ T_C$). Unfortunately, they were unable to employ sufficient resolution while retaining enough neutron intensity to obtain a clear picture of the scattering, particularly at the higher energies and higher temperatures.

In addition to these temperature dependent measurements, the spin wave part of $\chi(\vec{K},\omega)$ has been measured at room temperature in detail. However, the magnon dispersion relations in the 3d metals are

very steep, so that at larger wavevectors the magnon energies become rather high for neutron scattering techniques to measure. The problem is that the flux of thermal neutrons in the reactor is approximately given by a Maxwell distribution, with a peak at ∿30 meV. The flux therefore falls off rapidly at higher neutron energies and this makes measurements of the high energy spin waves difficult. Collins et al., and Minkiewicz et al., measured a portion of the dispersion relations and found that the spin waves were isotropic in $\vec{q}$ up to the highest energy transfers they could measure (∿70 meV). This energy corresponded to a $\vec{q}$ vector which was about 40% of the zone boundary $\vec{q}$ vector in Fe, and 27% for Ni. Approximating the dispersion relation in this wavevector region by

$$\hbar\omega_{\vec{q}} = D|q|^2 (1 - \beta|q|^2) \qquad (5)$$

they found values of D = 280 meV-Å^2 and β = 0.96 Å^2 for Fe, and D = 400 meV-Å^2 and β = ∿-10.5 Å^2 for Ni. They concluded that for the Heisenberg model to fit the data the exchange interaction would have to be of very long range. For Ni the quartic term is positive rather than negative, and the fit with equation 5 was not particularly good. In fact, to get good agreement with the data the expansion had to be carried out to powers of q^{10}.

Mook, Nicklow and collaborators were able to extend the room temperature spin wave measurements for iron[67] and nickel[68] to higher energies. As the dispersion curves were followed to higher energies

they found that the spin wave intensities were roughly constant until about 100 meV, and then dropped suddenly by more than an order of magnitude. The fall off in intensity occurred at different energies in different symmetry directions in the crystals, and was interpreted as the intersection of the spin wave modes with the Stoner continuum band of excitations.

With increasing temperature it was expected that the splitting between the spin-up and spin-down electron energy bands would vary in a manner proportional to the magnetization, and hence the region of high density of Stoner states would decrease in energy. In order to check this conjecture, a study of the spin wave spectrum of nickel as a function of temperature was undertaken.[69] It was rather surprising to find that not only did well defined spin wave excitations exist above the ferromagnetic transition temperature, but that the energy at which the spin wave mode disappeared was temperature independent. In fact, except for very small wavevectors the whole spin wave spectrum changed remarkably little between 4.2° and 715°K, which is 86° above T_C.

In view of these rather interesting results, it was clear that a comprehensive investigation of the temperature dependence of the spin waves in the ferromagnetic 3d metals would be profitable. The present studies were therefore carried out with the following objectives in mind.

1) The original nickel measurements could not be carried to higher temperatures because of the limitations of the furnace. Hence there was no indication of how, or if, the scattering would transform

into the limiting form of the paramagnetic scattering expected at very high temperatures. It would therefore be of interest to extend the measurements to higher temperatures.

2) There were also no measurements made with sufficient resolution to enable accurate determinations of the spin wave linewidths in nickel as a function of temperature. In particular, it was unclear how the scattering at higher wavevectors, where there are well-defined spin wave excitations above T_C, would evolve into the overcritically damped behavior found at small wavevectors. The higher temperature measurements at intermediate energies were also complicated by the overlapping of the spin waves with each other and with the phonons. It would consequently take thorough measurements with good resolution to sort out the scattering that was solely of magnetic origin as a function of energy, wavevector and temperature.

3) Of course, there was no way of knowing if the magnetic excitations in the other 3d ferromagnetic metals would show similar behavior, or whether the results found were just an anomalous property of nickel itself. It would therefore be appealing to carry out measurements for iron and cobalt. Unfortunately, cobalt has a large incoherent scattering cross section and a large absorption cross section for thermal neutrons, which make inelastic scattering experiments very difficult even at low temperatures. More importantly, it undergoes a hcp to fcc phase transformation at $\sim$675°K, which is well below T_C ($\sim$1390°K). If a single crystal is heated through the solid-state transformation it is destroyed. Hence a single crystal would have to be grown and kept at high temperatures in order to measure the dispersion curves at elevated temperatures.

The neutron scattering properties of iron are much more favorable. However, it also undergoes a solid-state phase transformation at ∿1185°K, (bcc → fcc), but this is above T_C (∿1042°K). With the addition of $\gtrsim$4% silicon the high temperature transformation is by-passed, thus allowing the growth of a large single crystal from the melt, as well as permitting measurements of the spin waves at high temperatures. Most of the measurements reported here for iron were in fact taken on a single crystal of ^{54}Fe(12% Si), although a limited set of data was also obtained with a pure iron single crystal.

4) Calculations of the dynamic susceptibility for itinerant electron ferromagnets are very difficult to carry out quantitatively for physically realistic systems. The low temperature calculations of Cooke and Davis[70,71] for nickel are the most ambitious to date. Their theory includes momentum-dependent spin splitting of the electronic energy bands as well as multi-band effects. The theory is too difficult to treat analytically, and therefore extensive computer calculations are required to obtain numerical results. The overall agreement between theory and experiment gives us confidence that the description of the excitation spectrum based on band structure models is at least qualitatively correct and that the agreement can be improved as the electron interactions are treated to better approximation. Since there were no "realsitic" results of $\chi(\vec{K},\omega)$ available for iron, these calculations were extended to the case of iron. These efforts have been made in collaboration with J. F. Cooke and H. L. Davis as part of an extended program on the calculation of the dynamic susceptibility of itinerant

electron systems, and therefore an exhaustive report of the results will not be given here.

CHAPTER II

THEORY

General Considerations

In order to calculate the response of a solid to an external magnetic perturbation, one needs to know the initial state of the system, the perturbing Hamiltonian, and all the many-body eigenfunctions and eigenvalues of the system. Of course, this is far too ambitious a task, and the general procedure is to first approximate the many-body wave functions by products of single particle wave functions. To begin the model of the solid, we first solve the free-atom problem for the single particle electron energies and eigenfunctions. We can then usually separate these atomic electrons into two groups, the core electrons, which will not be modified significantly (for most purposes) when put into a solid, and the "valence" electrons, which may be considerably modified when placed into a periodic lattice.

The localized and itinerant models basically differ in the treatment of these valence electrons. If the "magnetic" electrons are localized on atomic sites, then the procedure for handling the correlation of these electrons can usually be greatly simplified. First we solve for the electron states on a single site, taking into account the effects of the remainder of the crystal in an average sense via crystalline electric- and/or magnetic (molecular) fields. The low-lying

magnetic excitations of the system (for example, spin waves or crystal field levels) can then be obtained by assuming a weak magnetic coupling between the atoms. If the ground state happens to correspond to a particular value of the total angular momentum J that is well separated in energy from other states of total J, then models such as the Heisenberg model are appropriate.

When the magnetic electrons are not localized, then the simplifications resulting from the localized moment concept are no longer applicable. The alternate approach (for metals) which has been used is the energy band theory, in which the electrons propagate through the crystal in the periodic potential of the ion cores and the average potential of the "valence" electrons. Properties such as the d-electron electrical conductivity and specific heat, and the non-integral magnetic moments per atom, can be explained in a natural way with this model. However, the collective properties of the system, such as spin waves, are much more difficult to calculate in the band model.[72] The spin wave state is one in which the spin density at one point in space and time is correlated with the spin density at another point. For the localized model this correlation is easily achieved, both mathematically and conceptually, by phasing the rotation of the spin vector on one atom with the rotations on neighboring atoms. For the band model, on the other hand, the spin motion of the electrons must be combined with the translational motion in such a way that the collective spin motion of all the electrons at one point in space is correlated with the motion at another point. These correlation effects produce an effective spin

dependence of the electronic energies and wavefunctions, and hence a stable magnetization density. A magnetic excitation then corresponds to exciting an electron from a single particle state $(\vec{k},\sigma)$ to a state $(\vec{k} + \vec{q}, -\sigma)$. Due to the correlation effects, however, this electron will feel an attraction for the hole that was created, and if the attraction is strong enough they can form a bound state. The spin wave in the band model corresponds to this bound electron-hole pair which propagates through the lattice.

In the early band models, however, there were no spin waves, and their absence was regarded as a serious drawback. In the original Stoner model, for example, the electrons were assumed to occupy spin-up and spin-down energy bands which were rigidly split apart (equivalent to a Weiss molecular field). The only magnetic excitations were single particle electron excitations from one spin band to another band of reversed spin. These spin-flip "Stoner excitations" have energies $\varepsilon_s(\vec{q})$ given by

$$\varepsilon_s(\vec{q}) = \varepsilon_{\pm\sigma}(\vec{k} + \vec{q}) - \varepsilon_{\mp\sigma}(\vec{k}) \quad . \tag{6}$$

It was shown subsequently,[73] however, that spin waves arise quite naturally in the itinerant model by including electron correlations in the theory. Just as spin waves in the Heisenberg model are obtained by taking linear combinations of atomic spin operators, spin waves in the band model can be constructed from linear combinations of Bloch states.[74] Furthermore, Izuyama, Kim and Kubo[75] showed that the itinerant model was

capable of explaining a variety of neutron scattering phenomena, such as diffuse magnetic scattering below T_C, magnetic critical scattering around T_C, and paramagnetic scattering above T_C, that were assumed to be describable only in terms of localized models. In fact, even detailed studies of critical exponents for ferromagnets[62,76] do not seem to be able to provide a clear distinction between different mechanisms of magnetism. It is apparent that it will be difficult to discriminate between the localized and itinerant models on the basis of the long wavelength spin dynamics.

As discussed in the introduction, it is now generally accepted that the 3d electrons in iron and nickel occupy relatively narrow energy bands, so that the magnetic electrons are (at least to some degree) itinerant in nature. Since the excitation spectrum and general features of the inelastic neutron scattering for itinerant electron systems are not as widely known as those for the localized model, a somewhat detailed discussion of the neutron scattering expected from itinerant electron ferromagnets will be given. The tight-binding (narrow-band) approximation will be introduced and the general features of the scattering demonstrated by a simple single band model. The results of the calculation of $\chi(\vec{K},\omega)$ for iron will then be presented.

Neutron Scattering from Itinerant Electron Ferromagnets

By virtue of its magnetic moment, a neutron will interact with both the ("uncompensated") spin of the electrons and their orbital currents. For iron and nickel the orbital contribution to the magnetization is $\sim$5%, which is nevertheless easily measured in elastic scattering

experiments with polarized neutrons. However, the present experiments are concerned with the magnetic inelastic scattering. Lovesey and Windsor[77] have shown that the orbital contribution to the susceptibility at very high energy and large momentum transfers can be comparable to the spin part, but for the regions in which we are interested the orbital contribution can probably be safely neglected. We will therefore simplify the discussion by considering only the spin contribution to the magnetic scattering. In addition, all of the present experiments have been performed with an unpolarized neutron beam incident upon an unmagnetized sample. These assumptions will also be incorporated.

The spin-only magnetic cross section for unpolarized neutrons is given by[78]

$$\frac{d^2\sigma}{d\Omega d\omega} = \left(\frac{\gamma e^2}{m_e c^2}\right)^2 \frac{k'}{k} \sum_{\alpha,\beta} (\delta_{\alpha,\beta} - e_\alpha e_\beta) \frac{1}{2\pi} \tag{7}$$

$$\times \int_{-\infty}^{\infty} e^{-i\omega t} < \mathcal{S}^\alpha(\vec{K},0)\mathcal{S}^\beta(-\vec{K},t) > dt \ ,$$

where k and k' are the magnitudes of the incident and scattered neutron wavevectors, $\hbar\vec{K} = \hbar\vec{k} - \hbar\vec{k}'$ is the momentum the crystal receives from the neutron, $\vec{e}$ is a unit scattering vector ($\vec{e} = \vec{K}/|\vec{K}|$), $\hbar\omega$ is the energy gained by the crystal, γ is the gyromagnetic ratio of the neutron, m_e and e are the mass and charge of an electron, $<\cdots>$ represents the

thermal average, and α,β denote x,y,z. We see that the magnetic inelastic scattering is a direct measure of the time dependent spin correlations of the electrons. The operator $\delta^{\alpha}(\vec{K})$ (at time t) is the Fourier transform of the spin density operator;

$$\hat{\delta}^{\alpha}(\vec{K}) = \int e^{-i\vec{K}\cdot\vec{r}}\ \hat{s}^{\alpha}(\vec{r})\ d\vec{r} \qquad \alpha = x,y,z \tag{8}$$

where

$$\hat{s}(\vec{r}) = \sum_{i} \delta(\vec{r} - \vec{r}_{i})\ \hat{s}_{i} \tag{9}$$

and $\hat{s}_{i}$ is the spin operator for the i^{th} electron. In terms of the second quantized formalism this can be written as

$$\hat{\delta}(\vec{r}) = \psi^{\dagger}(\vec{r})\ \hat{s}\ \psi(\vec{r})\ , \tag{10}$$

where $\psi^{\dagger}(\vec{r})$ and $\psi(\vec{r})$ are the electron creation and destruction field operators, respectively.

Some general features of the scattering can be discerned from equation 7. If the raising and lowering operators

$$\delta^{\pm}(\vec{K}) = \delta^{x}(\vec{K}) \pm i\delta^{y}(\vec{K}) \tag{11}$$

are introduced, the cross section can be rewritten in terms of only three independent correlation functions;

$$\frac{d^2\sigma}{d\Omega d\omega} = \left(\frac{\gamma e^2}{m_e c^2}\right)^2 \frac{k'}{k} \frac{1}{2\pi} \int_{-\infty}^{\infty} e^{-i\omega t} \left[(1 - \kappa_z^2) < \delta^z(\vec{K},0)\delta^z(-\vec{K},t) > \right. \tag{12}$$

$$\left. + \frac{1}{4}(1 + \kappa_z^2) < \delta^+(\vec{K},0)\delta^-(-\vec{K},t) + \delta^-(\vec{K},0)\delta^+(-\vec{K},t) > \right]$$

where κ_z is the component of the vector $\vec{e}$ along the magnetization direction. There are two types of contributions to the inelastic scattering, spin-flip and non-spin-flip scattering. The $< \delta^z\delta^z >$ part of the scattering does not involve the flip of the neutron spin, and at low temperatures it is very small compared to the spin-flip cross section (because the magnet is saturated). However, it should be kept in mind that as the temperature is raised the $< \delta^z\delta^z >$ part of the scattering becomes larger, and for an isotropic ferromagnet above the transition temperature all three correlation functions will be equal, since there is no preferred direction remaining in the crystal. Note also that the $< \delta^z\delta^z >$ scattering can be eliminated if a magnetic field is oriented along the scattering vector.

The $< \delta^{\pm}\delta^{\mp} >$ correlations give rise to the spin-flip scattering, which includes the inelastic scattering of neutrons by spin waves and the Stoner modes. The spin-flip scattering can be varied by a magnetic field, but it cannot be eliminated.

Finally, for an unmagnetized sample, the cross section has to be averaged over all directions of the magnetization. For a cubic crystal this yields a value of $\kappa_z^2 = 1/3$.

Spin Deviation Operator

Since itinerant electron systems are considerably more complicated to deal with mathematically than localized systems, it may be enlightening to study the operator which creates a spin deviation in the system, and see how this operator can be simplified to the Heisenberg spin deviation operator with the appropriate approximations.[79]

If the field operators in equation 10 are expressed in terms of Bloch states, then

$$\hat{s}(\vec{r}) = \sum_{\substack{n,\vec{k},\sigma \\ m,\vec{k}',\sigma'}} \sum \phi^*_{n\vec{k}\sigma}(\vec{r})\, \phi_{m\vec{k}'\sigma'}(\vec{r})\, \hat{c}^{\dagger}_{n\vec{k}\sigma}\, \hat{s}\, \hat{c}_{m\vec{k}'\sigma'} . \qquad (13)$$

The spin deviation operator $s^-(\vec{K})$ (as in equation 12) can then be written as

$$s^-(\vec{K}) = \sum_{\vec{k},n,m} (n\vec{k}\downarrow | e^{-i\vec{K}\cdot\vec{r}} | m\ \vec{k}+\vec{K}\uparrow)\ \hat{c}^{\dagger}_{n\vec{k}\downarrow}\ \hat{c}_{m\ \vec{k}+\vec{K}\uparrow} . \qquad (14)$$

Here n and m are the band indices, $\uparrow$ and $\downarrow$ denote the spin directions, and the operators $\hat{c}^{\dagger}_{n\vec{k}\sigma}$ and $\hat{c}_{n\vec{k}\sigma}$ create and destroy, respectively, electrons in band n, with wavevector $\vec{k}$ and spin σ.

In the extreme tight-binding limit (localized orbitals), the $\vec{k}$ dependence drops out of the matrix elements, and in this case it is clearly more appropriate to introduce operators $\hat{c}^{\dagger}_{n\ell}$ and $\hat{c}_{n\ell}$ which create and destroy electrons in the state n on the site ℓ. Then equation 14 can be written as

$$\mathcal{S}^{-}(\vec{K}) = \sum_{n,m} \tilde{F}_{nm}(\vec{K}) \sum_{\ell} e^{-i\vec{K}\cdot\vec{R}_{\ell}} \hat{c}^{\dagger}_{n\ell\downarrow} \hat{c}_{m\ell\uparrow} \ . \tag{15}$$

Here n and m are no longer band indices, but single site atomic indices. Operators of this type can be used to describe singlet ground state systems, intermediate coupling, and crystal field levels. If the lowest set of states happens to belong to the same value of the total angular momentum, then we can construct the usual site operators $S^{\pm}_{\ell}$ and S^{z}_{ℓ} (using the Wigner-Eckart theorem) and finally obtain

$$\mathcal{S}^{-}(\vec{K}) \simeq \sum_{\ell} e^{-i\vec{K}\cdot\vec{R}_{\ell}} S^{-}_{\ell} F_{\ell}(\vec{K}) \ , \tag{16}$$

which will be recognized as the Heisenberg spin operator. Here $F_{\ell}(\vec{K})$ is the magnetic form factor, which is the Fourier transform of the atomic spin density. If the magnetic atoms are identical, $F_{\ell}(\vec{K})$ does not depend on ℓ. It is then customary to pull $F(\vec{K})$ out in front of the correlation functions, so that a factor $|F(\vec{K})|^2$ appears in the cross section formula.

Generalized Susceptibility

The cross section (equation 7) can be expressed in terms of a variety of other theoretical quantities which may be more convenient to work with and of more direct significance in statistical mechanics* than the spin-spin correlation functions. For our purposes it will be convenient to introduce the generalized (isothermal) spin susceptibility (equation 1), which is related to the spin density operators by

$$\chi^{\alpha\beta}(\vec{K},\omega) = \frac{(g\mu_B)^2 i}{N\hbar} \int_0^\infty < [\hat{\delta}^\alpha(\vec{K},t),\hat{\delta}^\beta(-\vec{K},0)] > e^{i\omega t}\, dt \ , \qquad (17)$$

where μ_B is the Bohr magneton and $[\hat{A},\hat{B}]$ denotes the commutator of the operators $\hat{A}$ and $\hat{B}$. The cross section can then be written in the form

$$\frac{d^2\sigma}{d\Omega d\omega} = \left(\frac{\gamma e^2}{m_e c^2}\right)^2 \frac{N\hbar}{\pi(g\mu_B)^2} \frac{k'}{k} \frac{e^{\hbar\omega\beta}}{e^{\hbar\omega\beta} - 1} \sum_{\alpha,\beta} (\delta_{\alpha\beta} - e_\alpha e_\beta)\ \mathrm{Im}\ \{\chi^{\alpha\beta}(\vec{K},\omega)\} \ , \qquad (18)$$

where $\beta = 1/kT$ and Im { } means take the imaginary part.

If the radial part of the wave functions for the unpaired electrons in the solid is not greatly different from that of the free atom,

---

*Marshall and Lovesey[78] formulate the cross section in terms of a variety of (related) functions, including spin-spin correlation functions, generalized susceptibilities, Green's functions, and response functions.

then the wave functions of these electrons in the solid should be well represented by linear combinations of corresponding atomic wave functions. This "tight-binding" theory should yield a good description of electrons which are in narrow energy bands, such as the 3d electrons in iron and nickel. Within this approximation equation 18 can be rewritten as

$$\frac{d^2\sigma}{d\Omega d\omega} = \left(\frac{\gamma e^2}{m_e c^2}\right)^2 \frac{N\hbar}{\pi(g\mu_B)^2} \frac{k'}{k} |F(\vec{K})|^2 e^{-2W(\vec{K})} \frac{e^{\hbar\omega\beta}}{e^{\hbar\omega\beta} - 1} \times \sum_{\alpha,\beta} (\delta_{\alpha\beta} - \kappa_\alpha\kappa_\beta) \mathrm{Im}\{\chi^{\alpha\beta}(\vec{q},\omega)\} . \tag{19}$$

Here $\vec{q} = \vec{K} - \vec{\tau}$, where $\vec{q}$ is the reduced wavevector and $\vec{\tau}$ is the necessary reciprocal lattice vector to bring $\vec{q}$ into the first Brillouin zone. $\chi(\vec{q},\omega)$ is now periodic in $\vec{\tau}$, since the aperiodic functions of $\vec{\tau}$, the form factor $F(\vec{K})$ and the Debye-Waller factor $e^{-2W(\vec{K})}$, have been removed from $\chi(\vec{K},\omega)$.

Calculation of the Susceptibility

In order to evaluate the cross section, we require a calculation of the susceptibility $\chi(\vec{q},\omega)$. To do this we need the Hamiltonian for the system, which is of the form

$$H = \sum_i \left\{ \frac{\hat{p}_i^2}{2m_e} + \hat{V}(\vec{r}_i) \right\} + \frac{1}{2} \sum_{i\neq j} \frac{e^2}{|\vec{r}_i - \vec{r}_j|} , \tag{20}$$

where the first term (H_o) is the kinetic energy of the electrons and the (periodic) potential energy due to the ion cores, and the last term is the energy due to the mutual Coulomb interaction of the electrons. The sum is over all the electrons. The last term is too difficult to treat analytically, so that some approximation (often the Hartree-Fock approximation) must be employed for it.

For the Bloch states $\phi_{n\vec{k}\sigma}(\vec{r})$, H can be expressed in the second quantized formalism as

$$H = \sum_{n,m,\vec{k},\sigma} < n\vec{k}\sigma | H_o | m\vec{k}\sigma > \hat{c}^{\dagger}_{n\vec{k}\sigma} \hat{c}_{m\vec{k}\sigma} \tag{21}$$

$$+ \frac{1}{2} e^2 \sum_{\substack{\ell,m,n,r \\ \vec{k}_1,\vec{k}_2,\vec{q} \\ \sigma,\sigma'}} < \ell\vec{k}_1\sigma; m\vec{k}_2+\vec{q}\sigma' | \frac{1}{|r - r'|} | n\vec{k}_2\sigma'; r\vec{k}_1+\vec{q}\sigma >$$

$$\times \hat{c}^{\dagger}_{\ell\vec{k}_1\sigma} \hat{c}^{\dagger}_{m\vec{k}_2+q\sigma'} \hat{c}_{n\vec{k}_2\sigma'} \hat{c}_{r\vec{k}_1+\vec{q}\sigma} .$$

Note that for the last term we have made use of the fact that the Coulomb potential is a non-spin-flip and momentum-conserving potential.

To introduce the tight-binding approximation, we expand the d-like part of the Bloch functions in terms of a set of orthonormal functions ψ which are strongly localized about atomic sites;

$$\phi_{n\vec{k}\sigma} = \frac{1}{\sqrt{N}} \sum_{\ell,\mu} e^{i\vec{k}\cdot\vec{R}_\ell} a_{n\mu\sigma}(\vec{k}) \psi_{\mu\sigma}(\vec{r} - \vec{R}_\ell) . \tag{22}$$

Here n is the band index, μ is the symmetry index (for example, with 3d states, μ ranges from one to five), and ℓ is the site index. Note that the functions $\psi_{\mu\sigma}(\vec{r} - \vec{R}_\ell)$ are not atomic orbitals, since atomic orbitals centered on different sites are not orthogonal. However, functions which have the same symmetry properties as the atomic orbitals and which are orthogonal can be constructed.[80]

In terms of the states ψ the Hamiltonian can be written as

$$H = \sum_{\ell,\ell'} \sum_{\mu,\nu,\sigma} T^{\sigma}_{\mu\nu}(\vec{R}_\ell - \vec{R}_{\ell'})\hat{c}^{\dagger}_{\ell\mu\sigma}\hat{c}_{\ell'\nu\sigma} + \frac{1}{2} \sum_{\mu,\nu,\lambda,\delta} \sum_{\ell,\ell',m,m'} \sum_{\sigma,\sigma'} \tag{23}$$

$$< \ell\mu\sigma;\ell'\nu\sigma' | \frac{1}{r} |m'\delta\sigma;m\lambda\sigma' > \hat{c}^{\dagger}_{\ell\mu\sigma}\hat{c}^{\dagger}_{\ell'\nu\sigma'}\hat{c}_{m'\delta\sigma}\hat{c}_{m\lambda\sigma'} ,$$

where

$$T^{\sigma}_{\mu\nu}(\vec{R}_\ell - \vec{R}_{\ell'}) = \int \psi^{*}_{\mu\sigma}(\vec{r} - \vec{R}_\ell)\, H_o\, \psi_{\nu\sigma}(\vec{r} - \vec{R}_{\ell'})\, d\vec{r} \tag{24}$$

and

$$< \ell\mu\sigma;\ell'\nu\sigma' | \frac{1}{r} |m'\delta\sigma;m\lambda\sigma' > \tag{25}$$

$$= e^2 \iint \frac{\psi^{*}_{\mu\sigma}(\vec{r} - \vec{R}_\ell)\psi^{*}_{\nu\sigma}(\vec{r}' - \vec{R}_{\ell'})\psi_{\delta\sigma}(\vec{r}' - \vec{R}_{m'})\psi_{\lambda\sigma'}(\vec{r} - \vec{R}_m)\, d\vec{r}d\vec{r}'}{|\vec{r} - \vec{r}'|} .$$

Of course, equation 22 may also be substituted directly into equation 21.

If the bands are narrow, then the overlap of the functions ψ centered on different sites is small. The tight-binding approximation corresponds to keeping only the matrix elements in the second term for which $\ell=\ell'=m=m'$. The remaining terms are assumed to be negligible. Note that the matrix elements of the first term for which $\ell\neq\ell'$, the "hopping" terms, are retained.

Single Band Model

The simplest model which contains the essential features of the scattering from an itinerant electron system is the single band Hubbard model.[16] For a single band in the tight-binding approximation equation 23 simplifies to

$$H = \sum_{\ell,\ell',\sigma} T(\vec{R}_\ell - \vec{R}_{\ell'}) \hat{c}^\dagger_{\ell\sigma}\hat{c}_{\ell'\sigma} + \frac{1}{2} I' \sum_{\ell,\sigma} \hat{n}_{\ell\sigma}\hat{n}_{\ell-\sigma} , \qquad (26)$$

where $\hat{n}_{\ell\sigma} = \hat{c}^\dagger_{\ell\sigma}\,\hat{c}_{\ell\sigma}$ is the number operator, and the Coulomb matrix elements are denoted by I'. This is the Hubbard Hamiltonian. If we now restrict ourselves to low temperatures the cross section is proportional to $\chi^{-+}(\vec{q},\omega)$, which is given in the random-phase-approximation (RPA) by[75] the "enhanced" susceptibility expression (with $I = I'/(g\mu_B)^2$)

$$\chi^{-+}(\vec{q},\omega) = \frac{\chi_o^{-+}(\vec{q},\omega)}{1 - I\chi_o^{-+}(\vec{q},\omega)} . \qquad (27)$$

Here $\chi_o^{-+}(\vec{q},\omega)$ is the so-called "non-interacting" susceptibility, which is

$$\chi_o^{-+}(\vec{q},\omega) = -\frac{(g\mu_B)^2}{N} \sum_{\vec{k}} \frac{< \hat{n}_{\vec{k}+\vec{q}\uparrow} > - < \hat{n}_{\vec{k}\downarrow} >}{\varepsilon(\vec{k}+\vec{q}) - \varepsilon(\vec{k}) + \Delta - \hbar\omega + i\eta} , \qquad (28)$$

and Δ is the (rigid) splitting between the up-spin and down-spin energy bands. The factors $< \hat{n} >$ may be replaced at low temperatures by Fermi distribution functions.

From these equations we can now determine the general features of the scattering. We may expect a response in the cross section when the imaginary part of the susceptibility diverges, which will occur whenever the denominator in either equation 27 or equation 28 vanishes. With the identity

$$\mathrm{Im}\left\{\lim_{\eta\to 0^+} \frac{1}{x + i\eta} = -\pi\delta(x)\right\} \qquad (29)$$

the imaginary part of $\chi_o^{-+}(\vec{q},\omega)$ can be written as

$$\mathrm{Im}\{\chi_o^{-+}(\vec{q},\omega)\} = \frac{\pi(g\mu_B)^2}{N} \sum_{\vec{k}} \left(< \hat{n}_{\vec{k}+\vec{q}\uparrow} > - < \hat{n}_{\vec{k}\downarrow} >\right) \qquad (30)$$

$$\times \delta(\varepsilon(\vec{k}+\vec{q}) - \varepsilon(\vec{k}) + \Delta - \hbar\omega) .$$

The singularities of $\mathrm{Im}\{\chi_o^{-+}(\vec{q},\omega)\}$ therefore occur when

$$\hbar\omega = \varepsilon(\vec{k}+\vec{q}) - \varepsilon(\vec{k}) + \Delta \quad \text{(for any } \vec{k}) . \qquad (31)$$

For $\vec{q} = 0$ this gives $\hbar\omega = \Delta$, the band splitting energy. As $\vec{q}$ becomes non-zero, there is an increasingly larger range of band energies that satisfy equation 30, and the excitations fan out from Δ. These are the (spin-flip) Stoner modes, which are seen to be rather diffuse in nature and hence difficult to observe.

If the real and imaginary parts of $\chi_o^{-+}(\vec{q},\omega)$ are separated via

$$\chi_o^{-+}(\vec{q},\omega) = {}^{R}\chi_o^{-+}(\vec{q},\omega) + i\ {}^{I}\chi_o^{-+}(\vec{q},\omega) \tag{32}$$

then the imaginary part of $\chi^{-+}(\vec{q},\omega)$, the "interacting" susceptibility, is

$$\text{Im}\ \{\chi^{-+}(\vec{q},\omega)\} = \frac{{}^{I}\chi_o^{-+}(\vec{q},\omega)}{(1 - I\,{}^{R}\chi_o^{-+}(\vec{q},\omega))^2 + (I\,{}^{I}\chi_o^{-+}(\vec{q},\omega))^2} \ . \tag{33}$$

Outside the region of the Stoner states, ${}^{I}\chi_o^{-+}(\vec{q},\omega) \equiv 0$, so that the poles are determined by

$$1 = I\,{}^{R}\chi_o^{-+}(\vec{q},\omega) = \frac{I'}{N} \sum_{\vec{k}} \frac{< \hat{n}_{\vec{k}+\vec{q}\uparrow} > - < \hat{n}_{\vec{k}\downarrow} >}{\varepsilon(\vec{k} + \vec{q}) - \varepsilon(\vec{k}) + \Delta - \hbar\omega} \ . \tag{34}$$

For $\vec{q} = 0$, we have (using $\sum_{\vec{k}} < \hat{n}_{\vec{k}\uparrow} > = N < n_\uparrow >$)

$$1 = \frac{I'}{N} \sum_{\vec{k}} \frac{< \hat{n}_{\vec{k}\uparrow} > - < \hat{n}_{\vec{k}\downarrow} >}{\Delta - \hbar\omega} = \frac{I'(< n_\uparrow > - < n_\downarrow >)}{\Delta - \hbar\omega} . \qquad (35)$$

Now $< n_\uparrow > - < n_\downarrow >$ is the magnetization (per atom), which is related to the band splitting by

$$\Delta = I'(< n_\uparrow > - < n_\downarrow >) . \qquad (36)$$

Thus for $\vec{q} = 0$ equation 35 has a solution for $\omega = 0$. This is the spin wave mode. As discussed previously, for an isotropic ferromagnet at small $\vec{q}$ the spin wave energy $\sim D|\vec{q}|^2$.

Note that if the spin wave mode enters the region of Stoner excitations, then $I\chi_o^{-+}(\vec{q},\omega)$ is no longer zero. We therefore no longer have a true singularity, and an intrinsic width is induced in the spin wave. The larger $I\chi_o^{-+}(\vec{q},\omega)$ is, the larger the induced width, and if $I\chi_o^{-+}(\vec{q},\omega)$ becomes large enough the pole will become completely washed out.

The excitation spectrum is shown schematically in Figure 1. The Stoner modes have been drawn for the case of a "strong" ferromagnet, which means that at T = 0°K all the electron spins are in the same direction (i.e., there are only majority spin electrons on the Fermi surface). For a "weak" ferromagnet there are both majority and minority spin electrons on the Fermi surface. Thus at some value of $\vec{q}$ it will be possible to take a spin-up electron on the Fermi surface at $\vec{k}$ and

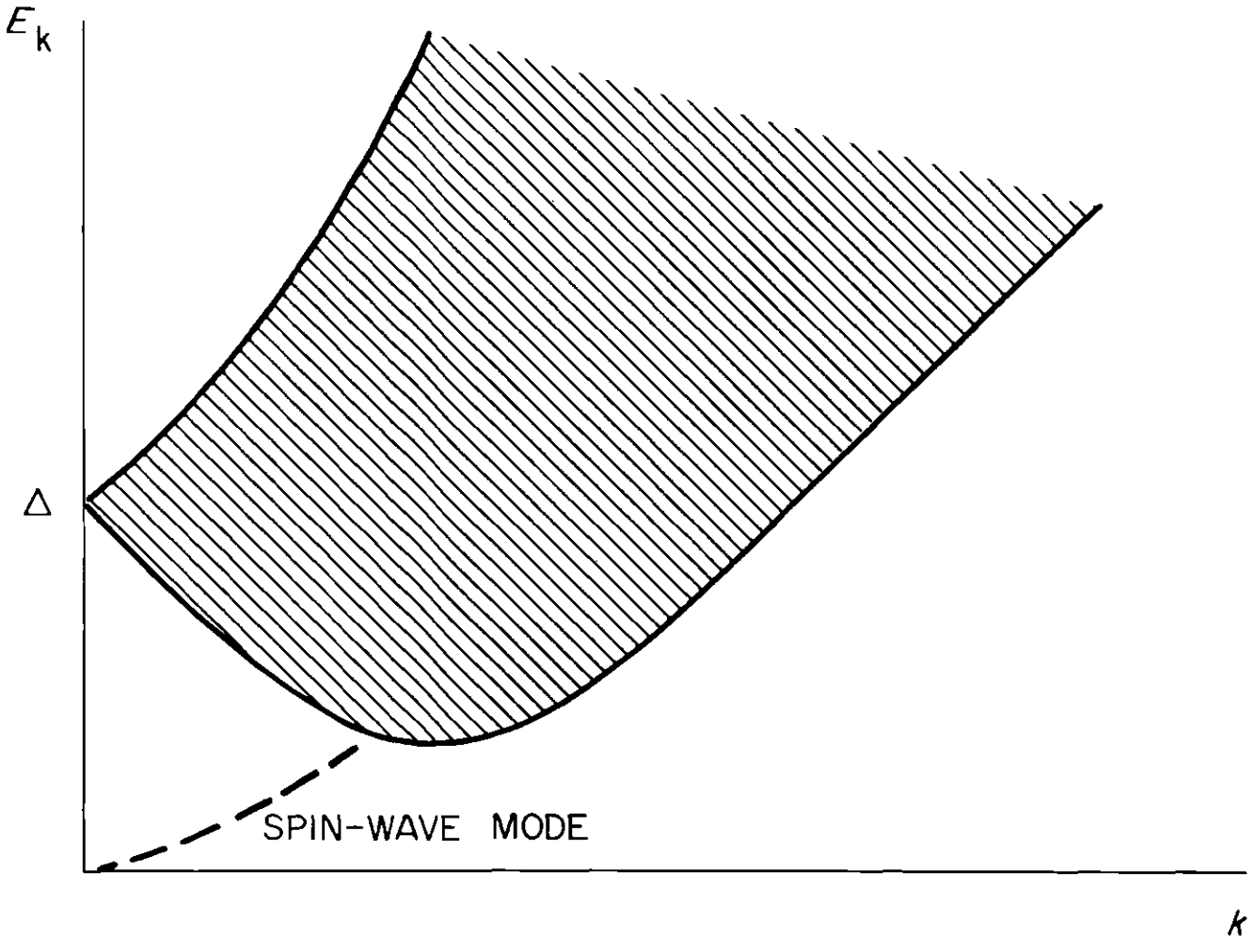

Figure 1. Schematic Diagram of the Spin Wave and Stoner Excitations Calculated from a Simple Band Model

place it in a down-spin state on the Fermi surface at $\vec{k}+\vec{q}$ (or vice-versa), so that the Stoner modes will extend to $\omega = 0$.

At low temperatures the band splitting Δ is given by equation 36, so that the simplest form of a temperature dependent theory would consist of setting Δ proportional to the magnetization. As the temperature is raised, we would therefore expect the Stoner excitations to lower in energy as Δ decreases, and indeed as the temperature is raised through T_C the Stoner modes should collapse into $\omega = 0$. Of course, we shouldn't be too surprised if this type of molecular field approximation does not give the correct spin dynamics at elevated temperatures. Even in this simple model, equation 36 represents only the leading order term (in the $< n >$'s) for the band splitting. As the magnetization decreases the higher order terms may become important. Above T_C, there may be short range spin correlations, so that over a limited region of space we may be able to define a "local" band-splitting, and hence be able to recover to some extent the low temperature picture. Nevertheless, it is expected that the Stoner states should decrease in energy at higher temperatures.

It should be pointed out that for elevated temperatures and for the multi-band case the region of Stoner states will not be as sharply defined as it is depicted in Figure 1. In fact, there will be a finite density of Stoner states at all $(\vec{q},\omega)$. What is important, however, is the magnitude of the density of Stoner states. A small density will induce a small intrinsic width into the spin wave mode, and the higher the density the larger the width. If the density becomes high enough,

the spin wave mode may in fact become completely damped out. It is this region of "high density of Stoner states" that should be thought of as depicted in Figure 1.

Calculations for Iron

Quantitative calculations of the dynamic susceptibility for systems whose magnetic electrons are itinerant are generally very difficult to do. The difficulty stems from the problem of properly incorporating into the energy band structure the electron correlations, which are of paramount importance in obtaining the magnetic properties of the model. Unfortunately, analytic solutions for realistic systems do not exist, so that approximate solutions which are at least amenable to numerical calculation must be sought. However, even if an adequate description of the electronic system is obtained, the equations for the neutron cross section are at least as complicated as present-day band sturcture equations, which require numerical solutions at general points in the Brillouin zone. Furthermore, a calculation of the susceptibility (as well as other magnetic and optical properties) requires the integration of quantities which involve the electronic energies and matrix elements of operators over the Brillouin zone, so that the method of solution must be fast enough for these integrals to be evaluated in a reasonable amount of computer time.

Of the 3d ferromagnetic metals, the electron correlations in nickel may be the easiest to handle, since on the average there is less than one magnetic electron per atom ($\mu_{spin} = 0.55\ \mu_B$). Nickel has

therefore been the first material to be treated in detail. The most ambitious calculations to date are those by Cooke and Davis[71] for the low temperature susceptibility of nickel. Their theory[70] is based on a simple extension of the RPA and an improved description of certain screened Coulomb matrix elements which appear in the theory. These improvements lead to a momentum dependent spin-splitting of the electronic energy bands as well as s-d hybridization, characteristics which are necessary in the band structure in order to obtain agreement with optical and Fermi surface measurements. The calculations are done by fitting a band structure interpolation scheme to a "first-principles" paramagnetic band structure. The interpolation scheme allows the rapid calculation of the electron energies and wavefunctions at a large number of $\vec{k}$ points. The ferromagnetic band structure is then generated self-consistently, with the only adjustable parameter in the theory being fixed to produce the observed low temperature spin-only moment. The appealing feature is that once the ferromagnetic band structure is determined, the calculation of the susceptibility follows automatically. There are no adjustable parameters to force agreement with experiment.

The overall agreement obtained between this theory and the experimental results for nickel gives us confidence that the calculation of $\chi(\vec{q},\omega)$ based on band structures is at least qualitatively correct. In view of the lack of any quantitative calculations of the susceptibility for the more difficult case of iron,[81] calculations of the non-interacting susceptibility for iron, based on the theory of Cooke and Davis, have been performed.

To extend the calculations to iron, an interpolation scheme must be chosen for the bcc lattice. We have used the Slater-Koster[82] interpolation method. This consists of forming Bloch sums of tight-binding orbitals (as in equation 22, but with the $a(k) \equiv 1$) and then setting up the Hamiltonian matrix. Since there are no non-diagonal matrix components between Bloch sums with different $\vec{k}$'s, we have terms of the form

$$\sum_{\vec{R}_j} e^{i\vec{k}\cdot\vec{R}_j} \int \psi_\mu^*(\vec{r})\ H\ \psi_\nu(\vec{r}-\vec{R}_j)\ dv\ . \tag{37}$$

Here μ and ν are the symmetry indices and j is the site index. The convenient feature of this representation is the simple dependence of each term on $\vec{k}$, while the proper symmetry requirements of the crystal (and hence the energy bands) are built in. The integrals, however, are extremely difficult to evaluate from first-principles. Rather than trying to calculate these integrals, then, they are merely used as disposable constants to fit a first principles band structure. With these constants determined, one can then diagonalize H rapidly to find the eigenvalues and eigenfunctions for a fine mesh of $\vec{k}$ points in the Brillouin zone, so that the electron density of states and the dynamic susceptibility can be evaluated accurately.

We have used nine tight-binding orbitals in this interpolation scheme: five d-like orbitals, one s-like orbital and three p-like

orbitals.* The sum was extended to second nearest neighbors, which results in 27 independent "Slater-Koster" integrals. The interpolation scheme is fit by a least-squares method to a suitable paramagnetic band structure. The ferromagnetic band structure is then generated by splitting the diagonal d-block elements. The t_{2g} and e_g part of the d-block can be split by different amounts, rigidly, or self-consistently by setting

$$\Delta_{t_{2g}} = [n_{\uparrow}(t_{2g}) - n_{\downarrow}(t_{2g})]\, U_{eff}\ /3 \tag{38}$$

$$\Delta_{e_g} = [n_{\uparrow}(e_g) - n_{\downarrow}(e_g)]\, U_{eff}\ /2\ .$$

Here $n_{\uparrow}(t_{2g})$ is the total number of spin up electrons (per atom) with t_{2g} character, etc. The density of states is calculated by the Gilat-Raubenheimer[83] method, and from this calculation the population factors and the Fermi energy can be determined. The band splittings are then adjusted to give the proper spin-only moment (2.122 μ_B). Exchange splitting of the "conduction" electrons has not been included, although there is a net conduction-electron moment due to s-d hybridization.

By way of example, Figure 2 shows the ferromagnetic band structure along the high symmetry lines in the Brillouin zone obtained by fitting Wood's paramagnetic bands[84] and using a rigid d-band splitting

---

*The transformation properties of these orbitals are given by xy,xz, and yz (t_{2g}); x^2-y^2 and $3z^2-r^2$ (e_g); and constant, x, y, z for s and p.

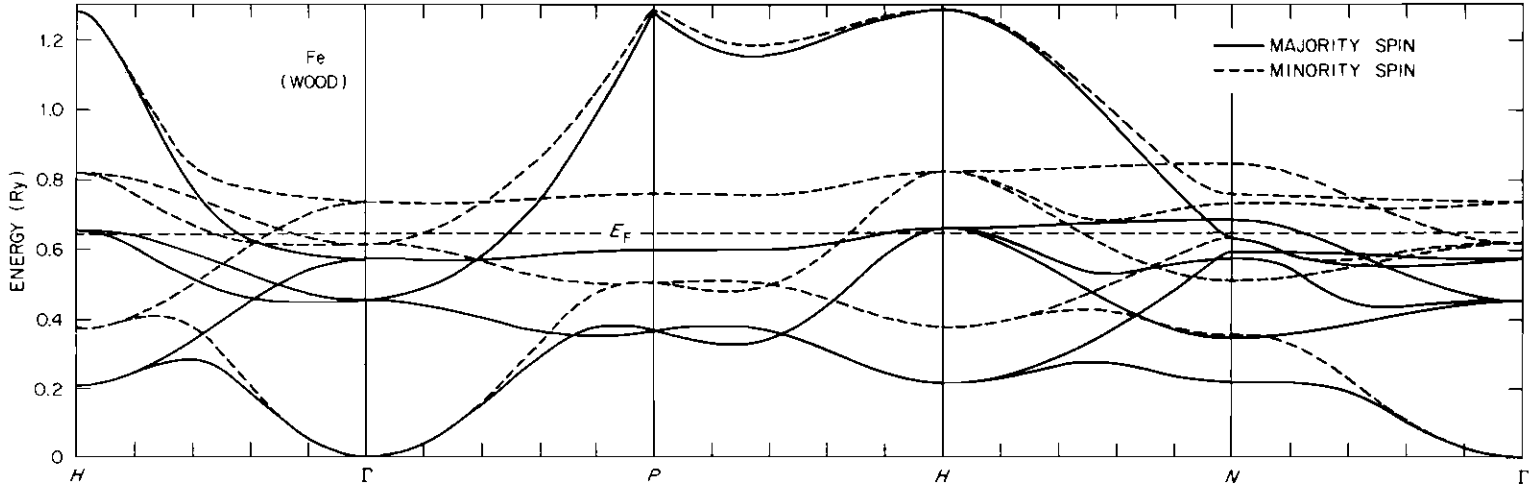

Figure 2. Ferromagnetic Band Structure of Iron

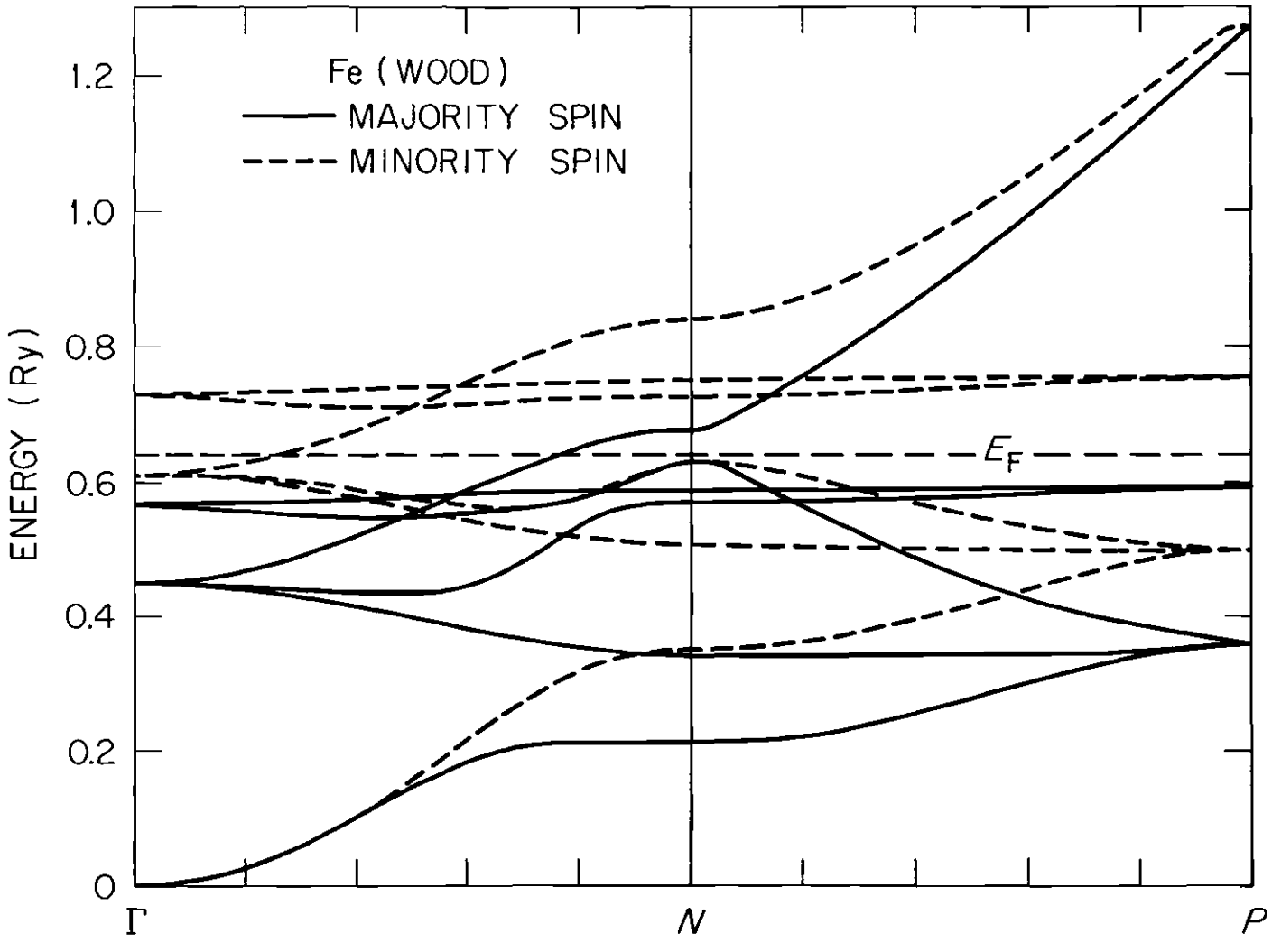

Figure 2 (continued)

of 2.22 eV. Only the lowest 12 bands are shown (six for each spin). The group theory notation is that of Koster,[85] and the bcc Brillouin zone, along with the irreducible zone, is shown in Figure 3. Note that because of s-d hybridization the splittings of the bands are $\vec{k}$-dependent, the spin splitting being proportional to the amount of d-character at each $\vec{k}$ point. If the t_{2g} and e_g bands were not split by the same amount, then there would be an additional $\vec{k}$-dependent splitting proportional to the amount of t_{2g} and e_g character of the bands at each $\vec{k}$. At Γ, the lowest band is pure s, the next band is the triply-degenerate t_{2g}, and then the doubly-degenerate e_g band (for each spin).

The ferromagnetic density of states calculated from this band structure is shown in Figure 4. The calculation has been done for 3080 $\vec{k}$ points in the irreducible zone, using an energy mesh of 0.00068 Ry. The t_{2g}, e_g and s-p character of the density of states has been projected out for the majority and minority spin directions and this is shown in Figures 5-7. Note that the splitting does not correspond to a rigid shifting of the majority and minority desnities of states. Once again this is due to the s-d hybridization. For this example we obtained the following: $\mu(t_{2g}) = 1.046\ \mu_B$, $\mu(e_g) = 1.177\ \mu_B$, $\mu(s\text{-}p) = -0.100\ \mu_B$ and $E_F = 0.6442$ Ry (measured from the bottom of the bands). This gives the net d-spin a 53% e_g character. At the Fermi surface we find that the electrons are characterized by having 80% t_{2g} character and 76% majority spin.

Once the band structure has been determined, the imaginary part of the non-interacting susceptibility can be evaluated by calculating

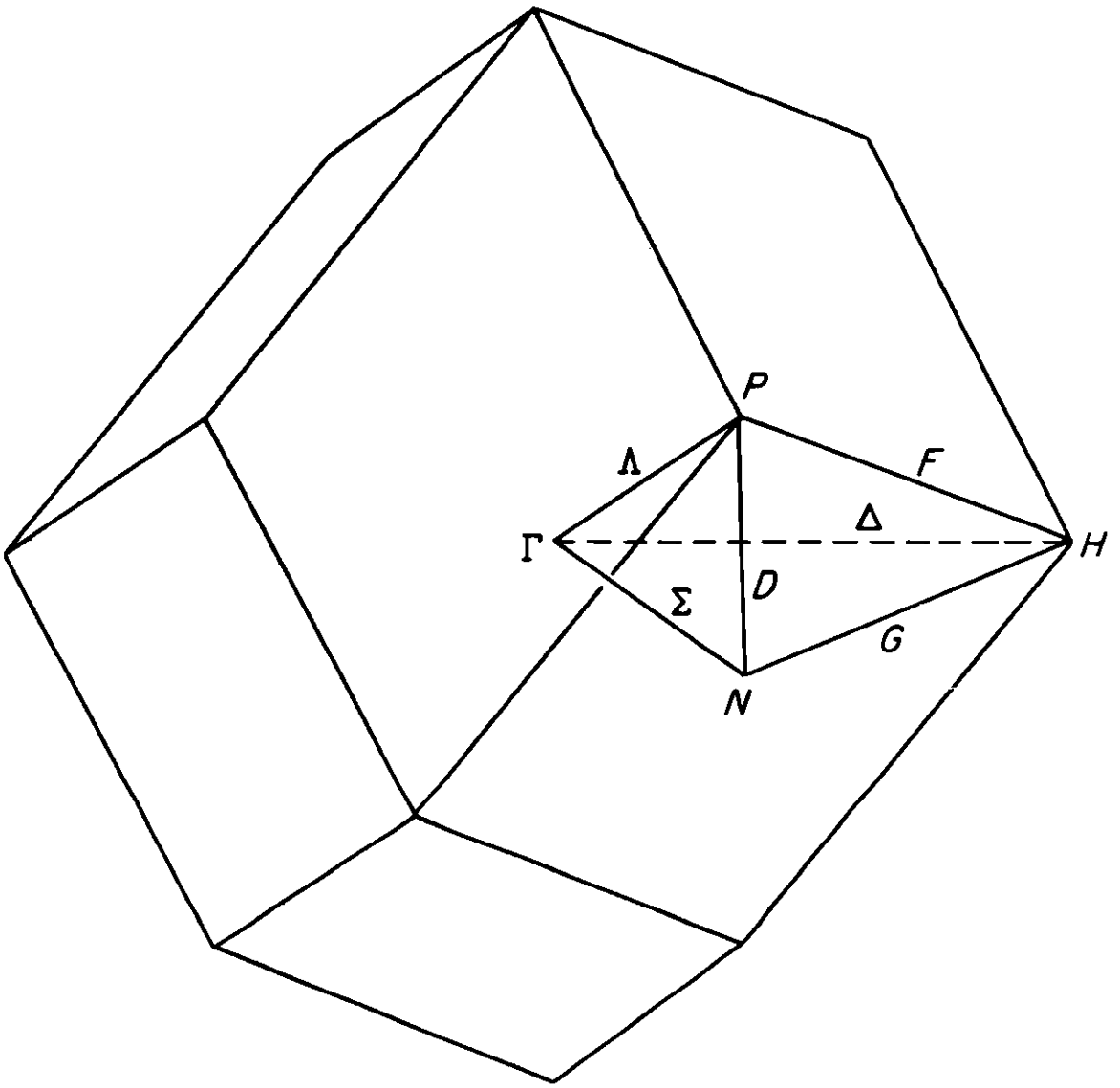

Figure 3. Body-Centered Cubic Brillouin Zone and the Irreducible Cell

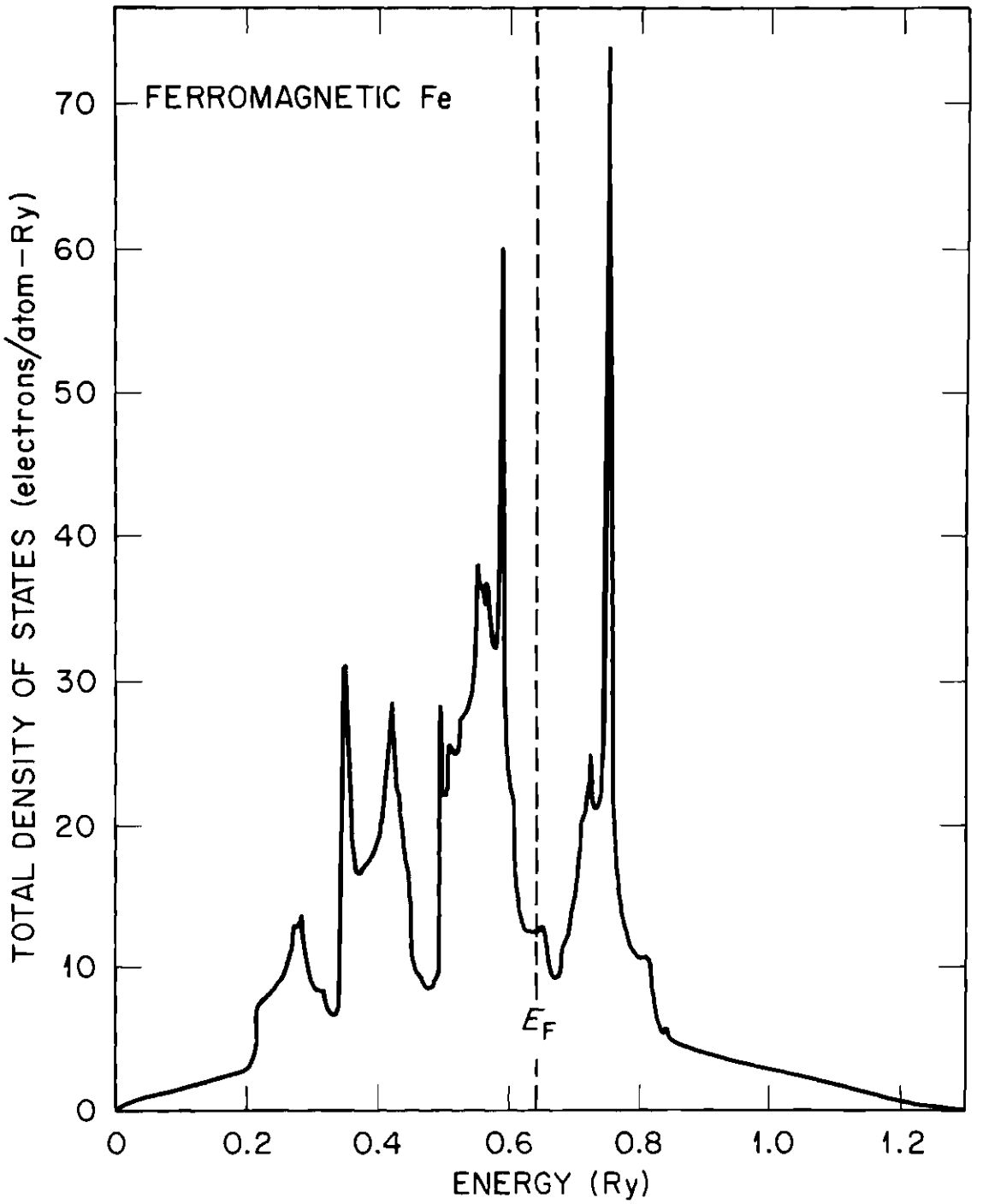

Figure 4. Total Density of Electron States Versus Energy for Ferromagnetic Iron

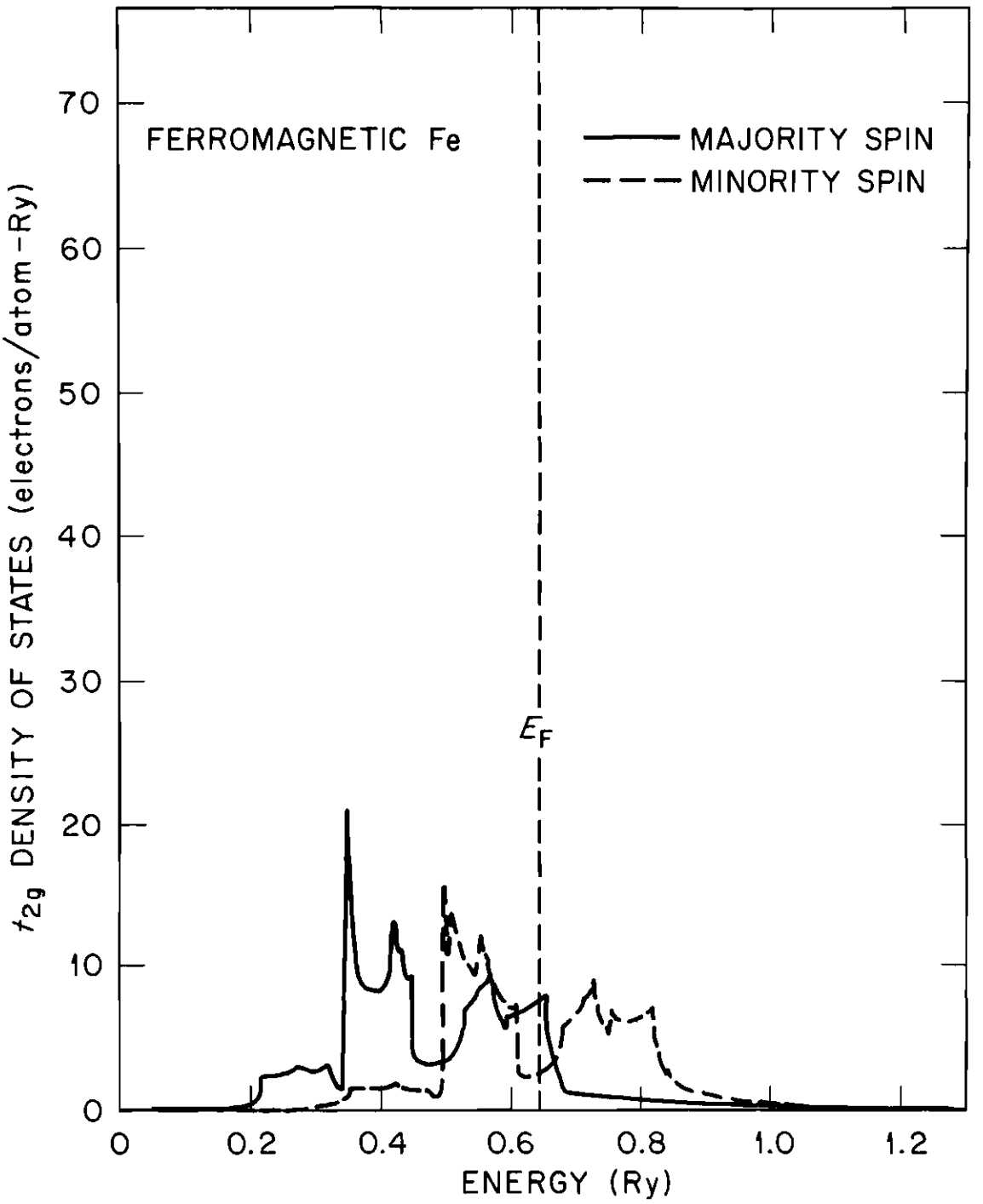

Figure 5. Density of t_{2g} Electron States Versus Energy for Majority and Minority Spin

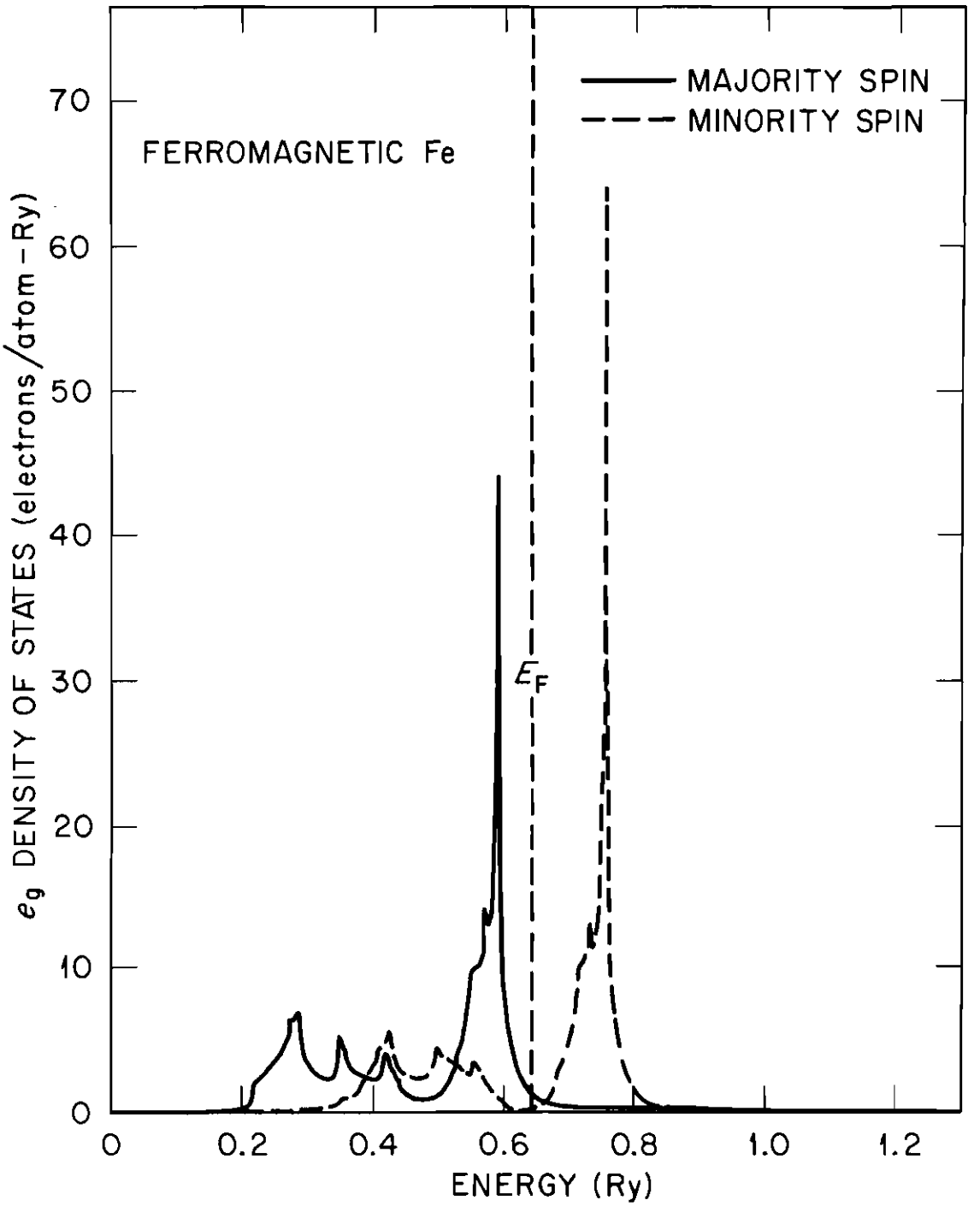

Figure 6. Density of e_g Electron States Versus Energy for Majority and Minority Spin

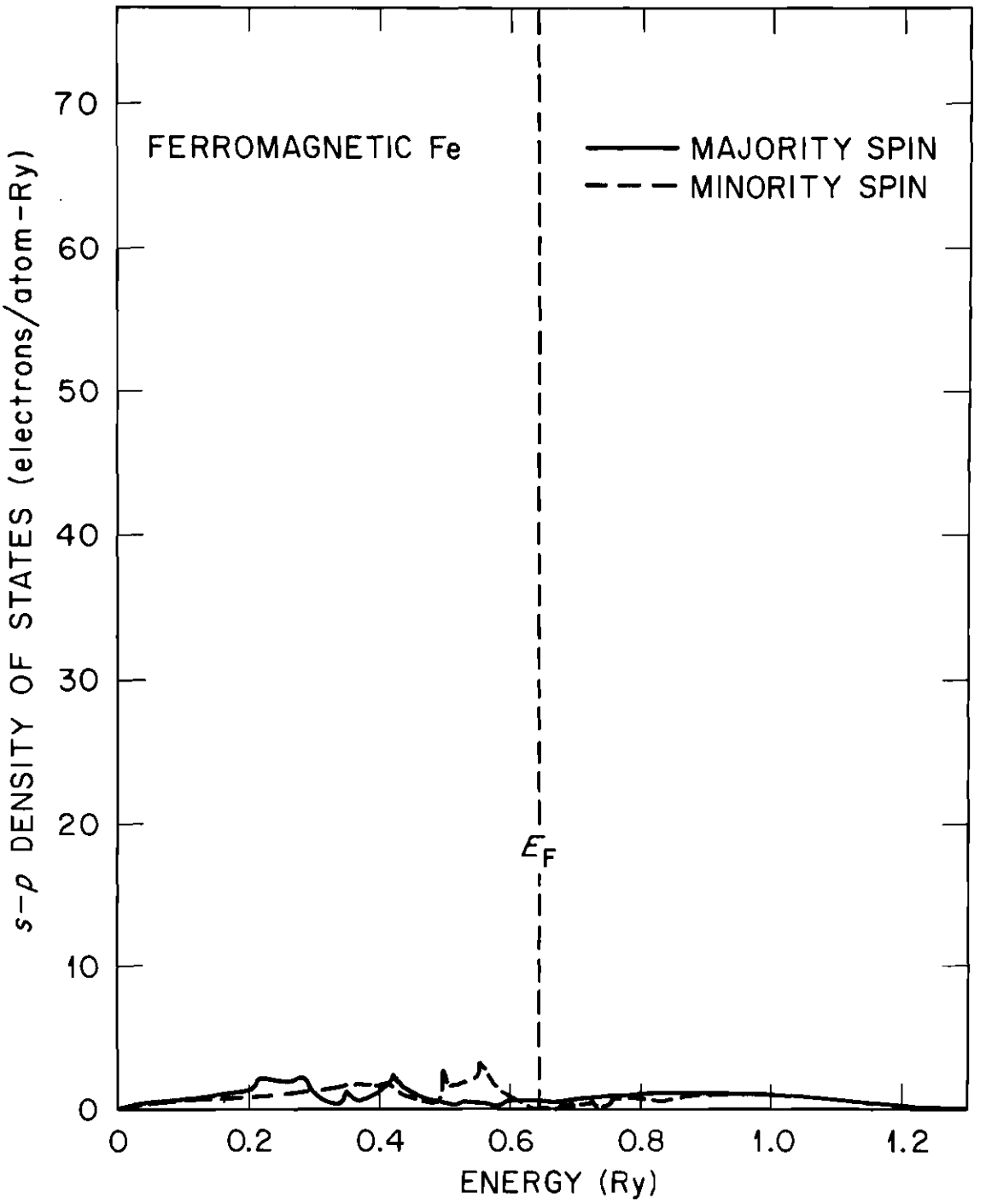

Figure 7. Density of s-p Electron States Versus Energy for Majority and Minority Spin

the density of spin-flip Stoner excitations, as in equations 6 and 30 except treating the multiband case. Figure 8 shows an example of the Stoner density of states calculated from the band structure shown in Figure 2 and also from the paramagnetic band structure of Wood. The density is plotted for $\vec{q}$ = (0.3,0,0) as a function of energy. Note that at low temperature there is a finite density of states at small energies and that the density smoothly increases up to the peak at the band splitting energy. This is fairly typical of the density of states calculated at different values of $\vec{q}$ and for different directions in the crystal, and can be contrasted with the density of Stoner states for a single band model as depicted in Figure 1. In this case the density is identically zero until a finite value of the energy is reached, and then the density abruptly jumps to a fairly large value. It is this latter behavior which is generally thought to cause the sharp cutoff of the spin wave intensity.

It should be kept in mind that the band splitting of 2.22 eV, which is necessary to produce the correct ferromagnetic moment from Wood's paramagnetic bands, is larger than the band splitting that might be expected for iron ($\sim$1 eV). However, different splittings can be obtained by using different paramagentic band structures as starting points for these calculations. The band splitting can also be reduced by neglecting s-d hybridization, which is probably not treated very accurately in either the interpolation scheme or the "first principles" band structure calculations. For example, by neglecting s-d hybridization, the band splitting obtained from Wood's paramagnetic bands is reduced to 1.46 eV.

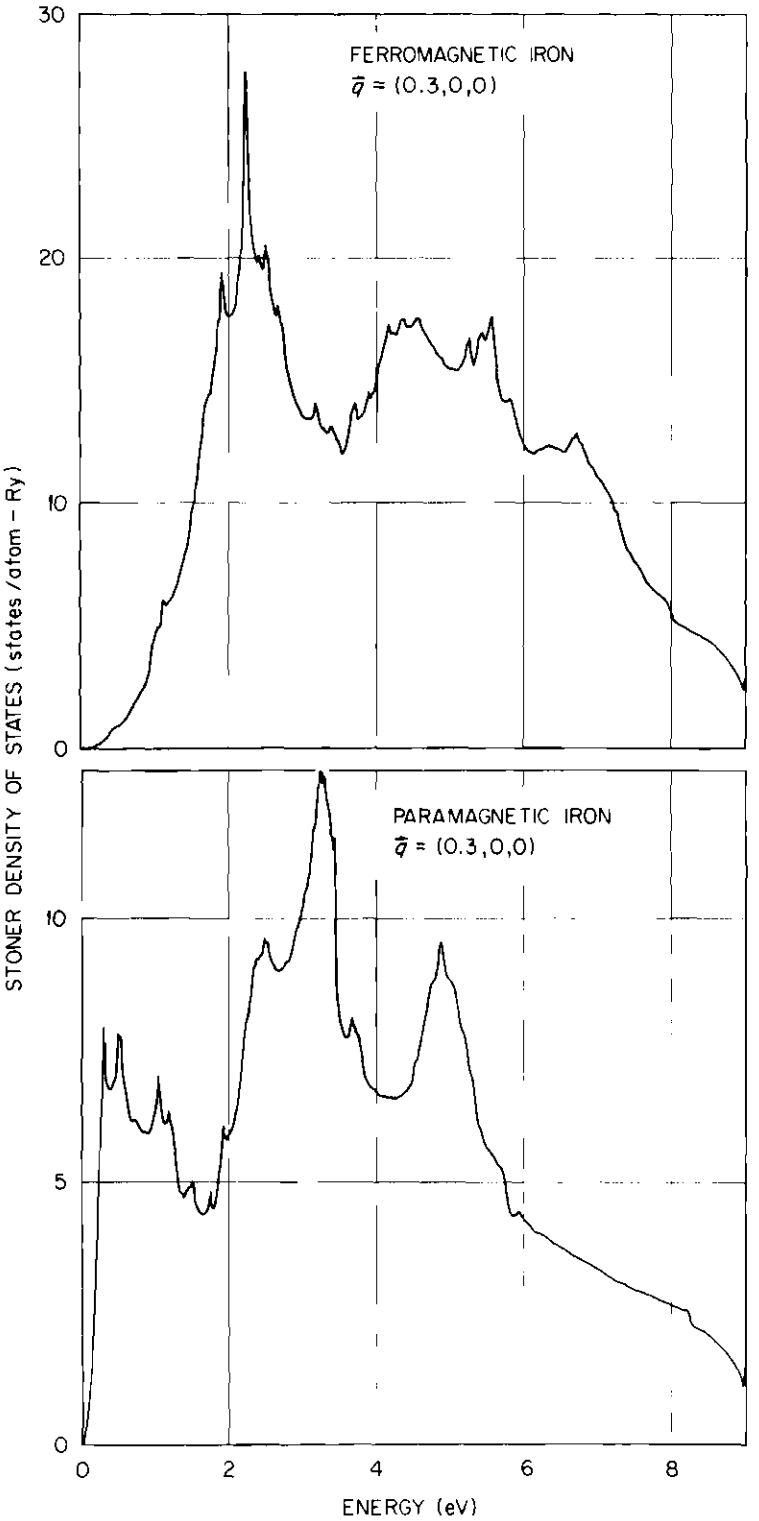

Figure 8. Density of Single Particle Spin-Flip Excitations for Iron

The ferromagnetic band structures and Stoner densities of states were calculated from a number of other band structures, and it was found that the overall shape of the Stoner density of states did not change appreciably, but the spectra were shifted to higher or lower energies depending on the value of the band splitting needed to produce the observed ferromagnetic moment. It is clear from these calculations that the region of high density of spin-flip states apparently occurs at too high an energy and increases too slowly with energy to explain the sharp decrease in the spin wave intensity in iron. Even with no band splitting, the region of high density of Stoner states (away from $\vec{q} = 0$) comes at too high an energy (the lowest energy peak in the figure occurs at $\sim$300 meV), although the overall spectrum is, of course, shifted to lower energies. However, it is not yet known in general how high the density of Stoner states needs to be in order to induce a substantial width into the spin wave peak. This requires incorporating into the density of states calculation the matrix elements governing the transition probabilities for decay of the spin wave states into Stoner states. Certainly more theoretical effort will be needed in order to clarify the nature of the disappearance of the spin wave intensity in iron.

CHAPTER III

EXPERIMENTAL APPARATUS AND PROCEDURES

Triple-Axis Neutron Spectrometers

The majority of the measurements were taken on the HB-3 triple-axis neutron spectrometer[86] installed at the High Flux Isotope Reactor (HFIR) at the Oak Ridge National Laboratory. Additional high resolution measurements on nickel were taken on the HB-4A triple-axis neutron spectrometer which is also at the HFIR. The triple-axis technique has been discussed at length in the literature,[87,88] so that only a brief description of the operation of the spectrometers will be given here.

A schematic diagram of the HB-3 spectrometer is shown in Figure 9. Neutrons from the reactor are incident upon a monochromator crystal, which "Bragg" reflects neutrons of the desired energy at an angle $2\Theta_M$ from the reactor-beam direction. This defines the energy E_o and momentum $\hbar\vec{k}_o$ of the neutrons incident upon the sample. The second axis of the spectrometer is rotated an angle Φ from the incident monochromatic beam direction so that neutrons scattered from the sample in the Φ direction arrive at the analyzer crystal, which is set to only reflect neutrons with energy E' and momentum $\hbar\vec{k}'$. Thus both the energy

$$\hbar\omega = E_o - E' = \frac{\hbar^2}{2m_N}\left(|\vec{k}_o|^2 - |\vec{k}'|^2\right) \tag{39}$$

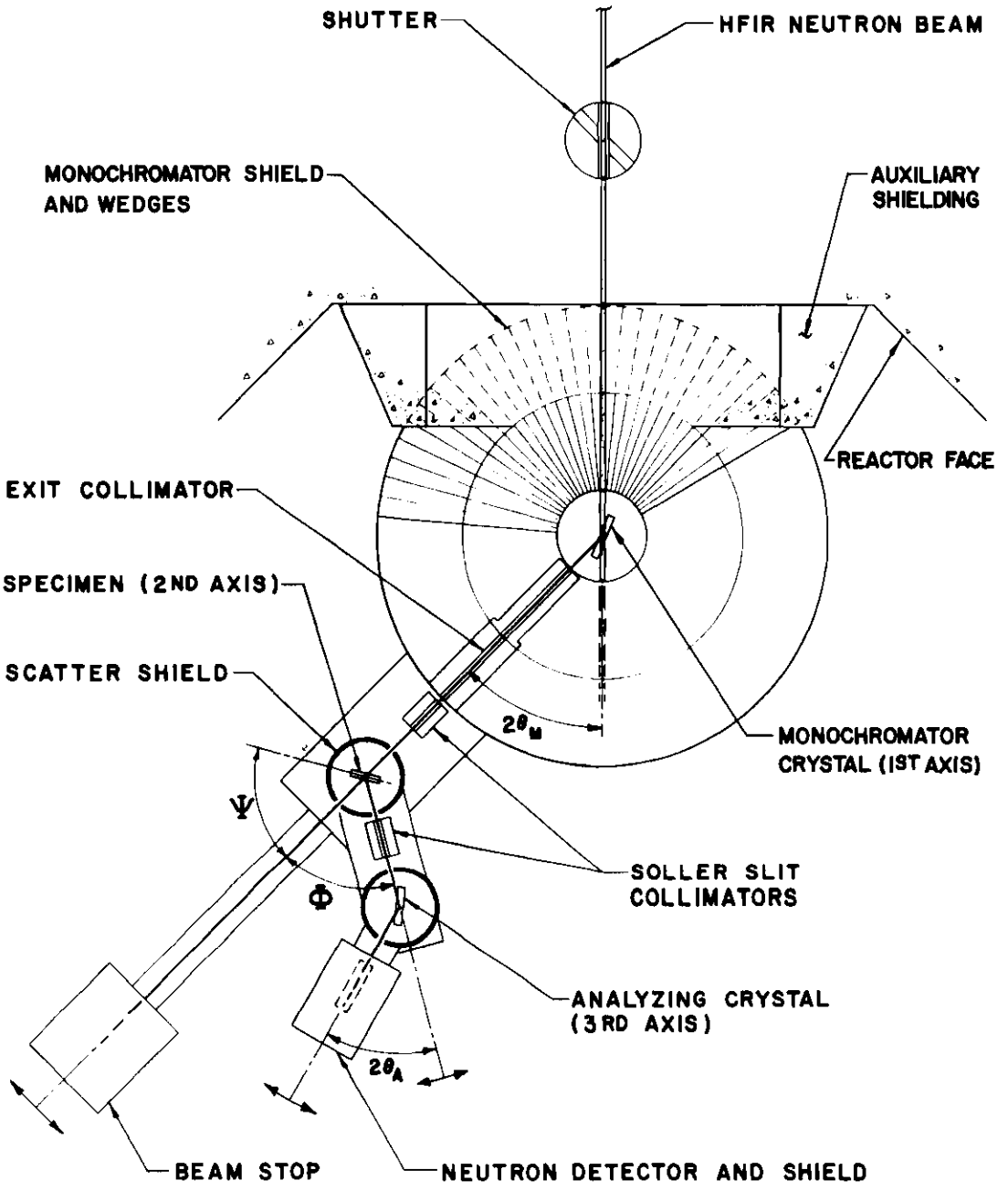

Figure 9. HB-3 Triple-Axis Neutron Spectrometer

and momentum

$$\hbar\vec{K} = \hbar(\vec{k}_o - \vec{k}') \quad (= -\hbar\vec{Q}) \tag{40}$$

that the crystal receives can be measured. Note that $\hbar\vec{Q}$ is the momentum change of the neutron.* The angle Ψ is set so that the desired orientation of reciprocal space in relation to $\vec{K}$ is obtained. A typical scattering diagram, corresponding to the measurement of a high energy spin wave (one point in the scan) in iron, is shown in Figure 10. The triangle has been drawn for the following parameters: $\hbar\omega$ = 103.4 meV, E' = 95.1 meV, E_o = 198.5 meV, $\vec{Q}$ = (1.2,1.2,0.0) and $\vec{q}$ = (0.2,0.2,0.0) in reduced units.

Of course, the actual energy and momentum change of the crystal due to each individual detected neutron is not exactly $\hbar\omega$ and $\hbar\vec{K}$, but has a spread of values ($\Delta\omega$ and $\Delta\vec{K}$) determined by the resolution of the spectrometer. Cooper and Nathans[87] have shown that the resolution function which describes the probability for neutron transmission by the spectrometer is given to a very good approximation by

$$R(\omega+\Delta\omega,\vec{K}+\Delta\vec{K}) = R_o \exp\left\{ -\frac{1}{2}\sum_k\sum_\ell M_{k\ell}X_kX_\ell \right\} \tag{41}$$

where $X_1 = \Delta K_x$, $X_2 = \Delta K_y$, $X_3 = \Delta K_z$ and $X_4 = \Delta\omega$. R_o and the matrix M are complicated functions of the spectrometer parameters, but the

*For the cases we will be considering, either $\vec{K}$ or $\vec{Q}$ can be used (interchangeably) in the formulas.

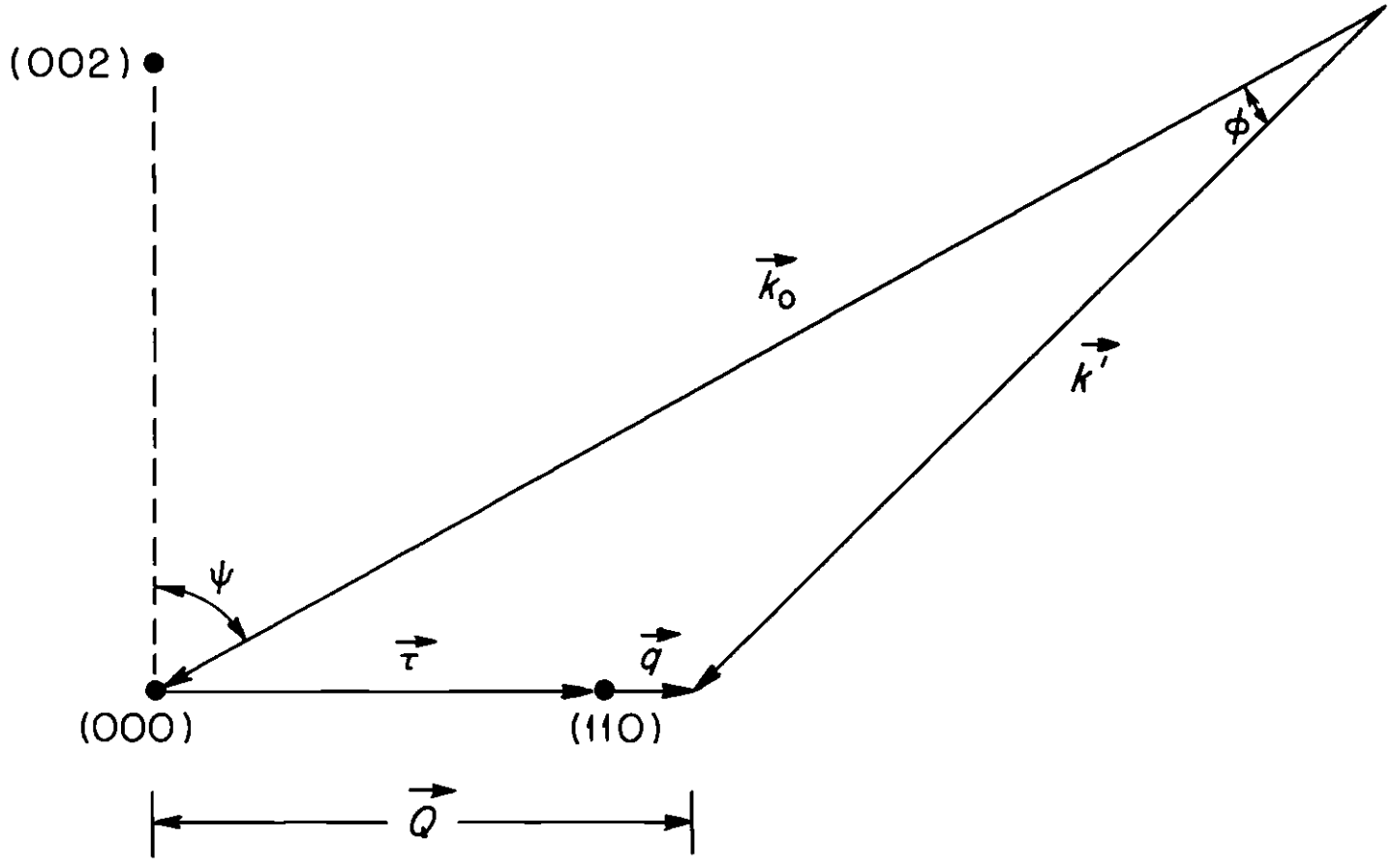

Figure 10. Typical Scattering Diagram for Measurement of a High Energy Spin Wave in Iron

dependence on $\Delta\vec{K}$ and $\Delta\omega$ is quite simple, being gaussian for any line passing through $\vec{K},\omega$. Surfaces of constant transmission probability are ellipsoids, and the "resolution ellipsoid" is defined as the surface where the resolution function has fallen to half its maximum value.

At each setting of the spectrometer the observed intensity $I(\vec{K},\omega)$ is then given by the convolution of the scattering cross section $\sigma(\vec{K},\omega)$ with the resolution function;

$$I(\vec{K},\omega) = \int R(\omega+\Delta\omega,\vec{K}+\Delta\vec{K})\ \sigma(\omega+\Delta\omega,\vec{K}+\Delta\vec{K})\ d(\Delta\vec{K})d(\Delta\omega)\ . \qquad (42)$$

The operation of the spectrometer consists of a measurement of the scattered intensity $I(\vec{K},\omega)$ (per fixed number of neutrons incident on the sample) at a series of $(\vec{K},\omega)$ values. If the resolution ellipsoid intersects a dispersion surface during one of these "scans", a peak in the response will be observed, corresponding to the $(\vec{q},\omega)$ of the excitation. By performing a series of scans, one can determine the dispersion surface throughout the Brillouin zone.

Intensity Considerations

Because neutron inelastic scattering cross sections are generally quite small (hence the need for high flux reactors), the experimental configuration must be arranged to optimize the observed scattering. For spin wave scattering from iron and nickel there are three basic requirements that dictate the mode of operation of the spectrometer.

Since the spin wave excitations in iron and nickel extend to high energies (compared to kT), all the measurements have been taken

with $E_o > E'$, so that the neutrons create spin waves in the crystal. This is necessary because the Bose thermal factor, $< n > = [e^{\hbar\omega/kT} - 1]^{-1}$ is much less than one ($< n > << 1$) for the high energy spin waves. The scattering cross section for spin wave creation (neutron energy loss) is proportional to $1 + < n >$, whereas the cross section for spin wave destruction (neutron energy gain) is proportional to $< n >$.

The second consideration arises because the spin wave dispersion relations in the 3d metals are very steep. This necessitates measuring the higher energy spin waves by fixing the energies of the incident and scattered neutrons that the spectrometer transmits and by varying $\vec{K}$, which is called a "constant-E" scan. This type of scan will cut directly across the dispersion surface, giving a sharp peak in the scan. The more familiar "constant-$\vec{Q}$" scan (or "constant-$\vec{K}$" scan) would almost parallel the spin wave dispersion surface. The resolution ellipsoid would then "drag" along the dispersion surface over a large energy range, giving a very broad distribution of scattered intensity.

Finally, although the elementary excitation spectrum in a periodic lattice is itself periodic (so that $\hbar\omega(\vec{q}) = \hbar\omega(\vec{q} + \vec{\tau})$, where $\vec{\tau}$ is any reciprocal lattice vector), the neutron scattering cross section does not have this same periodicity. Inspection of equation 19 shows that an important consideration will be the magnetic form factor $F(\vec{K})$, which is the Fourier transformation of the magnetization density in the unit cell. This is analogous to the form factor appropriate to x-ray scattering, except that the 3d magnetic form factor falls off more rapidly with increasing $\vec{K}$ than in the x-ray case. To maximize the scattered

intensity, $\vec{K}$ must be kept as small as practical. This has important consequences when measuring the high energy spin waves, as demonstrated in Figure 10. If we want to measure the scattering at a large energy transfer, then there must be a large difference in the lengths of the vectors $\vec{k}_o$ and $\vec{k}'$, as required by equation 39. However, in order to keep $\vec{K}$ reasonably small and still satisfy equation 40, $\vec{k}'$ must be fairly long also. Thus very high incident neutron energies must be used. For the measurement of spin waves $\sim$100 meV, incident neutron energies $\sim$200 meV have to be used. At these energies the flux of neutrons from the reactor is greatly reduced, so that the required counting times for measurement of these spin waves are very long. Fortunately, because of the design of the HFIR, the entire energy spectrum of the neutrons is shifted to higher energies compared with many other research reactors, so that the flux of high energy neutrons onto the sample is considerably higher at the HFIR than elsewhere. At an incident neutron energy $\sim$200 meV, for example, the flux onto the sample (with open collimation) is $\sim 5 \cdot 10^6$ neutrons/cm^{2}sec, which is nevertheless reduced by a factor of 20 from the maximum flux. Without the high flux of high energy neutrons available at the HFIR and the large single crystal samples grown from isotopes which are particularly favorable for measuring the magnetic scattering, these experiments would not have been possible.

Spectrometer Details and the Furnace

The majority of the measurements were taken on the HB-3 spectrometer using the constant-E mode of operation. The monochromator was a beryllium single crystal with the $(10\bar{1}1)$ planes oriented for reflection,

Be(10$\bar{1}$1). The analyzer crystal was Be(0002). Both of these crystals have a mosaic spread of 0.25°. For the higher energy spin waves, two-thirds degree Soller slits were used before and after the sample, and scattered neutron energies up to 103.4 meV were employed. For higher resolution measurements, one-third degree slits were used.

Measurements on nickel were also made on the high resolution HB-4A spectrometer. Neutrons with energies of 32.66 meV were incident on the sample from a Be(0002) crystal having a mosaic spread of 0.18°. The flight path from the monochromator to the sample is ∿7 m, giving a vertical and horizontal angular divergence of ∿0.25°. No additional collimation was used before the sample. Several different sets of collimation were used after the sample, including one-third degree horizontal collimation between the sample and analyzer, and one degree horizontal and vertical collimation in front of the detector. The analyzer was a Be(10$\bar{1}$1) crystal with a mosaic spread of 0.20°.

The samples were each mounted in the high temperature vacuum furnace described in Appendix A. Three calibrated thermocouples (one chromel-alumel and two Pt-Pt(10% Rh)) were spot-welded to the sample to determine the temperatures of the samples. The calibration of these thermocouples was checked by increasing the resolution of the spectrometer and measuring the critical magnetic scattering as the temperature passed through the ferromagnetic transition temperature T_C. The temperature gradients across the samples were found to be <2°K, with a temperature stability of better than 0.5°K over a 48-hour period. The temperature control of the samples was found to be more than adequate.

Data Collection and Analysis

Each scan was fit by a least-squares procedure to a sum of gaussian distributions (one for each peak) plus sloping background. This should be a valid procedure* if the dispersion surfaces do not deviate appreciably from planar dispersion surfaces over the extent of the (gaussian) resolution ellipsoid, and in fact excellent fits to the data were achieved with this method. The position, integrated intensity and width of each peak may then be extracted from the data. It was found that this was a reliable and particularly convenient method for cases when two (or more) peaks were overlapping each other, which occurred in some of the low energy scans due to the presence of both magnons and phonons. The positions, intensities and widths were also obtained by hand and checked with the computer results for consistency. The results agreed within experimental error. In addition, rather extensive resolution calculations (based on equations 41 and 42) were performed to determine the extent of the influence of the finite resolution of the spectrometers on these results. The resolution effects were found to be small, but not negligible. These effects will be discussed when the data are presented.

Spin Wave Intensity Analysis

If the resolution ellipsoid is passed through a dispersion surface, then the integrated intensity of the observed peak is related to the magnitude of the cross section being observed. Brockhouse et al.,[88]

---

*The case when the excitation has an appreciable intrinsic width will be discussed shortly.

showed how the interpretation of the intensities of a series of peaks measured along a dispersion surface can be greatly simplified, if the scattered neutron energy is not changed during the series of measurements, and if the flux of neutrons incident upon the sample is monitored by a low efficiency "1/v" detector.* Mook and Nicklow[67] have discussed in detail the interpretation of spin wave intensities for iron taken with this experimental arrangement and using the constant-E mode of operation. If within the region where the resolution ellipsoid intersects the dispersion surface, this surface does not deviate appreciably from a plane, and the variation of the scattering cross section along the dispersion surface can be ignored, then the observed integrated intensity I(E) is given to a good approximation by

$$I(E) = \frac{c\,\sigma(\vec{K}_o,E)}{|\vec{\nabla}_{\vec{q}}\omega|} \sim \frac{< n(E) > F^2(\vec{K}_o)\chi_s(E)\; e^{-2W(\vec{K}_o)}}{|\vec{\nabla}_{\vec{q}}\omega|} \qquad (43)$$

where $< n >$ is the Bose thermal occupation factor, $F(\vec{K}_o)$ is the magnetic form factor, $e^{-2W(\vec{K}_o)}$ is the Debye-Waller factor, $|\vec{\nabla}_{\vec{q}}\omega|$ is the slope of the dispersion surface, $\vec{K}_o$ is the value of $\vec{K}$ at the peak position, and $\chi_s(E)$ is the spin wave intensity. c is a complicated function of the spectrometer parameters, but does not vary from scan to scan. Mook and

*For the range of incident neutron energies used in these experiments (up to ~200 meV), the uranium fission detector employed as a monitor has a cross section proportional to 1/v. This monitor-efficiency factor cancels the factor k'/k in the neutron cross section.

Nicklow found that for the type of triple-axis scans used in these measurements, equation 43 in fact gives a good description of the operation of the spectrometer. These are the corrections that have been applied to the observed spin wave intensities to obtain the spin wave intensities $\chi_s(E)$ reported in Chapter 4.

Equation 43 may be understood in the following way. If we measure an integrated intensity I(E) in a constant-E scan, then to obtain a quantity which is proportional to the "scattering strength" of a spin wave state we need to take into account both the density (number) of spin wave states which contribute to the scattering and the thermal occupation of these states. The magnetic form factor $F(\vec{K})$ and the Debye-Waller factor $e^{-2W(\vec{K})}$ will also vary along the dispersion surface from scan to scan, although their variation is small unless the scans are done around different reciprocal lattice points. All the other factors which vary from scan to scan are automatically taken into account due to the manner in which the spectrometer is operated. This is because with k' fixed, the reflectivity of the analyzer crystal and the counting efficiency of the main detector remain fixed during the series of scans. Then the only part of the spectrometer which can change the volume of resolution ellipsoid (and thus the integrated intensity of the peak) is associated with E_o (the angle $2\theta_M$). As E_o increases (and hence $\hbar\omega = E_o - E'$ increases) the spread of energies ΔE_o becomes larger and this increases the flux of neutrons onto the sample. But this is reflected in a proportional increase in the counting rate of the monitor, and the effects cancel one another.

The density of states factor is $1/|\vec{\nabla}_{\vec{q}}\omega|$, and occurs for the following reason. For states of a crystal which are described by periodic (Bloch) wave functions (for example electrons, magnons and phonons), the density of states per unit range of wavevector is a constant. If a series of constant-$\vec{Q}$ scans is performed, then the number of states "sampled" by the resolution ellipsoid in each scan is the same.* However, the density of states per unit range of energy is not a constant, so that for constant-E scans the number of states "sampled" is not the same for each scan. The situation is depicted in Figure 11, where it can be seen that the density of states per unit range in energy is given by the reciprocal of the slope of the dispersion surface, and hence this factor must be included in equation 43.

As a function of temperature there are several additional quantities in the cross section which can vary. The magnetic moment μ (analogous to S in the localized model and not $< S^z >$) and the form factor $F(\vec{K})$ may be temperature dependent. However, measurements[5,6] show that they have (at most) only a weak dependence on temperature, and their temperature dependence has been retained in the spin wave intensities ($\chi_s(E)$) presented. The Debye-Waller factor $e^{-2W(\vec{K})}$ does vary with temperature, and this effect will be discussed when the data are presented.

---

*Recall that any variation in the size of the resolution function from scan to scan has already been taken into account experimentally. However, care must be taken to avoid situations where the resolution changes appreciably during the scan.

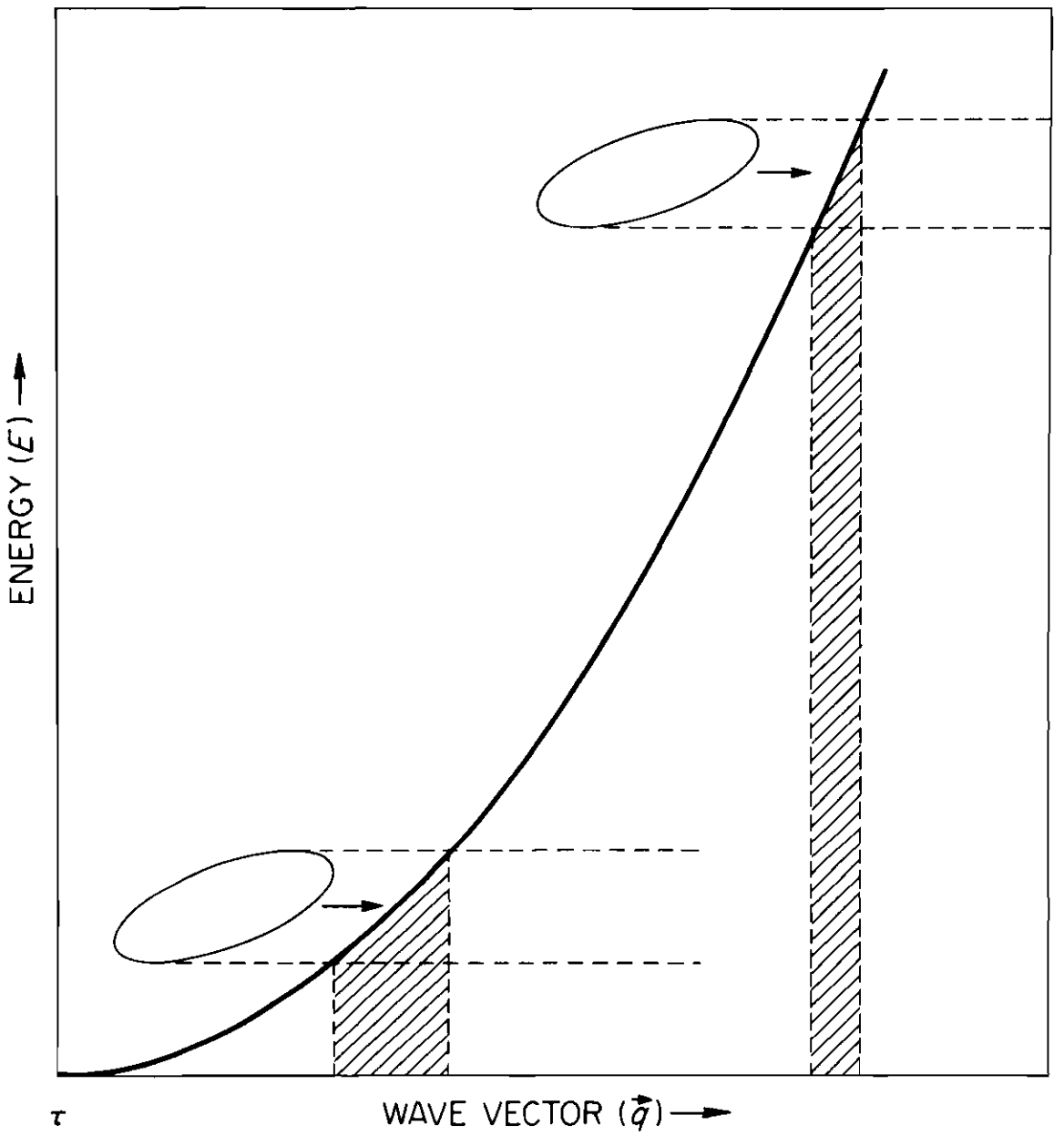

Figure 11. Density of Spin Wave States "Sampled" in Constant-E Scans. $\rho(E) \sim 1/|\nabla_{\vec{q}}\omega|$

It should be pointed out that there are a number of additional experimental factors which can influence the spin wave intensity measurements, particularly at high energies. When the monochromating and analyzing crystals are set to reflect a wavelength λ, they may also reflect higher order wavelengths (recall that Bragg's law is $n\lambda = 2d \sin\theta$). Thus when the spectrometer is set to transmit $(\vec{k}_o, \vec{k}', E_o, E')$ it may also transmit $(\vec{k}_o, 2\vec{k}', E_o, 4E')$, $(2\vec{k}_o, \vec{k}', 4E_o, E')$, etc. These extra processes can give rise to "spurious" peaks, i.e., to peaks which are not expected due to the primary scattering configuration. These peaks may occur in scans of any energy transfer, but they can be particularly bothersome for the high energy measurements where the magnetic scattering is small and the resolution is coarse. However, the positions of these peaks can be calculated and often avoided, and the cross section can be measured under different experimental arrangements and checked for consistency of results. This is time consuming, though, and these spurious peak processes are one of the major problems with triple-axis spectrometers. A second low efficiency monitor has also been placed between the sample and analyzer to detect Bragg scatterings from the sample, which can also give rise to spurious peaks in the scans.

Another problem is associated with multiple Bragg reflections in the monochromator crystal. The intensity of these multiple reflections is generally much smaller than that of the primary scattered beam, but at high incident energies multiple reflections may become significant. For example, with the Be(0002) reflecting, a double-Bragg scattering

can occur which will give an effective (0001) plane scattering at 2λ ($E_o/4$). If E_o is high, $E_o/4$ may be near the peak flux of the reactor spectrum, and therefore an appreciable number of neutrons with a wavelength of 2λ may be reflected into the incident beam. This will introduce spurious counts into the monitor, and hence the scattering cross section (per unit monitor interval) will appear to be reduced. By using the Be($10\bar{1}1$) as a monochromator, multiple Bragg scatterings are reduced. Still, a careful check must be made for these effects.

For high incident energies, incoherent scattering processes occurring in the monochromator may contribute an appreciable number of neutrons to the beam incident onto the sample. This may be easily corrected for by setting the monochromator crystal off the Bragg peak and counting the number of neutrons incoherently scattered. At the highest energies used the incoherent scattering amounted to no more than 5% of the incident flux, and the spin wave intensities have been corrected for it.

Finally, Bragg reflections may occur in the sample, and "rob" the incident beam of neutrons inside the sample. This effect may become more important for the higher energies (shorter wavelengths) since more Bragg reflections can occur. To check the magnitude of this effect, the beam transmitted through the nickel crystal was monitored as a function of energy. No appreciable effect was observed, and no corrections have been made for it.

Spin Wave Linewidth Analysis

As the temperature is raised from T = 0°K, the spin waves acquire* a finite lifetime and hence a spread (uncertainty) in energy. If the resolution of the spectrometer is comparable to or smaller than the intrinsic linewidth, the observed peak will become measurably broader at the higher temperatures and then spin wave linewidths may be obtained from the data.

Since the scans performed were constant-E scans (varying $\vec{Q}$), the measured widths are in $\vec{Q}$ rather than energy. But if the energy widths are not too large ($\Delta E/E \ll 1$) or if the dispersion surface is essentially planar, then the energy widths can be obtained directly by

$$\Delta E = \left|\vec{\nabla}_{\vec{q}}\omega\right| \Delta q \ . \tag{44}$$

Above T_C, however, the energy widths are not small. Nevertheless, equation 44 will still give rough estimates of the energy widths because the dispersion surface does not have a great deal of curvature, at least at the higher energies. More reliable linewidths can be obtained by numerically folding the scattering cross section with the resolution function and matching the calculations with the measurements. Rather extensive numerical calculations of this type have been made. These resolution effects and the specific assumptions used to extract the

*For an itinerant electron ferromagnet there may be a finite linewidth at T = 0°K due to the Stoner states.

intrinsic widths of the excitations will be discussed when the linewidth data are presented in Chapter 4.

Samples

Since we want to measure the magnetic scattering, it is worthwhile to try to enhance the magnetic scattering as much as possible, while at the same time reducing other types of scattering processes which are not of interest and which can increase background and sometimes give rise to spurious peaks. The larger the samples, the more intense all the scattering will be, so that counting times may be shortened and hence the relative amount of "room background" will be reduced. The nuclear cross sections can sometimes be reduced by growing crystals with particular isotopes. This can reduce the general background scattering from the sample and eliminate some types of scattering processes (for example, incoherent scattering). This is particularly important for measurements of the high energy spin waves because the magnetic scattering is weak and the counting times are long. Four different samples have been used in these investigations.

Pure iron undergoes a bcc to fcc transformation[89] at $\sim$1180°K, which makes the growth of large single crystals very difficult. However, with the addition of $\gtrsim$4% silicon the high temperature fcc phase is by-passed. A large single crystal can then be easily grown from the melt. The majority of the iron measurements were made on a single crystal of ^{54}Fe (12 at. % Si) weighing 180 gm. The crystal was approximately cylindrical in shape with the [110] crystallographic axis tilted $\sim$25° from the cylinder axis. The nuclear scattering amplitudes of ^{54}Fe

and Si are equal ($b = 0.42 \cdot 10^{-12}$ cm), so that use of the isotope of iron eliminates incoherent scattering, as well as reducing all the coherent nuclear scattering cross sections by a factor* of ~ 5.2 ($\bar{b}_{Fe} = 0.96$).

With that much silicon added, the magnetic properties are considerably altered from pure iron. The spin wave stiffness parameter decreases from 280 meV-Å^2 to 230 meV-Å^2, and the transition temperature decreases from 1042°K to 970°K. Thus in order to make certain that the magnetic behavior of the alloy is really indicative of iron, additional measurements were carried out on a single crystal of pure iron (with the natural distribution of isotopes). This sample was a cylinder weighing 23 gm, with approximately the same orientation as the alloy crystal. At room temperature, the signal to noise ratio was more than seven times better for the alloy (mainly due to sample size), and this ratio increased as the temperature increased. Of course, no measurements for pure iron could be carried out above 1180°K.

All the temperature dependent measurements for nickel (nickel is fcc over the entire temperature range of the solid) were taken on a single crystal of ^{60}Ni weighing 134 gm. Use of the isotope eliminates the large incoherent scattering found in nickel with the natural isotopic distribution. The nuclear coherent scattering is also greatly reduced (by a factor of ~ 13.3), with $\bar{b}_{Ni} = 1.03$ and $b_{^{60}Ni} = 0.282$. Without the use of the isotope, these measurements on nickel would be impossible.

---

*Recall that the coherent nuclear scattering cross section = $4\pi|\bar{b}|^2$.

Some rather anomalous neutron scattering results have been reported for nickel recently.[90] These measurements were made at room temperature on a "natural" single crystal of nickel. For comparison with these results and our own results on ^{60}Ni, a very limited number of measurements at room temperature were made on a natural single crystal of nickel. The sample weighed 99 gm and was in the form of a cylinder that had been cut in half along the cylinder axis.

CHAPTER IV

EXPERIMENTAL RESULTS AND DISCUSSION

The majority of the measurements were taken around the (110) and (111) reciprocal lattice points in iron and nickel, respectively. These reciprocal lattice points correspond to the smallest $\vec{\tau}$ vectors in their respective lattices, and hence $F(\vec{K})$ is large here. It is not practical to measure the excitations around the (000) reciprocal lattice point because the momentum and energy conservation relations (given by equations 39 and 40) cannot be satisfied for reasonable incident and scattered neutron energies.

Since the dispersion relations are isotropic in $\vec{q}$, and due to time limitations on the spectrometers, the measurements were concentrated in the [110] direction in iron, and the [111] direction in nickel. However, enough data were obtained in the other symmetry directions to establish that the spin wave dispersion relations, as well as the spin wave lifetimes, are isotropic in $\vec{q}$ over the entire temperature range covered. The Stoner excitations, on the other hand, are not isotropic in $\vec{q}$. Because of the long counting times required to measure the high energy spin waves, the temperature dependence of the spin wave-Stoner mode intersections was only determined for the [110] direction in Fe(Si), and the [111] direction in Ni.

Results for Iron

Room Temperature

Extensive temperature dependent measurements on pure iron would be too time consuming due to the small sample available. Thus the objective in collecting data on the pure iron was to determine if the results for the Fe(Si) crystal were indicative of Fe. The limited data obtained at room temperature are in excellent agreement with the previous measurements already reported,[60,67] and a value of D = 280 meV-Å^2 was obtained.

Since no triple-axis data have been reported for Fe(12% Si), the spin wave dispersion relations were examined thoroughly. Figure 12 shows the low energy spin wave dispersion relations for the principal symmetry directions. Measurements were taken in all three symmetry directions and around at least two different reciprocal lattice points at all the energies shown, but not all the points can be plotted in the figure because the results overlap. Within experimental error, the dispersion relations are isotropic in $\vec{q}$. If equation 5 is fit to these data, then the values of D = 230 ± 7 meV-Å^2 and β = 0.82 ± 0.20 Å^2 are obtained. The errors quoted are the least-squares statistical errors. The solid curve in the figure corresponds to equation 5, whereas the dotted curve is just the leading order quadratic term. These results are in reasonable agreement with the "diffraction method" results of Antonini et al.,[47] although their results are for alloys of 7 and 15% Si. Generally, the triple-axis method is considered to be more reliable since the excitations are measured directly, and without applying a

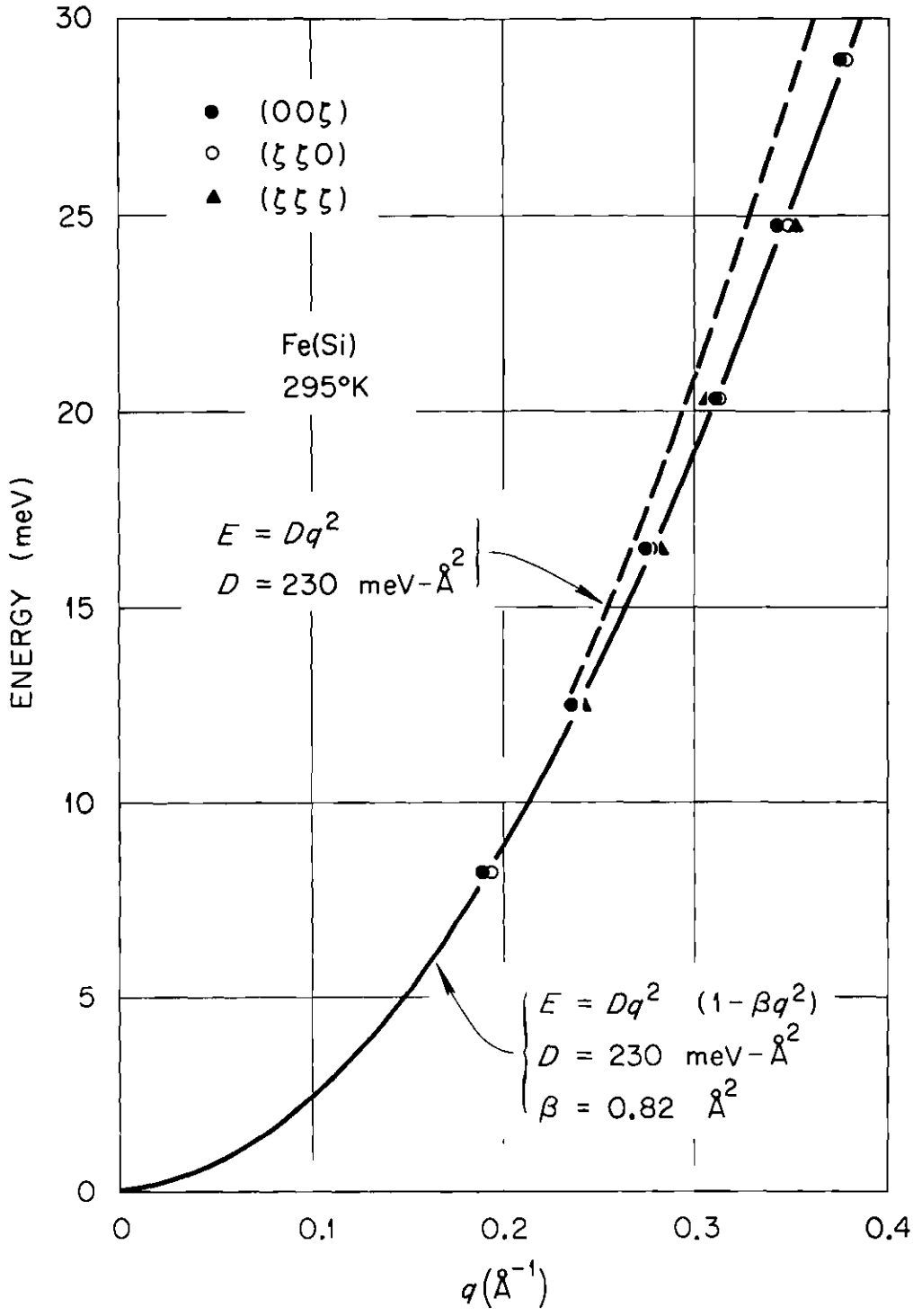

Figure 12. Room Temperature Spin Wave Dispersion Relations in the Principal Symmetry Directions for Fe(12% Si)

magnetic field. In particular, the diffraction method tends to give systematically larger values[8] of β (for β negative), which is apparent in their data at the larger values of $\vec{q}$.

It is noteworthy that the present results, as well as those of other authors,[8] show that the magnon and phonon dispersion curves cross without any apparent interaction. Therefore the magnon-phonon coupling must be very small. It should also be noted that the Heisenberg nearest-neighbor model does not give a good fit to the data, so that if the Heisenberg model is appropriate at all, the exchange interaction must be of long range.

The spin wave intensities in the [110] direction were measured as a function of energy, and at $\sim$110 meV the spin wave intensity begins to decrease rapidly (see Fig. 14). This rapid decrease in intensity is interpreted as the intersection of the spin wave modes with the region of high density of Stoner excitations. Note that the spin wave modes only exist over about half of the Brillouin zone (the zone boundary in the [110] direction is at 1.55 Å^{-1}). Although exhaustive measurements like those of Mook and Nicklow[67] were not carried out, due to the extremely long counting times required to make spin wave intensity measurements near the spin wave-Stoner mode intersection, it is clear that the intersection occurs at a higher energy than in Fe(4% Si). With consideration of the resolution used for these measurements* we

---

*At $\hbar\omega$ = 100 meV the energy resolution was $\sim$10%, which is very coarse in comparison with the resolution usually employed in triple-axis measurements.

can estimate an intersection point of ∿115 meV, which is considerably higher than the ∿95 meV they observed. This observation may be understood in terms of the band model if the effect of adding the silicon is simply to dilute the magnetic lattice. The "Stoner modes" in the localized model are at very high energies, outside the spin wave band. This localized limit can be obtained in the band model by widely separating the atoms. As the silicon concentration increases, the average spacing of the magnetic atoms increases, so that we might expect the region of Stoner modes to increase in energy, even though the spin waves lower in energy.

Temperature Dependent Results

The magnetic scattering was measured from room temperature through the ferromagnetic transition temperature and up to 1.4 T_C (1360°K). Although the furnace could go higher in temperature, the vapor pressure of the sample would have become high enough that a significant portion of the sample would have been lost over a period of days, and this was undesirable because the ^{54}Fe isotope is very expensive. The scattering was identified as magnetic in origin both by continuously following the evolution of the scattering from low temperatures, and from the dependence of the scattering intensity on the magnetic form factor $F(\vec{K})$. Spin waves with the same $\vec{q}$ were measured around different reciprocal lattice points and with a variety of experimental arrangements to detect any spurious scattering effects.

Figure 13 shows the temperature dependence of the spin wave spectra for Fe(12% Si) in the [110] direction. As the temperature is

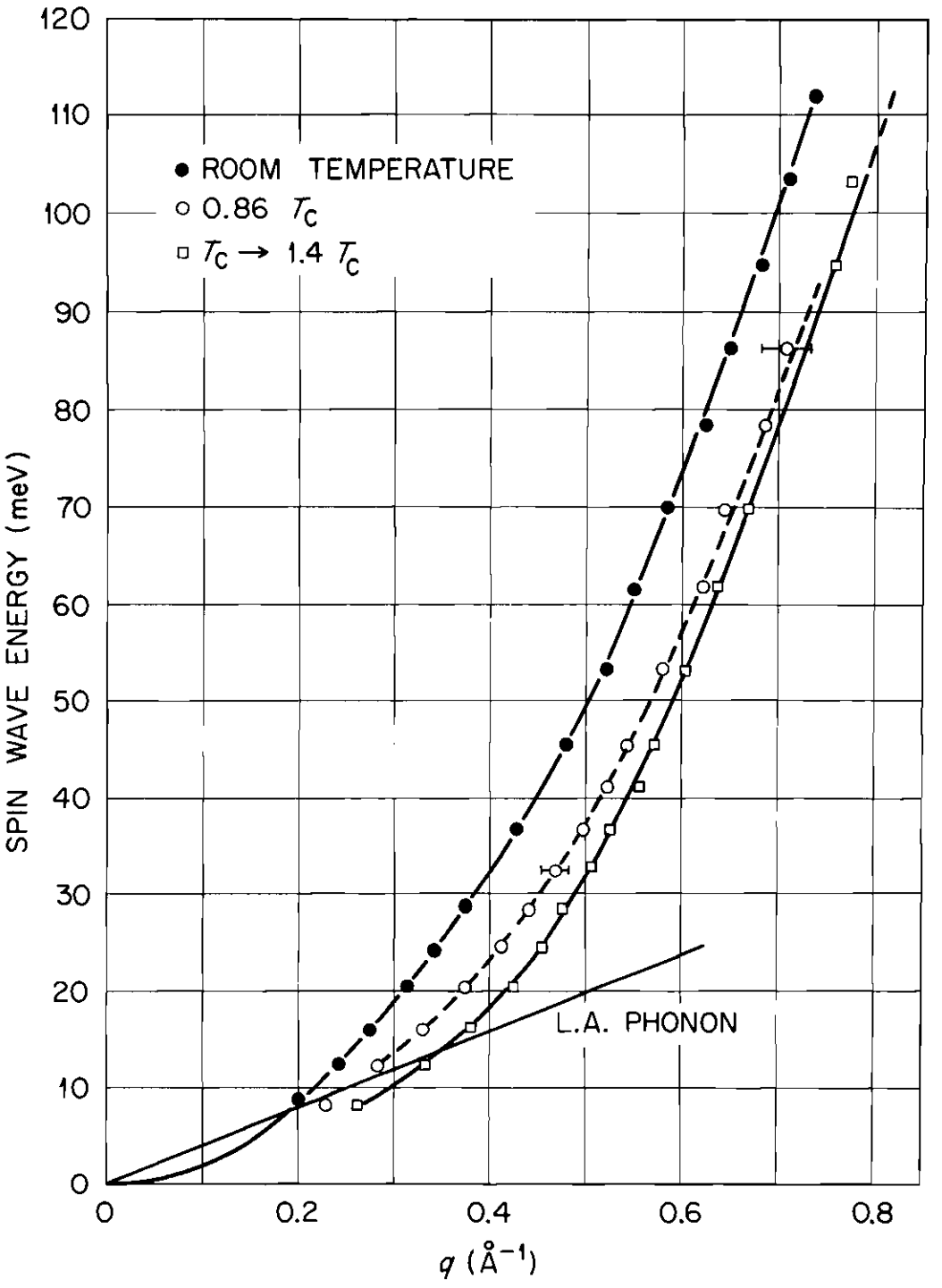

Figure 13. Fe(Si) Spin Wave Spectra at a Series of Temperatures

increased, the spin waves lower in energy. Outside the immediate vicinity of the origin, however, the spin waves persist as well defined excitations up to and above T_C, with no further renormalization of the dispersion relations occurring for $T > T_C$. This behavior is in marked contrast to the behavior observed in the small wavevector region,[60,64] where the spin waves were found to become overcritically damped just below T_C.

If the expression $E = Dq^2$ is fit to the data, then D is found to decrease from 230 meV-Å^2 at room temperature to ∿140 meV-Å^2 above T_C. About a 15% decrease in D can be expected[8,52] in going from T = 0°K to room temperature, so that the overall renormalization is ∿50%. However, the fit to the data above T_C was not very good, and including β in the fit (equation 5) results in a small value of D and a large negative value of β. An adequate fit to the disperion relation could not be achieved without including several higher order terms, and the curve in the figure for $T > T_C$ is a fit to a higher order polynomial expansion in the wavevector q. Unfortunately, the theoretical form of the dispersion relation is unknown. However, it was expected theoretically that the long wavelength spin waves should become overcritically damped just below T_C, and that D(T) should follow a power law of the reduced temperature (which means that $D(T) \to 0$ as $T \to T_C$). This behavior was confirmed experimentally for both iron[60,64] and nickel.[61]

The spin wave energies for pure iron were found to be ∿15% higher in energy (for a given value of q) than in the Fe(Si), and well defined spin waves were observed above T_C. Only a limited region of energy was

explored, though, and of course no measurements could be made above the solid state transformation. The highest temperature for which measurements were taken on pure iron was 1150°K, which corresponds to $T/T_C \simeq 1.1$ ($T_C = 1042$°K).

Figure 14 shows the spin wave intensity as a function of energy at room temperature ($T/T_C = 0.30$) and at 1.28 T_C for the [110] direction of Fe(Si). The method of arriving at these spin wave intensities has been described in Chapter III. It is clearly seen that the location of the abrupt spin wave intensity decrease, interpreted as the intersection of the spin wave modes with the Stoner continuum of excitations, changes little, if any, with temperature. This is an interesting result since the simplest theory (as discussed in Chapter II) would predict a substantial decrease in energy of the Stoner modes as the band splitting collapses with $T \rightarrow T_C$. It also appears that the slow fall off in intensity with energy at room temperature is absent at high temperatures. It should be noted that slow variations in the measured intensities over large energy ranges could be due, at least in part, to systematic experimental factors as discussed in Chapter III.

A few high energy spin wave measurements are shown in Figure 15 for room temperature and 1240°K. It can be seen that the spin waves are broadened in $\vec{q}$ and reduced in intensity at 1.28 T_C, but they are still easily observable. The solid curves are the result of a least-squares fit to a gaussian distribution plus sloping background. The sloping background in these scans is due to the small scattering angles Φ used in these measurements. At small values of Φ, a substantial

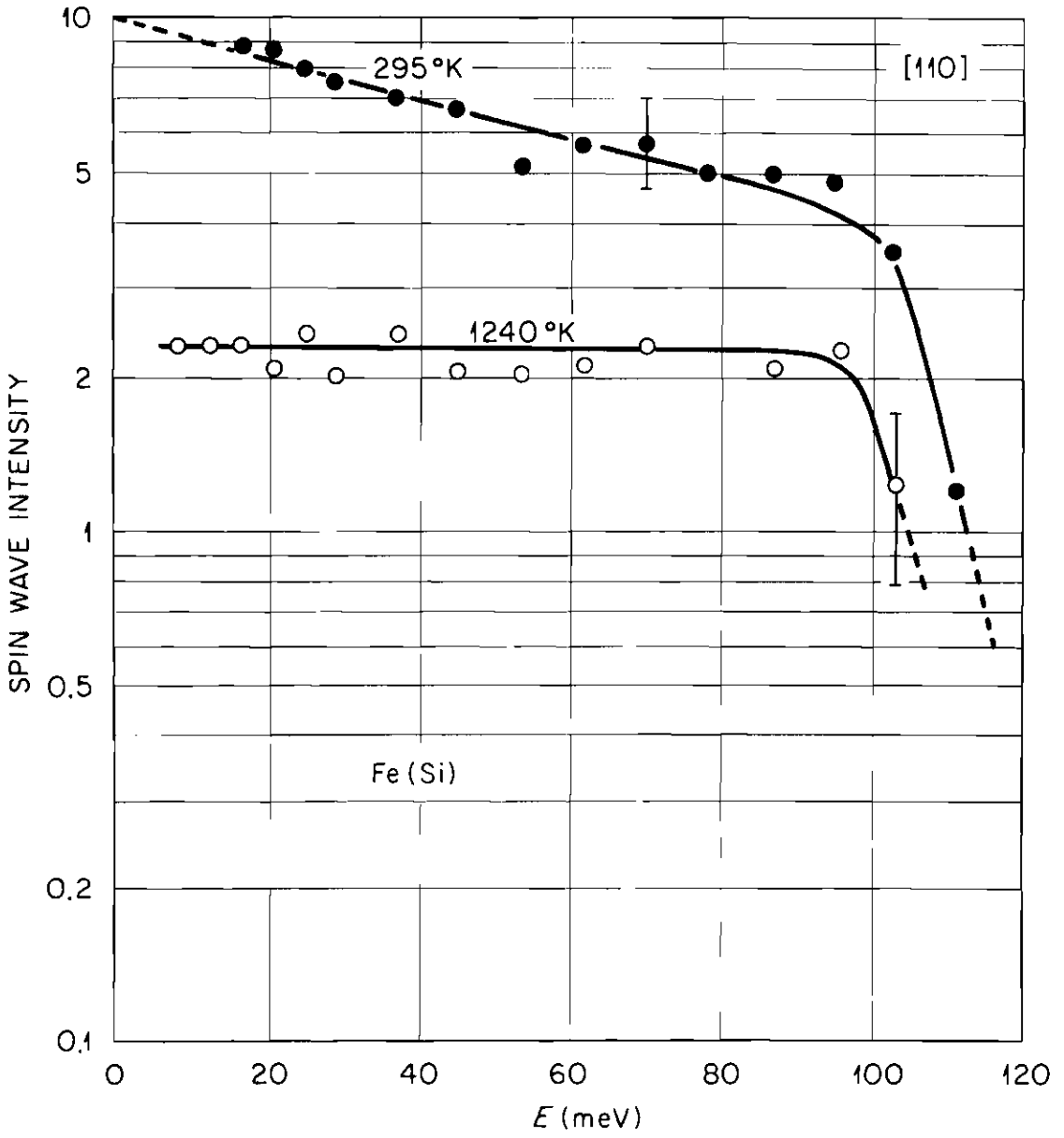

Figure 14. Spin Wave Intensity Versus Energy at T = 295°K and T = 1240°K for the [110] direction

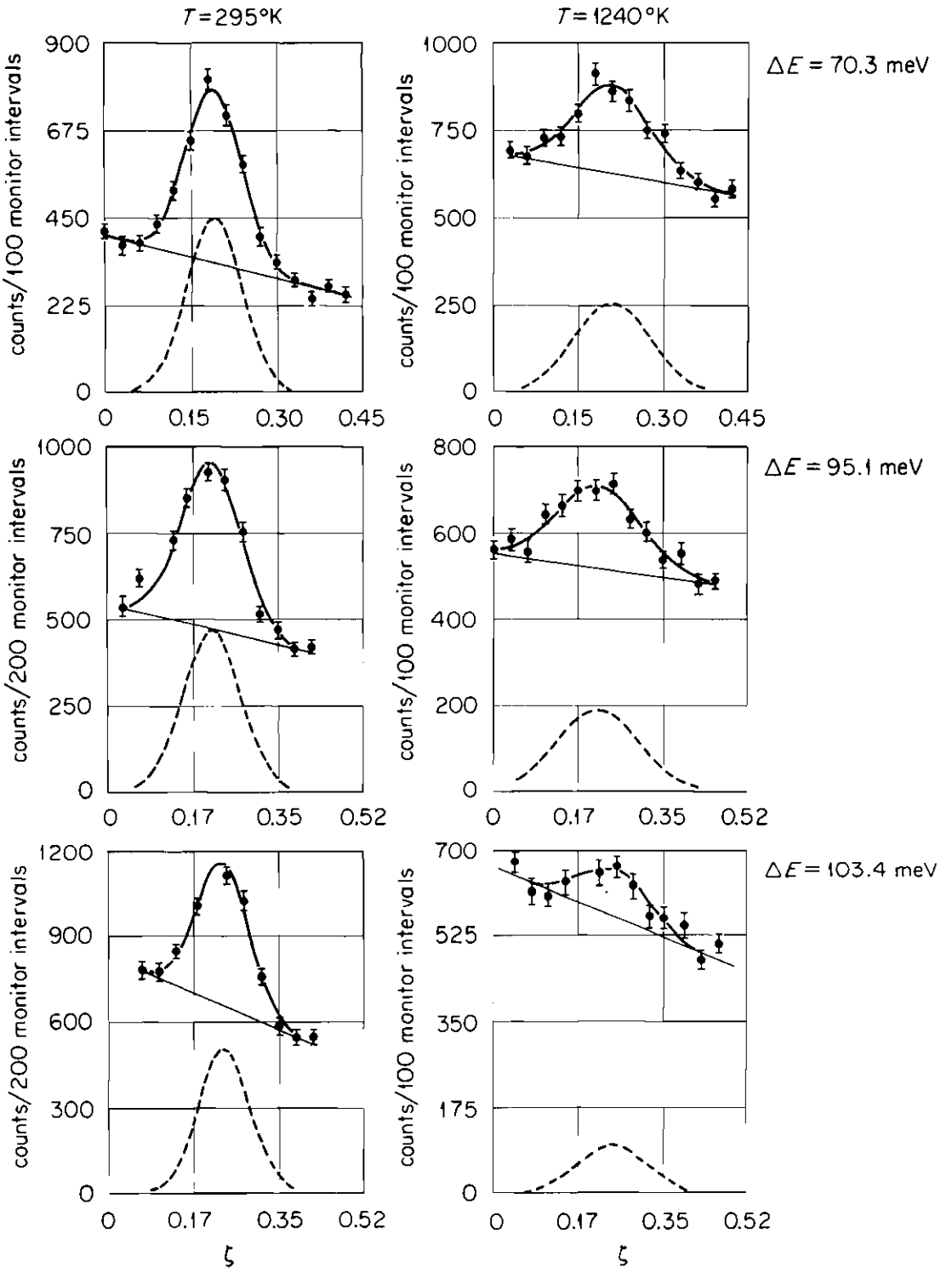

Figure 15. Several High Energy Spin Waves at 295 and 1240°K for $\vec{Q} = (1+\zeta, 1+\zeta, 0)$

background occurs due to air and furnace scattering of the incident beam, and this background decreases with increasing Φ.

The overall spin wave intensity is reduced at higher temperatures, and Figure 16 shows the temperature dependence of the spin wave intensity for a fixed energy transfer of 29 meV. This temperature dependence is typical of all the spin wave intensities. The intensity falls fairly rapidly with temperature, and apparently follows an exponential law at high temperatures. One contribution to this decrease is the temperature dependence of the Debye-Waller factor. To check the magnitude of this effect, the intensities of a few phonon groups were also measured. Below T_C, the interpretation of the temperature dependence of the phonon intensities is complicated by the fact that the intensity is partly magnetic in origin, due to magnetovibrational scattering. This effect is easily observable. The phonon intensities fall off fairly rapidly up to the transition temperature, but at T_C the rate of decrease abruptly changes. Above T_C, the phonon intensities decrease slowly, in accordance with calculations of the temperature dependence of the Debye-Waller factor, while the magnon intensities decrease about four times more rapidly.

In addition to the spin wave positions and intensities, the linewidths were also measured. Figure 17 shows the observed full-width at half-maximum of the spin waves at 8.27 and 29.0 meV as a function of temperature. Note that since the scans were taken with the energy transfer held constant, and by varying $\vec{q}$, the widths are in $\vec{q}$ rather than energy. The resolution of the spectrometer has not been removed

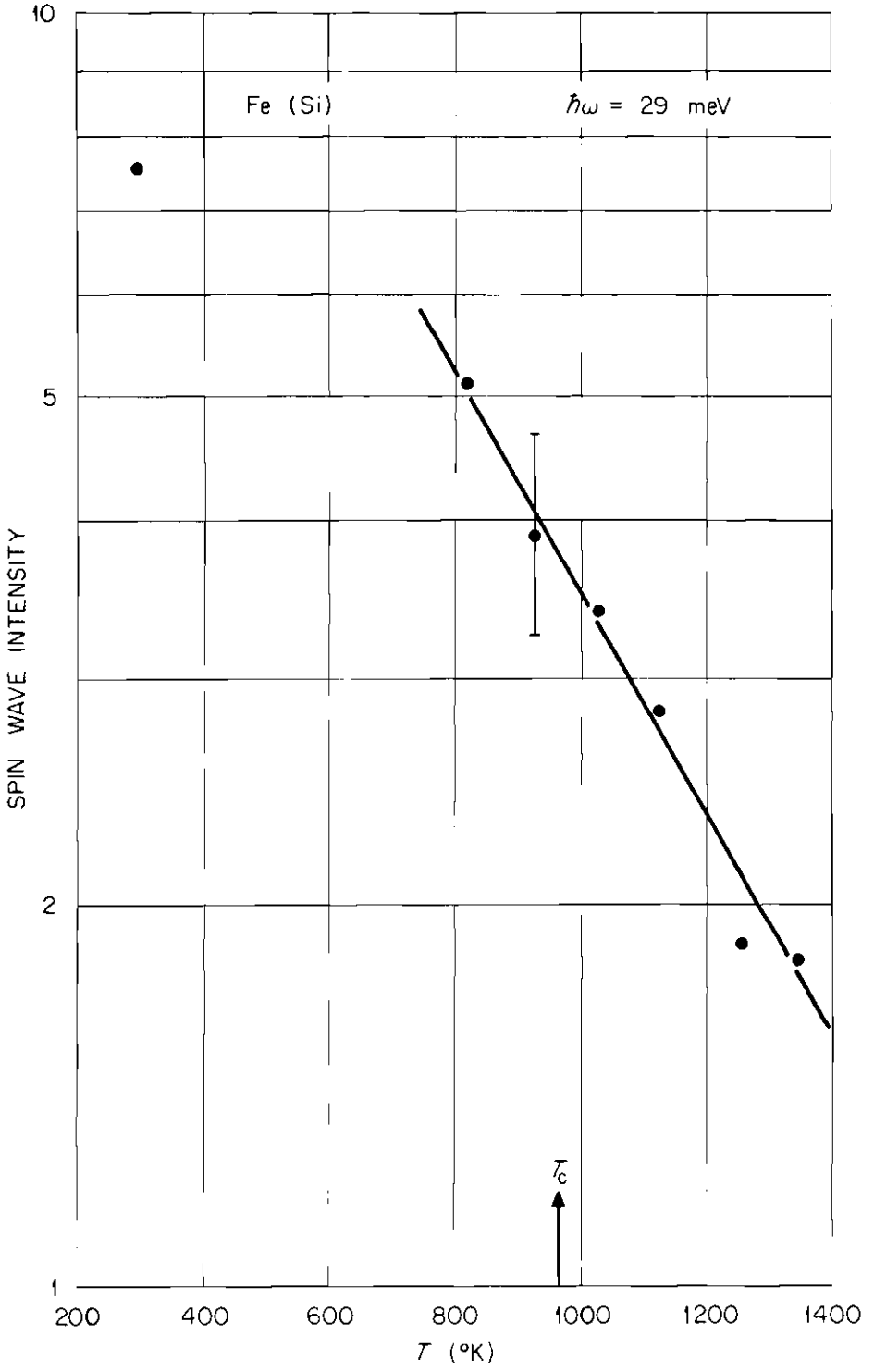

Figure 16. Spin Wave Intensity Versus Temperature

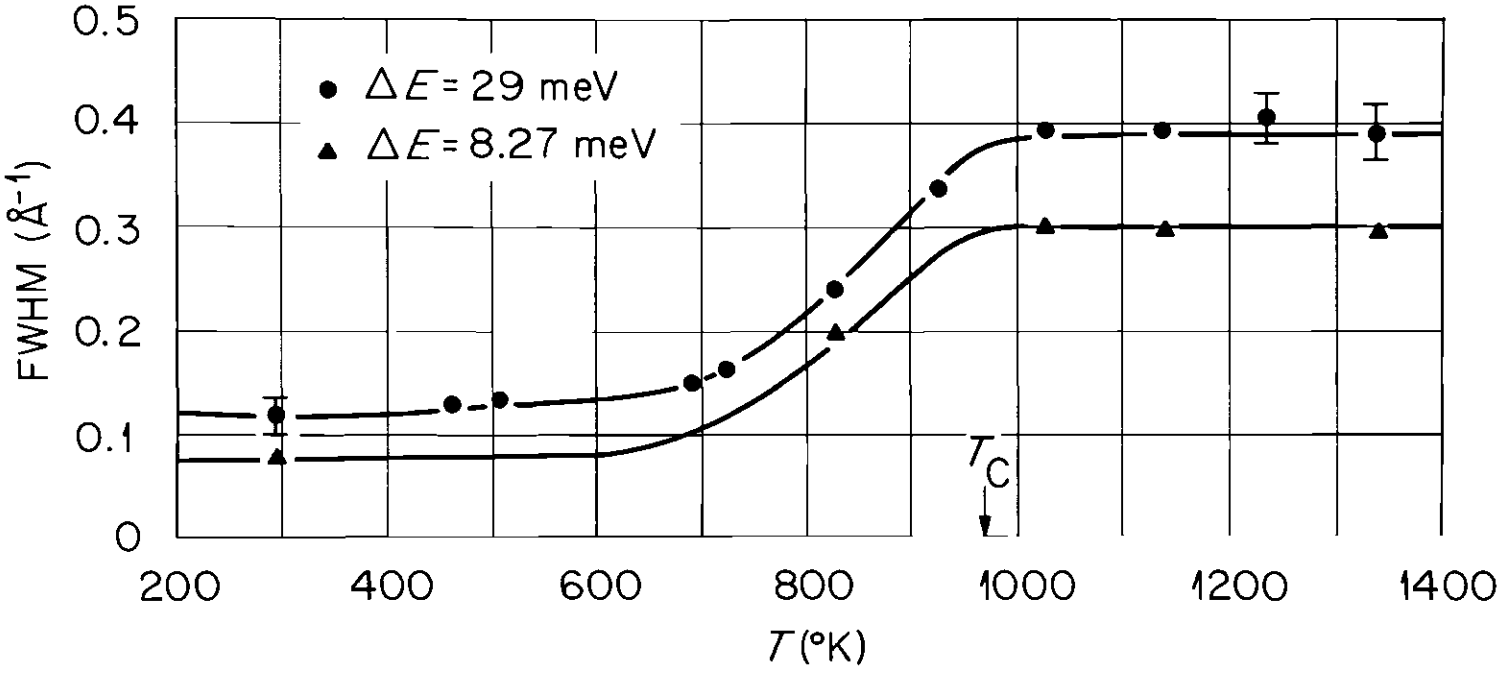

Figure 17. Observed Full Width at Half Maximum for Spin Waves at 8.27 and 29.0 meV as a Function of Temperature

from these widths, and the widths at room temperature may be taken as a measure of the resolution. Detailed resolution calculations showed that the intrinsic widths at room temperature are very small. As the temperature is raised to T_C, the spin waves broaden considerably. Above T_C, however, no further broadening occurs.

The widths were found to be isotropic in $\vec{q}$, and the majority of the measurements were therefore taken in the [110] direction. Figure 18 shows several scans just below and above T_C for 8.27 meV. Two peaks are observed, the sharp peak being due to the longitudinal phonon, and the broad peak being due to the spin wave. Although the presence of the phonon in the midst of the magnetic scattering is undesirable, it does afford a ready comparison of the magnetic and nuclear scattering, and it also gives an indication of the resolution of the spectrometer. Since the phonon is sharp, it may be separated easily from the magnetic scattering. The fits shown were obtained by a least-squares fitting procedure using two gaussian distributions plus background. Of course, if a transverse scan is made ($\vec{q} \perp \vec{Q}$), the longitudinal phonon can be eliminated from the scan, but then the transverse phonon appears (at a different position in $|\vec{q}|$). A variety of different scans was performed, and it was found that consistent results could be obtained by use of the fitting procedures. One interesting point that was observed in the low energy data is that the positions, widths, and intensities of the phonons seem to be unaffected by the presence of the magnons. At the higher energies, of course, there are no phonons in the scans.

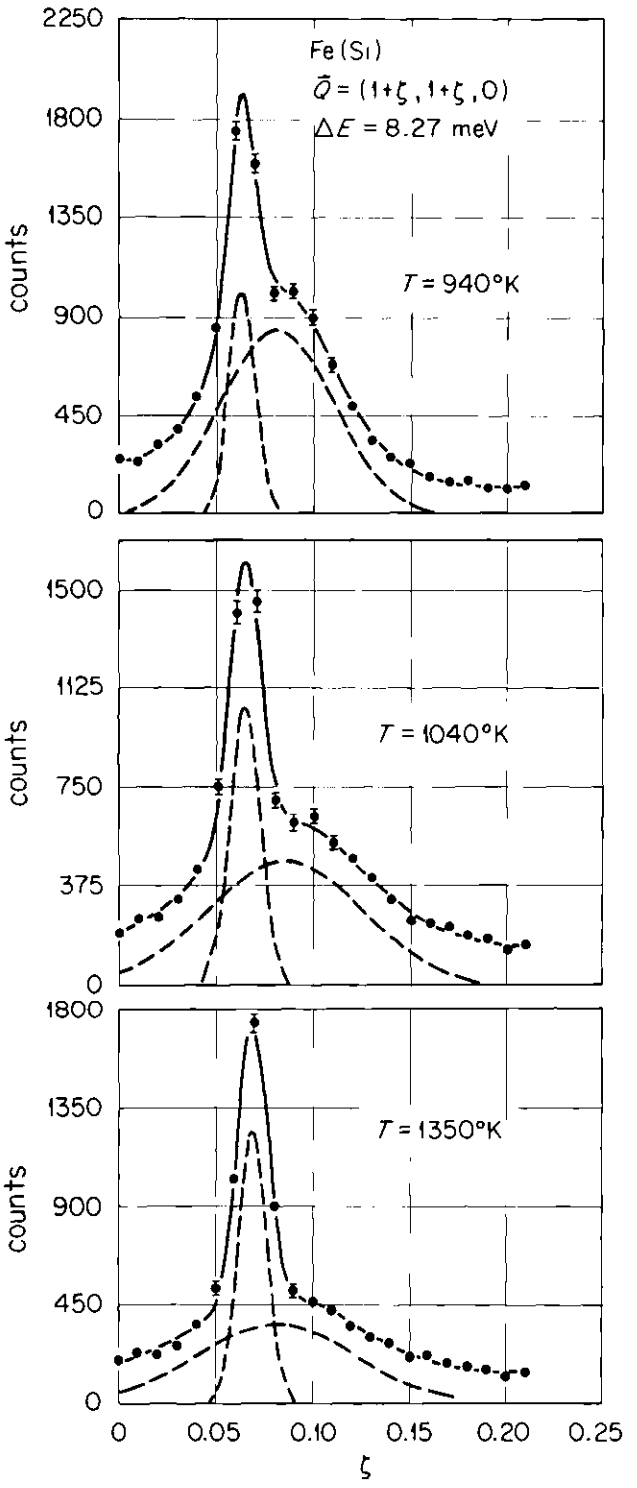

Figure 18. Several Constant-E Scans at 8.27 meV Above and Just Below the Curie Temperature (970°K)

When the intrinsic widths of the excitations are comparable to or larger than the resolution of the spectrometer, then these intrinsic widths may be extracted from the data. Although the widths are measured in q, they are related to the energy widths of the excitations through the dispersion relation. If the energy widths are not too large, then they can be found directly by multiplying the q width by the slope of the dispersion curve (equation 44). Above T_C, however, the energy widths are large, so that some care must be taken to obtain accurate widths. Detailed resolution calculations assuming a gaussian intrinsic energy width have been made, and these calculations indicate that the energy widths obtained via equation 44 should be reduced by no more than $\sim$10% in the worst case. The energy widths presented have been corrected in this manner for the resolution of the spectrometer. It should be kept in mind, however, that for the large widths present above T_C, the energy widths are not necessarily either gaussian or symmetric.

Unfortunately, the theoretical form of the linewidths above T_C is unknown. Since a gaussian distribution in q gives a good fit to the data at high temperatures, this form was assumed for the intrinsic widths. If the natural linewidths in q are lorentzian rather than gaussian, then the intrinsic widths extracted from the measurements will be smaller (by about 15% above T_C) than those obtained with the gaussian analysis, so that the gaussian widths represent in some sense an upper limit. It should be remembered that the quantitative results for the energy widths depend on the assumption of a gaussian linewidth. However, once the q widths and the dispersion relation are known over a

sufficiently large region of the Brillouin zone, the energy widths can be constructed directly, without assuming any particular form for them.

Figure 19 shows the ratio of the energy width to the excitation energy for E = 37.2 meV. The error depicted is the relative error of the widths and does not take into account any possible systematic errors, which are very difficult to evaluate. The ΔE is defined in terms of the standard deviation of a gaussian distribution. As the temperature is raised, a large intrinsic width is induced in the spin wave. Nevertheless, $\Delta E/E < 1$, which has been used as the criterion for the definition of a spin wave excitation. Clearly these excitations do not fall into the category of overcritically damped excitations.

Even though the widths change considerably as a function of temperature, at a fixed temperature the measured (intrinsic) widths in $\vec{q}$ do not change a great deal from scan to scan (energy to energy). Therefore, the energy widths as a function of $\vec{q}$, $\Gamma_{\vec{q}}$, depend to a large extent on the value of the slope of the dispersion curve. Above T_C, $\Delta E/E$ becomes less than one for $E \simeq 8$ meV, and this ratio decreases as E increases over the region where the spin waves exist. Just below the Stoner continuum, $\Delta E/E \sim 0.33$.

If a power law of q ($\Gamma_q \sim q^{\alpha}$) is fit to the results above T_C, then a value of $\alpha = 1.7$ is obtained. But the fit is not particularly good, and the widths are found to follow an exponential law equally well. It should be pointed out that these widths as a function of $\vec{q}$ may be subject to substantial systematic errors since the widths and positions (and hence slopes) are obtained from the same data

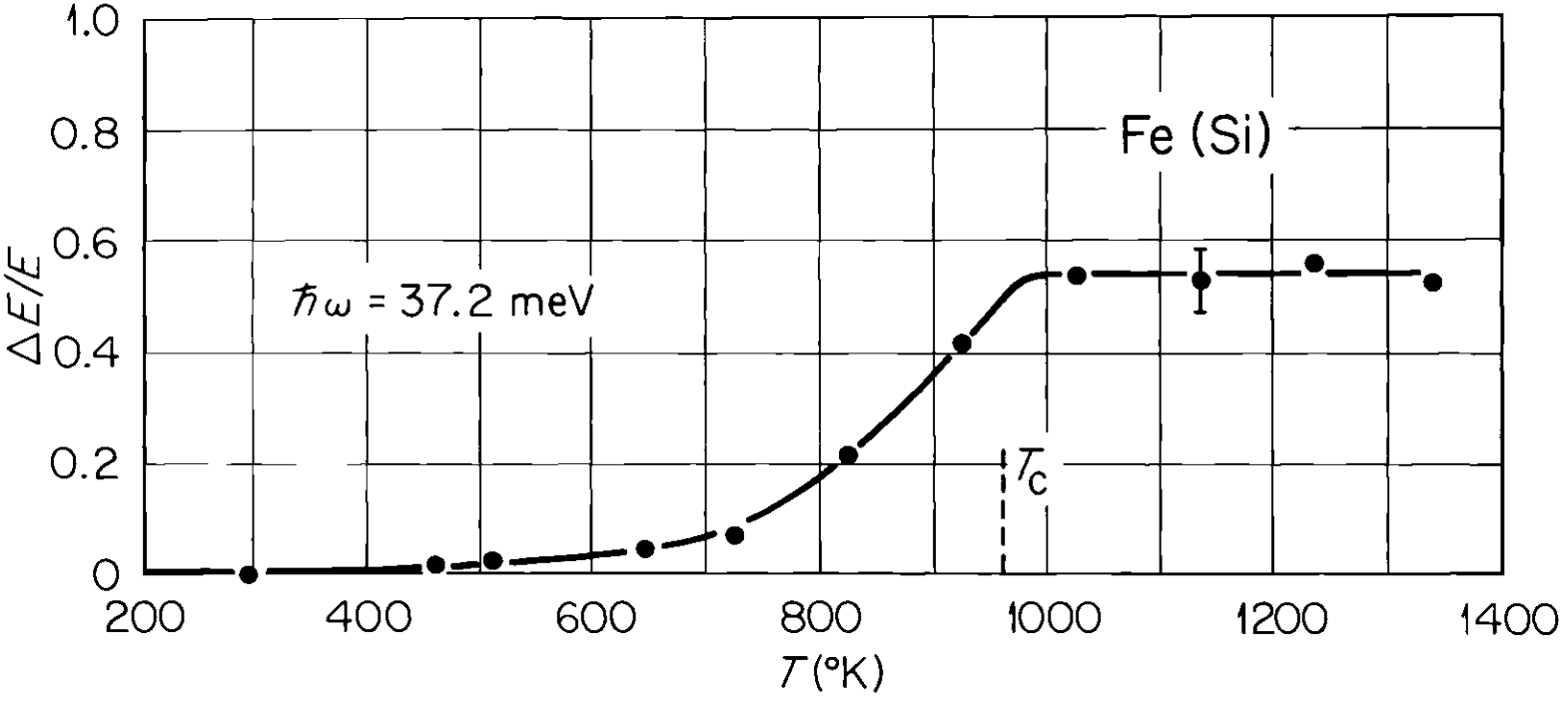

Figure 19. Energy Width ΔE Divided by Energy E for E = 37.2 meV as a Function of Temperature

simultaneously. Unfortunately, once again the theoretical form for Γ_q is unknown.

The intrinsic width in $\vec{q}$ (or $\vec{q}$ itself) at the energy where $\Delta E/E = 1$ should give an indication of the maximum wavelength excitations that can exist above T_C, i.e., the dynamic correlation range. Using the Heisenberg uncertainty relation ($\Delta q \Delta r = 1/2$), we find $\Delta r \sim 5$ Å, which can be interpreted as a "sphere of correlation" with a radius of $\sim$5 Å. The volume of this sphere is $\sim$500 Å^3, so that there are indeed rather long range spin correlations above T_C. It is interesting that this range of correlation is insensitive to the temperature.

Figure 20 shows a "three-dimensional" plot of the measured dynamic susceptibility $\chi(\vec{q},\omega)$ above T_C over the region where the spin waves exist (8 meV $\lesssim$ E $\lesssim$ 115 meV). For E < 8 meV, $\Delta E/E > 1$, although a "hump" of scattering extends downwards to at least 4 meV. This scattering evolves smoothly into the diffuse scattering around Γ. At high energies $\chi(\vec{q},\omega)$ falls off due to the Stoner excitations.

The plot of $\chi(\vec{q},\omega)$ clearly shows that with sufficiently good resolution a constant-$\vec{Q}$ scan would show a spin wave peak. In fact, the scattering function* $S(\vec{Q},\omega)$, corresponding to a constant-$\vec{Q}$ scan, is shown in Figure 21. This has been constructed directly from a series of constant-E scans which contained the same points $\vec{q}$. The resolution of the spectrometer is not contained in the plot, but it should be

*For a constant-$\vec{Q}$ scan $S(\vec{Q},\omega)$ is the same (within a constant) as Im $\{\chi(\vec{q},\omega)\}$ except that $S(\vec{Q},\omega)$ contains the Bose thermal factor.

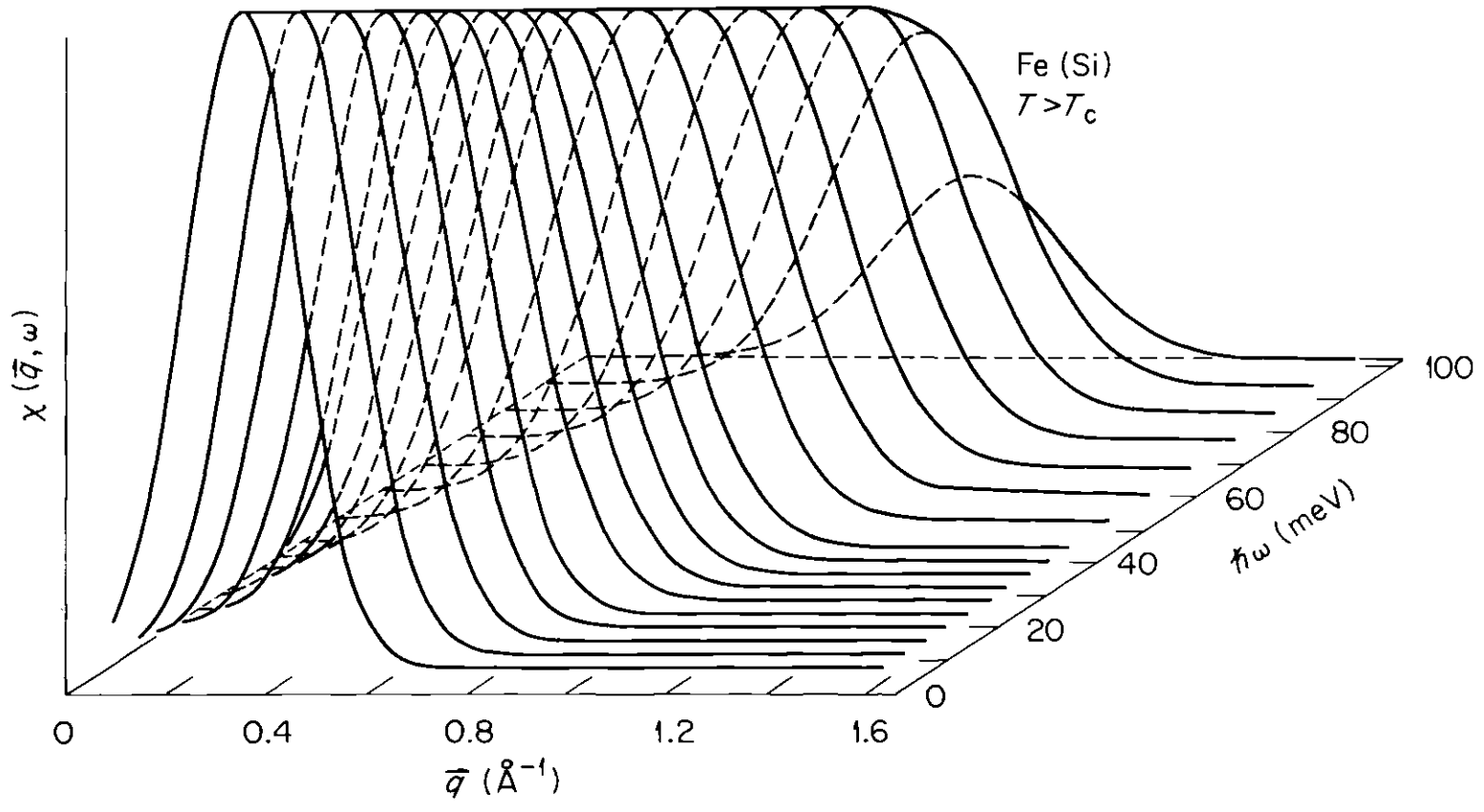

Figure 20. The Measured Susceptibility $\chi(\vec{q},\omega)$ for $T > T_C$

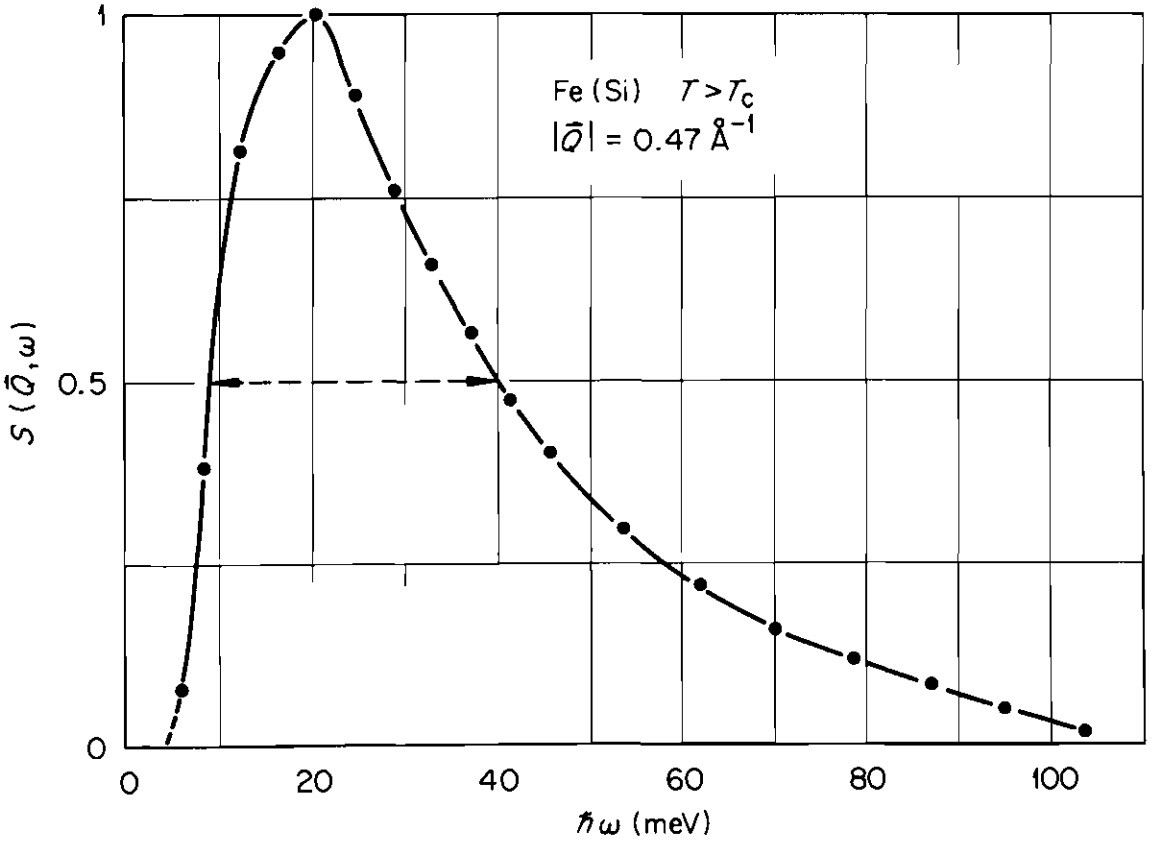

Figure 21. The Scattering Function $S(\vec{Q},\omega)$ Corresponding to a Constant-$\vec{Q}$ Scan, Showing the Lineshape of the Spin Wave Peak Above T_C

pointed out that the actual observed scattering shows an unmistakable spin wave peak.

By comparing Figures 21 and 13, it can be seen that the peak in $S(\vec{Q},\omega)$ occurs at a lower energy than shown on the dispersion curve, and that it is skewed toward higher energies. The skewing is due partly to the positive curvature of the dispersion surface and partly to the increased Δq at higher energies. Skewed linewidths like this are not uncommon in situations where "anharmonic" effects are large. It should be noted that the energy lineshapes and wavevector lineshapes do not have to be the same, as is clear when it is recalled that Figure 21 can be obtained from a series of gaussian distributions in $\vec{q}$.

Finally, since the Fe(Si) alloy crystal has a considerable amount of silicon in it, the question arises whether the linewidths are seriously affected by the silicon. Figure 22 shows a comparison of the intrinsic linewidths for the alloy and for pure iron at an energy of 29.0 meV. The Δq is defined in terms of the standard deviation of a gaussian distribution, and the resolution of the spectrometer has been removed. Clearly, the same behavior is found for both samples, the measured linewidths being slightly smaller for the pure iron. However, the slope of the dispersion curve in pure iron is slightly larger, so that the energy widths (and hence $\Delta E/E$) are essentially identical.

Temperature Dependent Results for Nickel

The ferromagnetic transition temperature of nickel is 631°K, so that room temperature is practically half the Curie temperature ($T/T_C = 0.47$). Consequently, in addition to taking data above room

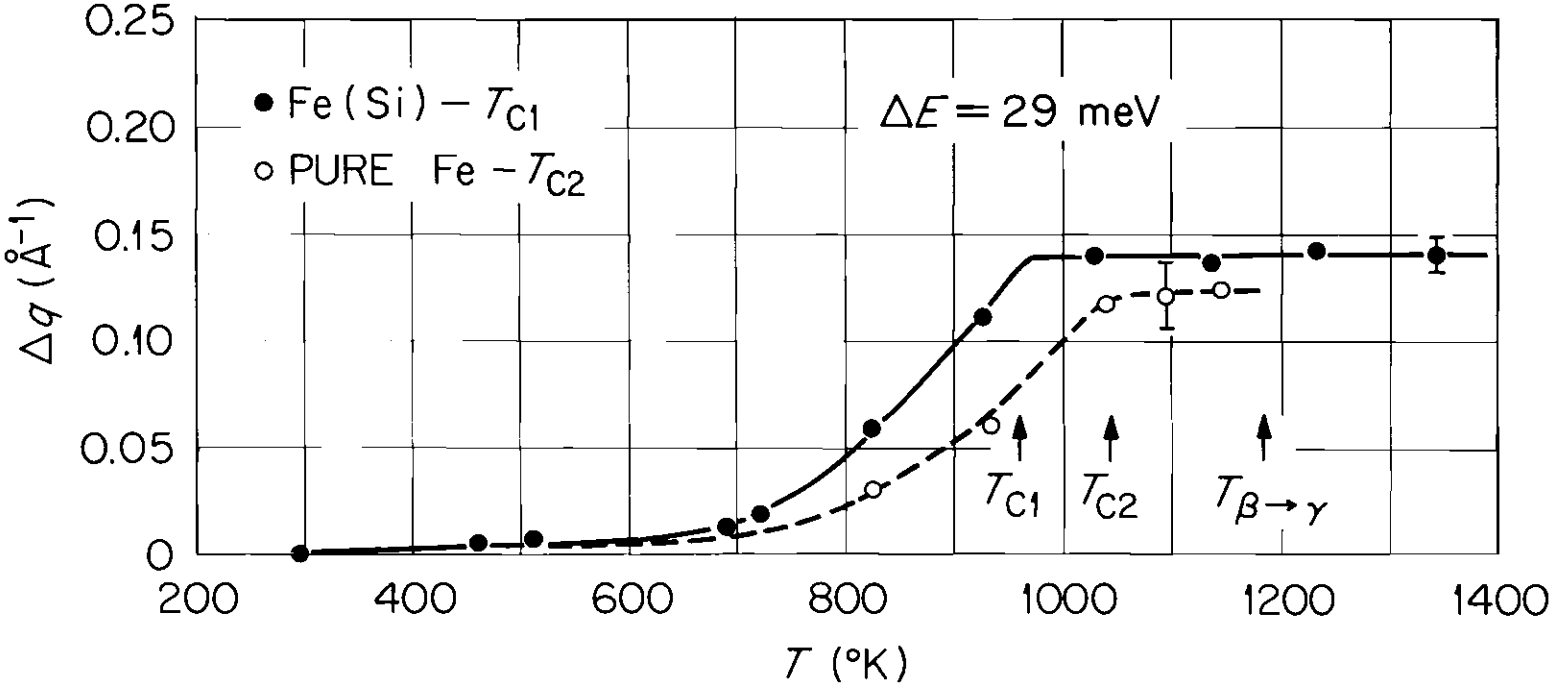

Figure 22. Comparison of the Spin Wave Linewidths as a Function of Temperature for Fe(Si) and Pure Iron

temperature, measurements* were also carried out at 4.2°K in a liquid helium cryostat.

The spin wave dispersion relations, as well as the intrinsic linewidths (at elevated temperatures), were found to be isotropic in $\vec{q}$ over the entire temperature range covered (4.2° → 1260°K). The measurements were therefore concentrated in the [111] direction. The spin wave spectrum over the temperature range $0 < T/T_C \leqslant 2$ is shown in Figure 23. As the temperature is increased up to T_C, the spin waves are seen to lower in energy. Above T_C, the excitations outside the immediate vicinity of Γ persist up to the highest temperatures measured (2 T_C), with no further renormalization of the spin wave dispersion relations occurring. This is in marked contrast to the behavior[61] at very small wavevectors, where the spin waves were found to become overcritically damped just below T_C.

If the dispersion relation $E = Dq^2$ is fit to the data, then D is found to decrease from 550 meV-Å^2 at 4.2°K to 280 meV-Å^2 at and above T_C. It is interesting to note that at room temperature D = 420 meV-Å^2, so that almost half the renormalization of the spin waves occurs from $T/T_C = 0$ to $T/T_C \sim 1/2$, whereas the magnetization decreases by only ∿5%. If equation 5 is fit to the data, then at 4.2° and 295°K the values D = 593 meV-Å^2, β = 0.68 Å^2, and D = 505 meV-Å^2, β = 0.98 Å^2 are obtained. These room temperature values are considerably different than the values obtained by Minkiewicz et al.[61] (see Chapter I). The

*The first data on nickel were taken in collaboration with H. A. Mook and R. M. Nicklow (see Chapter 1) and have been reported.[69] Preliminary reports of the data in this thesis have also been made.[91]

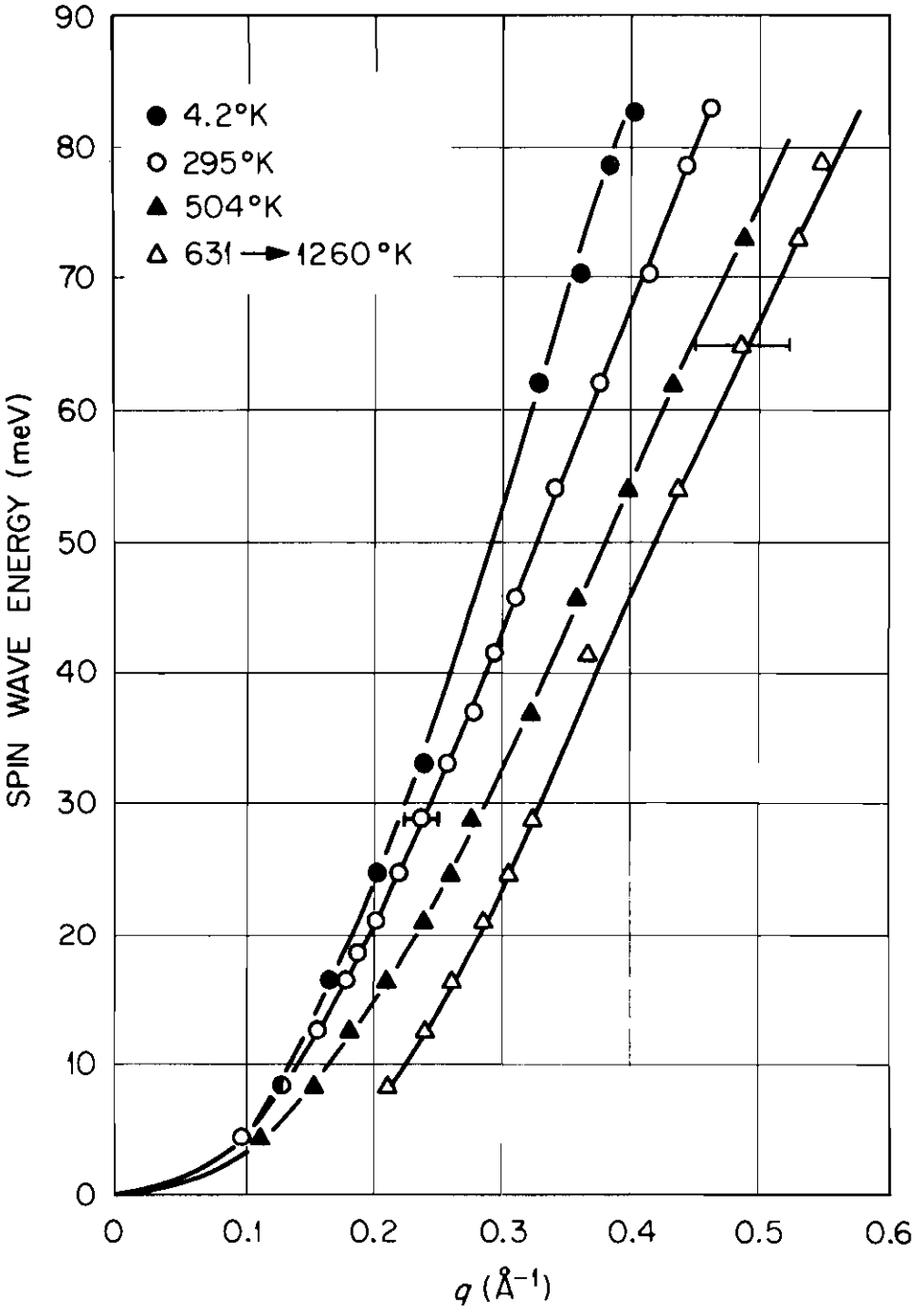

Figure 23. Spin Wave Spectra for Nickel as a Function of Temperature

reason for this discrepancy is because for nickel the spin waves at small $\vec{q}$ lie lower in energy than this fitted dispersion relation would give, so that use of just the higher energy data in the fitting procedure affects the fitted values considerably. It also emphasizes the dependence of D and β on one another. Comparison of the spin wave energies where the two sets of data overlap show that the measured values themselves are in good agreement.

Since the fall off of the spin wave intensity at room temperature was found to occur at a considerably lower energy in the [111] direction than in the other symmetry directions, temperature dependent spin wave intensity measurements near the Stoner cutoff were taken only in the [111] direction. Figure 24 shows the spin wave intensity versus energy at a series of temperatures from 4.2 to 757°K = 1.2 T_C. It is found that the rapid decrease of the intensity occurs at $\sim$85 meV regardless of the temperature. The overall intensity decreases at higher temperatures (in a manner similar to iron), so that these measurements become increasingly more difficult. Since no change in the Stoner cutoff was observable as high as 1.2 T_C, and because of the very long counting times involved, accurate intensity measurements of the high energy spin waves were not continued to higher temperatures. Although the temperature dependence of the spin wave-Stoner mode intersection was not measured in the other symmetry directions, measurements to 100 meV were taken both at low temperatures and above T_C in the [100] direction to be certain that there was no dramatic difference in the behavior of the cutoffs in the other directions.

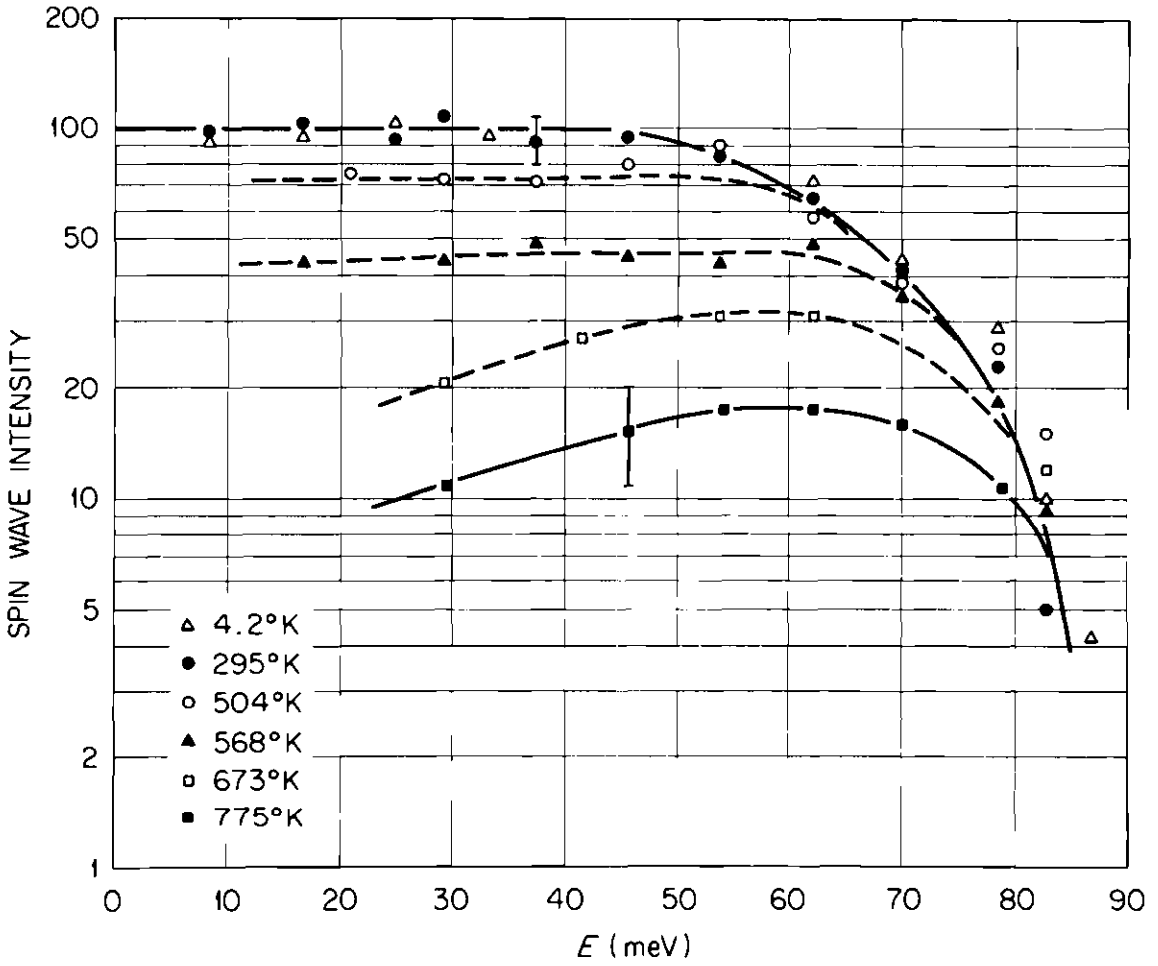

Figure 24. Spin Wave Intensity Versus Energy for the [111] Direction at a Series of Temperatures

One point that should be clarified concerning the fall off of intensity as shown in Figures 14, 20 and 24 is that the energy resolution of the spectrometer has not been taken into account, so that the actual scattering intensity falls off much more sharply than indicated. In fact, within the accuracies of these measurements, the spin wave scattering intensity abruptly falls to zero. When a series of measurements is taken around this cutoff, then each time the resolution ellipsoid passes through the dispersion surface at a higher energy, less of the ellipsoid intersects the surface where the scattering is non-zero, and hence the observed intensity decreases gradually over a range of energy which is comparable to the energy resolution employed in the measurements.

An example of some spin wave measurements at a series of temperatures above and below T_C is shown in Figure 25. These scans are for an energy transfer of 29.0 meV and for $\vec{q}$ in the [111] direction. q is in reduced units and must be multiplied by $2\pi \sqrt{3}/a \simeq 3.08$ Å^{-1} to obtain values in Å^{-1}. These measurements were taken with coarse resolution, and little broadening is observed. With higher resolution, however, the broadening of the spin waves is easily observable, and Figure 26 shows several scans above T_C for an energy transfer of 12.41 meV around the (111) reciprocal lattice point. Four peaks are clearly visible, two broad peaks due to the spin waves at ±q, and two sharp peaks due to the longitudinal phonons at ±q. At room temperature there are four sharp well-resolved peaks, with the spin wave at +q being about twice as high as the phonon at +q. Note that the phonon intensity at -q is

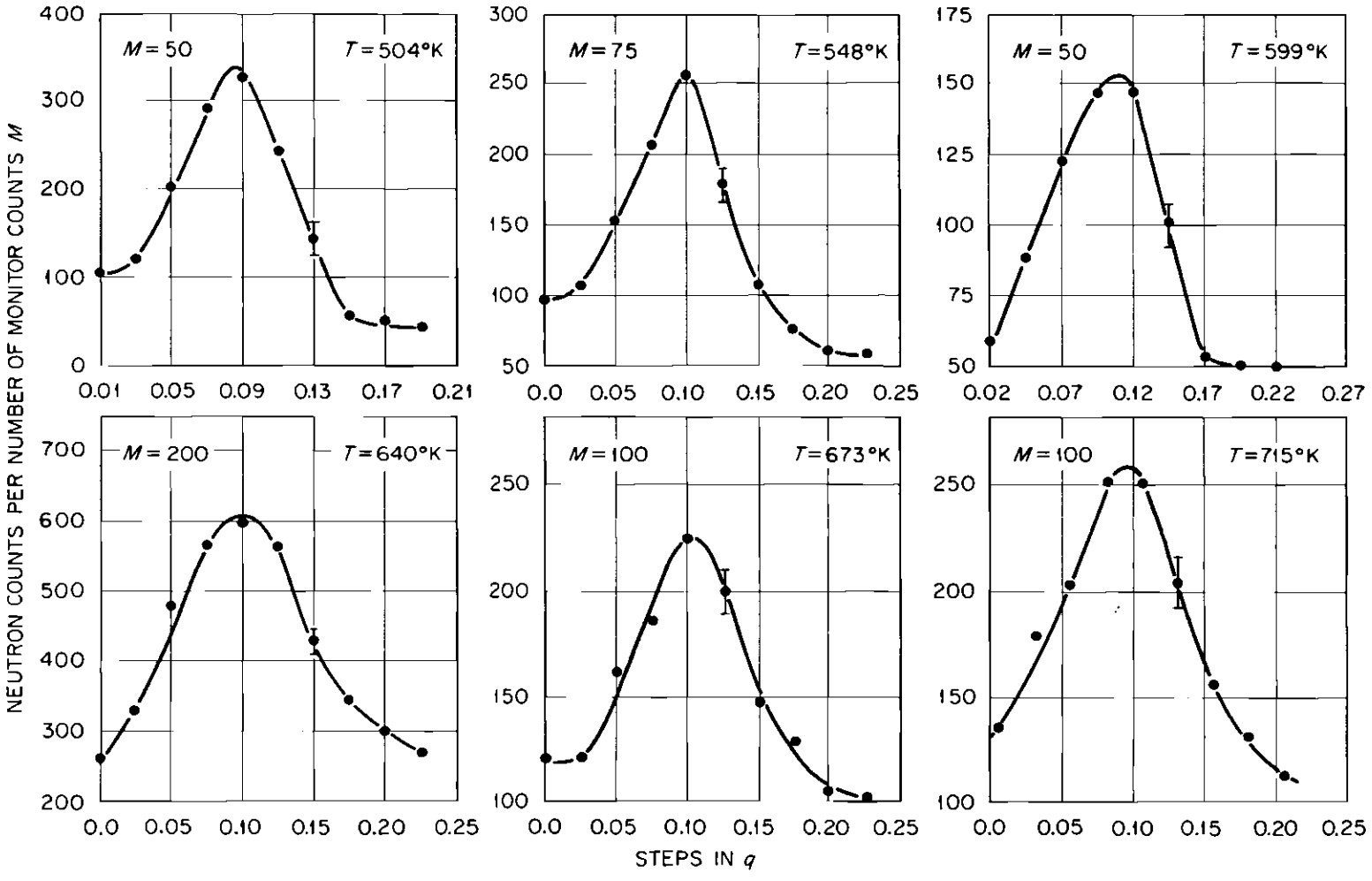

Figure 25. Measured Spin Waves at 29.0 meV for a Series of Temperatures Above and Below T_C (631°K)

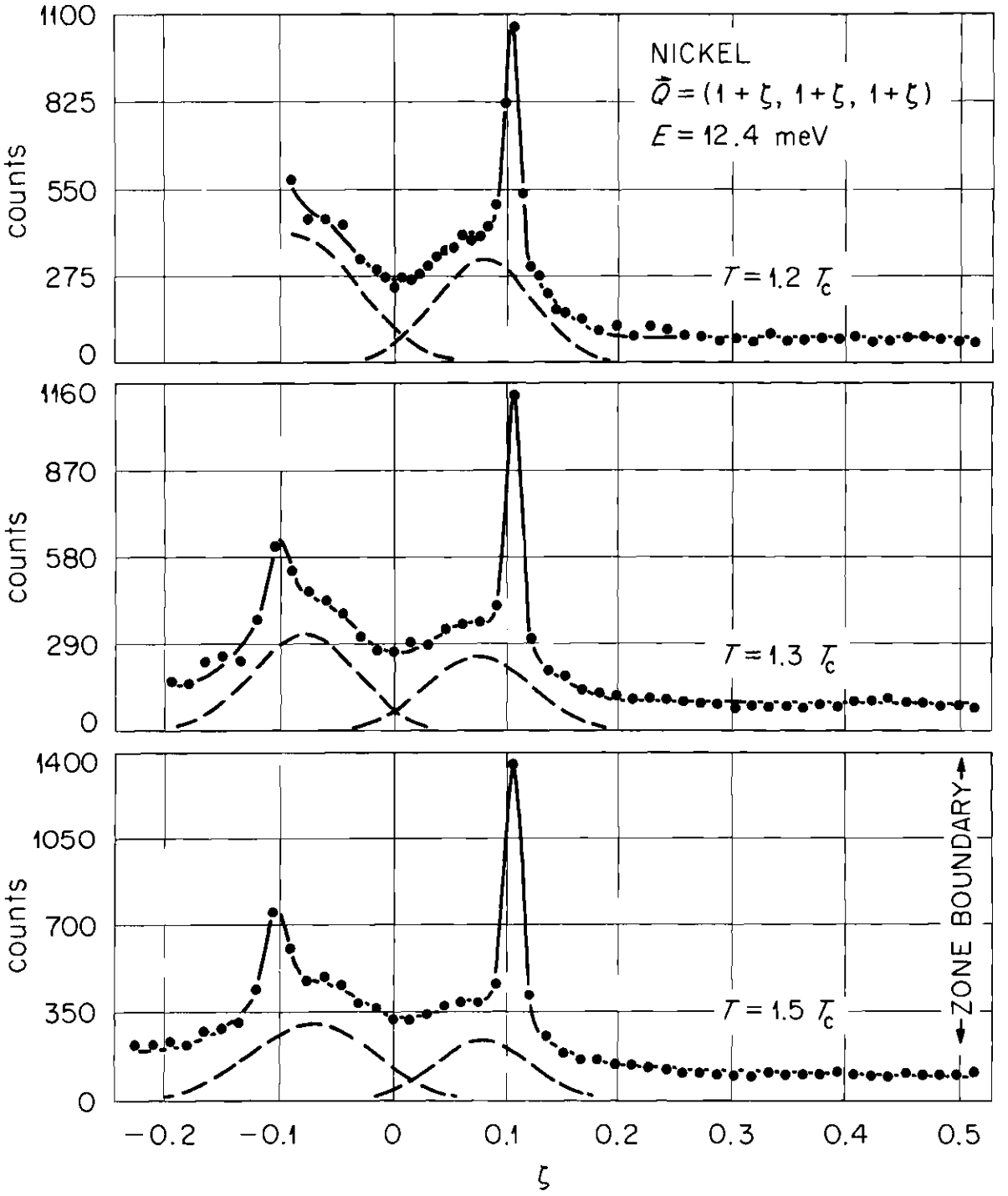

Figure 26. Measured Scattering Above T_C at ±q Around the (111) Reciprocal Lattice Point. The Solid Curves are the Computer Least-Squares Fits.

considerably less than that at +q. This is due to the fact that the cross section for phonon* scattering is proportional to $|\vec{Q}\cdot\hat{e}|^2$, where $\hat{e}$ is the (unit) polarization vector of the phonon. For this scan, $\vec{q}\,||\,\vec{Q}$, so that only the longitudinal phonon is visible. The integrated intensities of the phonons at ±q are related by the factor $|\vec{\tau}\pm\vec{q}|^2$. The spin wave intensities at ±q differ through the variation of the magnetic form factor $F(\vec{Q})$ and the Debye-Waller factor $e^{-2W(\vec{Q})}$, so that the intensity of the magnon at −q is somewhat greater than the one at +q.

The solid curve in the figure is the computer least-squares fit. The positions, widths and intensities for ±q obtained from these fits agree with each other once the appropriate variables in the cross sections and the resolution of the spectrometer are properly taken into account. Note that as in the case of iron, there is no indication of any interaction of the magnons and phonons.

In comparing the experimental measurements on Fe(Si) and Ni, it should be noted that in general the measurements on nickel were more difficult to carry out for several reasons. First, the Fe(Si) sample was somewhat larger, and the magnetic moment is about four times larger, so that the magnetic scattering was considerably stronger from the Fe(Si) sample. The spin wave dispersion relations are also steeper in nickel, so that the spin wave scattering in a constant energy transfer scan is reduced (see equation 43 and Figure 11). In addition, because

---

*Recall that the polarization vector of the phonon describes the displacement of the atoms from their equilibrium positions in relation to the wavevector $\vec{q}$ of the phonon. For a longitudinal phonon, $\vec{q}\,||\,\hat{e}$, and for a transverse phonon, $\vec{q}\perp\hat{e}$.

of the steepness of the dispersion surface, the spin waves at ±q begin to overlap at the higher temperatures, so that they must both be measured in order to separate the contributions from one another. This effectively doubles the experimental running time. The resolution of the spectrometer also becomes more important. For example, if magnetic scattering is observed at $\vec{q} = 0$, then the contributions are coming from the dispersion surface in all directions of $\vec{q}$, and not just the $\pm\vec{q}$ pertaining to the particular scan being carried out. The lower the energy of the spin waves being measured, the closer they are in $\vec{q}$, and hence the more serious is this problem. Considerably better resolution had to be employed for the lower energy measurements in nickel compared with iron. Improving the resolution reduces the observed scattering intensity, and hence increases the experimental running time. Note that for iron the spin waves did not overlap appreciably even at 8.27 meV (see Figure 18).

Figure 27 shows several scans at and above T_C for 12.41 meV with the phonons removed so that the magnetic contribution to the scattering can be seen in more detail. The scans in Figures 26 and 27 have been extended to the zone boundary, and it is evident that there is no appreciable magnetic scattering other than the spin wave scattering. Scans of this type have been carried out from room temperature up to 2 T_C, and from 4 meV to 29 meV. No scattering was observed other than the scattering due to the magnons and phonons.

Several scans at 12.41 meV around the (111) reciprocal lattice point are shown in Figure 28 for temperatures up to 2 T_C. The magnetic

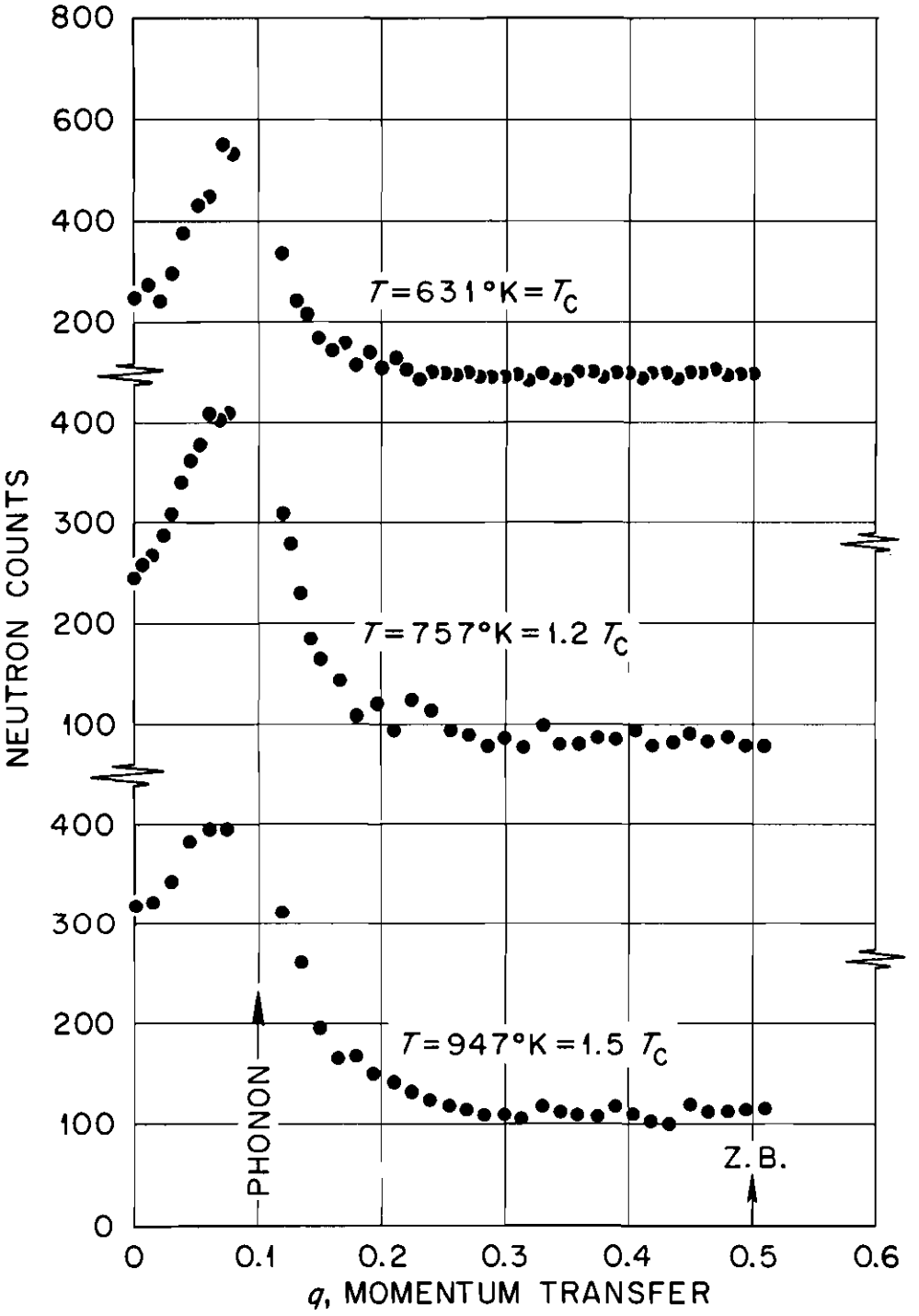

Figure 27. High Resolution Scans at 12.41 meV Over the Entire Brillouin Zone at and Above T_C

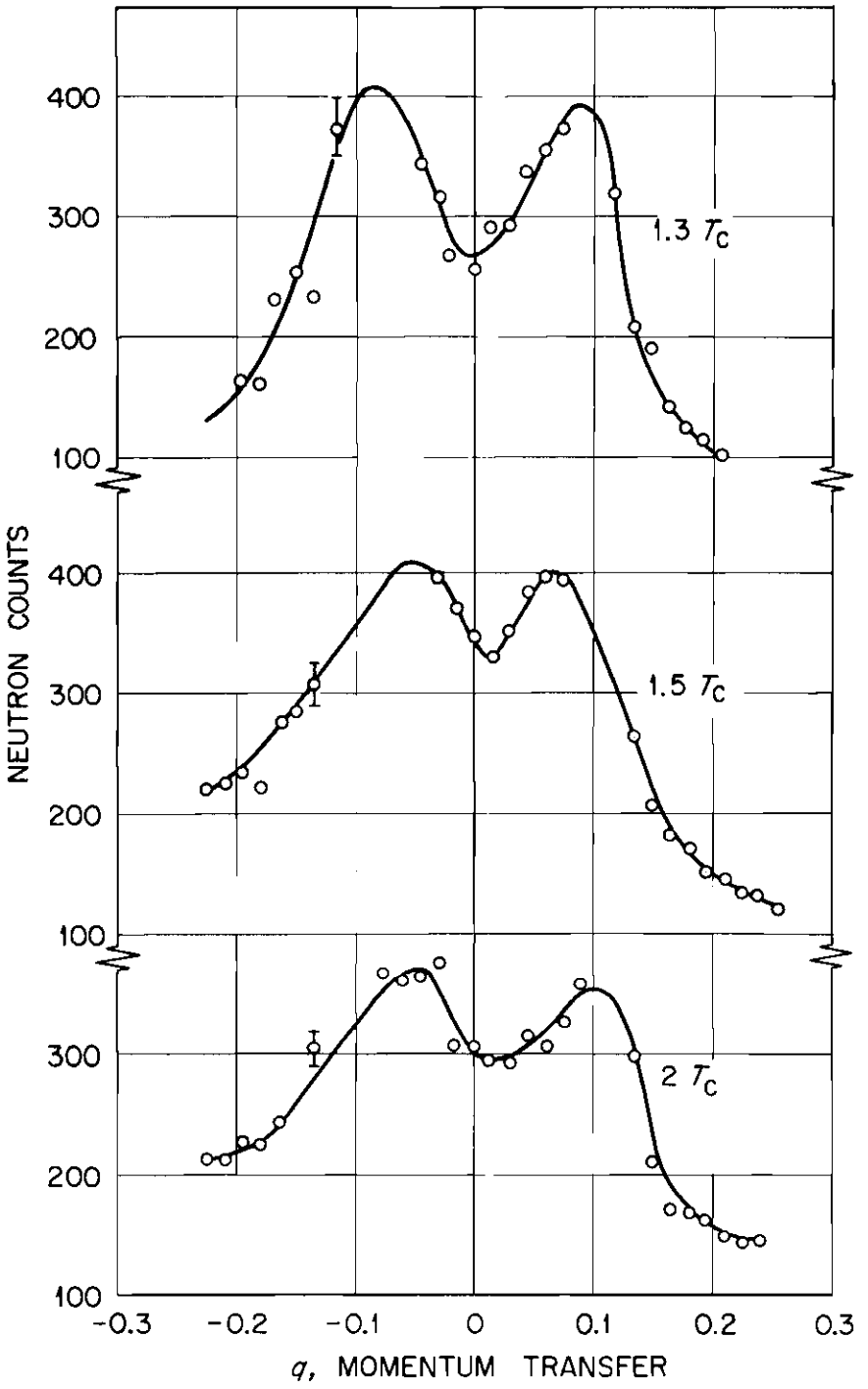

Figure 28. Spin Waves at ±q for $\hbar\omega$ = 12.41 meV for Temperatures up to 2.0 T_C

scattering can be described in terms of two overlapping peaks which do not change position as a function of temperature, but slowly broaden. The peaks at 2 T_C are in fact becoming quite broad, but are still easily discernible.

From these measurements, the linewidths in $\vec{q}$ may be extracted, and Figure 29 shows the observed widths for an energy of 12.41 meV from liquid helium temperature up to 2 T_C. The widths are seen to increase rapidly through the transition temperature and continue to broaden slowly at the higher temperatures. If the energy width is obtained via equation 44, then at T_C, $\Delta E/E \simeq 0.9$. As the linewidth increases, $\Delta E/E$ becomes greater than one, so that in this sense the concept of a spin wave becomes ill-defined at this energy. At 2 T_C, $\Delta E/E \sim 1.9$.

Figure 30 shows the linewidths for an energy transfer of 24.8 meV. The general behavior is the same as for 12.41 meV, except that the rate of increase of the linewidth slows just after T_C, instead of continuing to increase fairly rapidly above T_C. (For 12.41 meV, $\Delta E/E > 1$ before the rate of increase slows.) At T_C, $\Delta E/E \simeq 0.8$, and at 2 T_C, $\Delta E/E \simeq 1.2$. Note that at a fixed temperature above T_C, $\Delta E/E$ is smaller for the higher energy, and in general $\Delta E/E$ was found to decrease with increasing energy. The experimental results indicate that above an energy transfer of $\sim$35 meV, $\Delta E/E < 1$ up to the highest temperature measured.

Search for "Mixed Modes" and "Forbidden Phonons" in Nickel

Recently, Frikkee[90] has made neutron scattering measurements on nickel at room temperature, and observed some rather anomalous

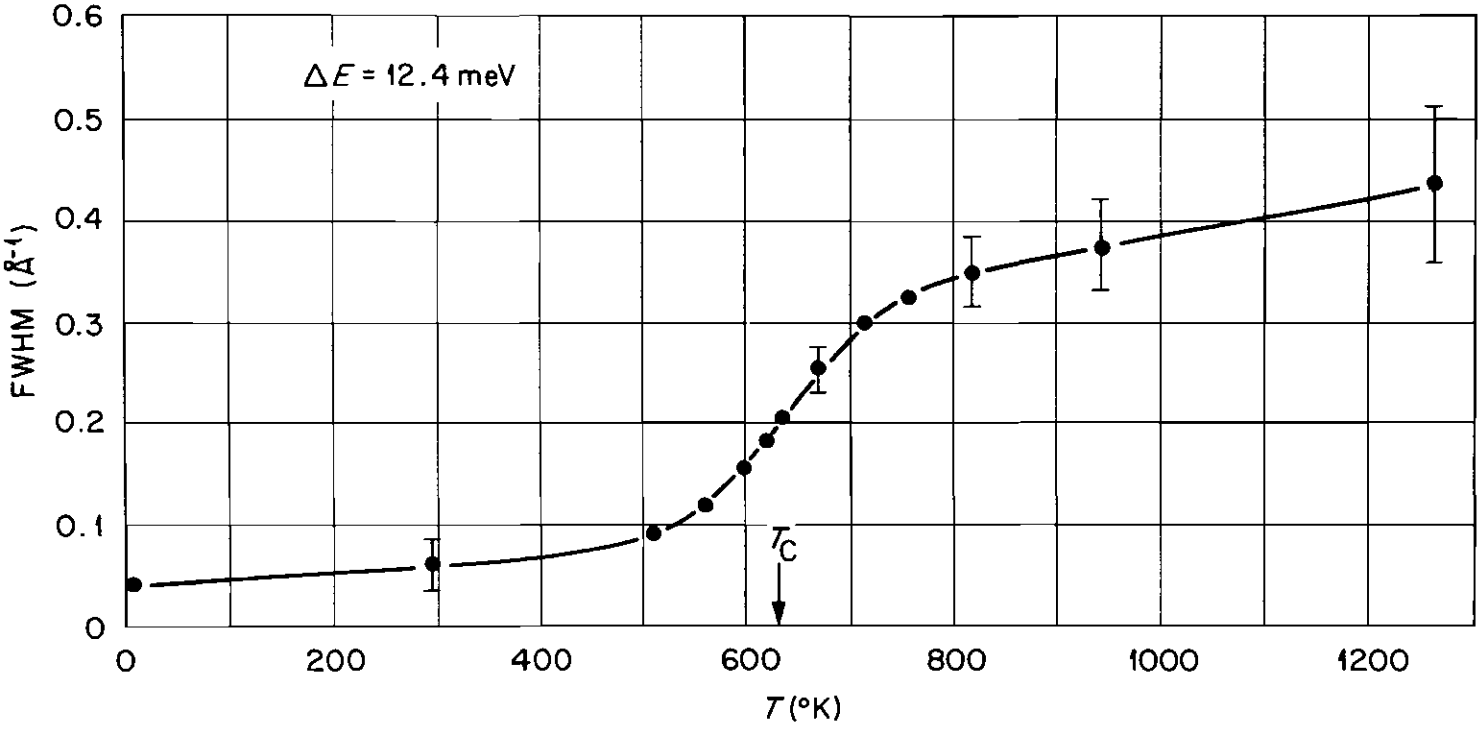

Figure 29. Spin Wave Linewidths as a Function of Temperature for 12.41 meV

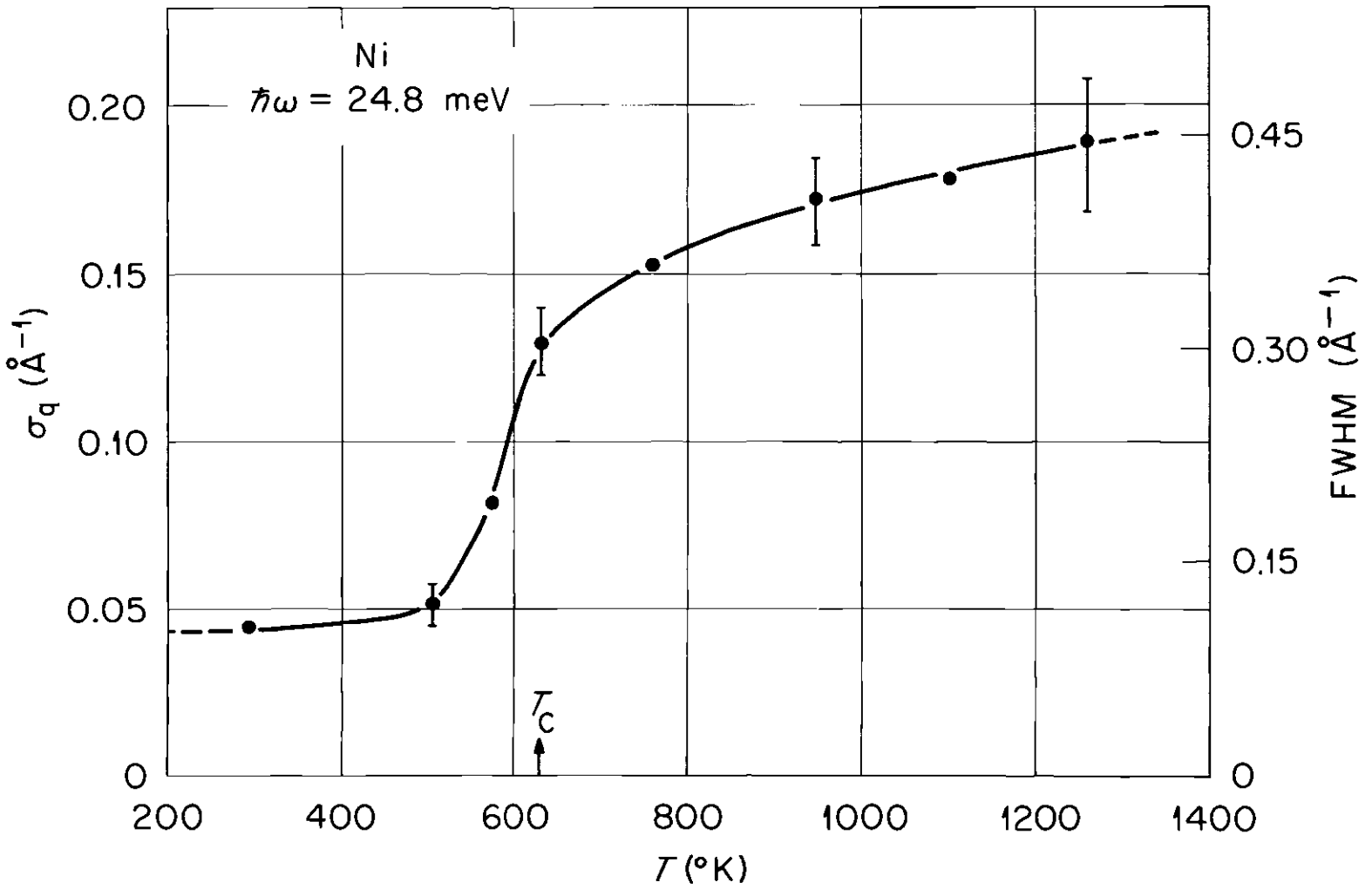

Figure 30. Spin Wave Linewidths Versus T for 24.8 meV. σ_q is the Standard Deviation of a gaussian distribution.

scattering. In scattering configurations where only longitudinal phonons should be observable, he was able to observe transverse phonons. Some of these were due to the poor resolution employed, but others could not be explained on this basis, and his conclusion was that there is an additional interaction present which lowers the symmetry of the crystal from cubic symmetry. The polarization vectors of the phonons would then not be purely longitudinal or transverse, and hence the transverse phonons might be observable in a longitudinal scan. Apparently, however, the observed frequencies of these perturbed transverse phonons depend on whether they are observed in the usual scattering configuration for measuring transverse phonons or in the "forbidden" configuration. The observed frequencies in the forbidden geometry were consistently different ($\sim$10%). Furthermore, the frequency of the phonons also deviated markedly when measured in neutron energy gain rather than neutron energy loss, and the observed intensities did not obey the detailed balance condition, which relates the scattering cross sections for energy gain and energy loss.

In addition to the polarization changes of the phonons, a new elementary excitation was observed. This excitation has very little dispersion over the entire Brillouin zone, and interacts strongly with both the magnons and phonons. It was therefore concluded that this mode has both electronic and vibrational character, and hence was called a "mixed mode." The scattering from this mode was very unusual in that the observed frequency depended markedly on the manner in which it was observed. The frequency of the mode differed up to 25% from neutron

energy gain measurements to neutron energy loss measurements. Moreover, the scattering in the neutron energy gain configuration was very weak, if observable at all, so that the detailed balance condition was again violated. It was concluded that this discrepancy was due to the "recoil energy of the atom." Thus two dispersion curves had to be drawn, one for energy gain and one for energy loss. Frikkee also carried out measurements in a magnetic field, and found that the scattering intensity depended on the orientation of the magnetic field.

Inconsistent and anomalous results such as these are highly suspicious. In order to check if there was any scattering of the type observed by Frikkee, several experiments were performed at room temperature both on a "natural" single crystal of nickel, and the ^{60}Ni crystal. The nickel crystal with the natural distribution of isotopes was used in order to compare with Frikkee's data, which were all taken on a natural single crystal. Figure 31 shows two longitudinal scans in the [001] direction on the natural single crystal. The scan with the coarse resolution is essentially identical to that observed by Frikkee, with both the longitudinal (LA) and transverse (TA) phonons visible. Note that the peak at $\nu = 0$ goes up to 18,521 counts, which is more than an order of magnitude larger than the longitudinal phonon. This peak at $\nu = 0$ is due to the large incoherent scattering cross section present in the natural nickel, and is completely absent in the ^{60}Ni crystal. Note also that there is no evidence of the mixed mode, which should appear at about 5.0 THz (1 THz = 4.135 meV) in neutron energy loss. The scan with the improved resolution shows the transverse phonon can be

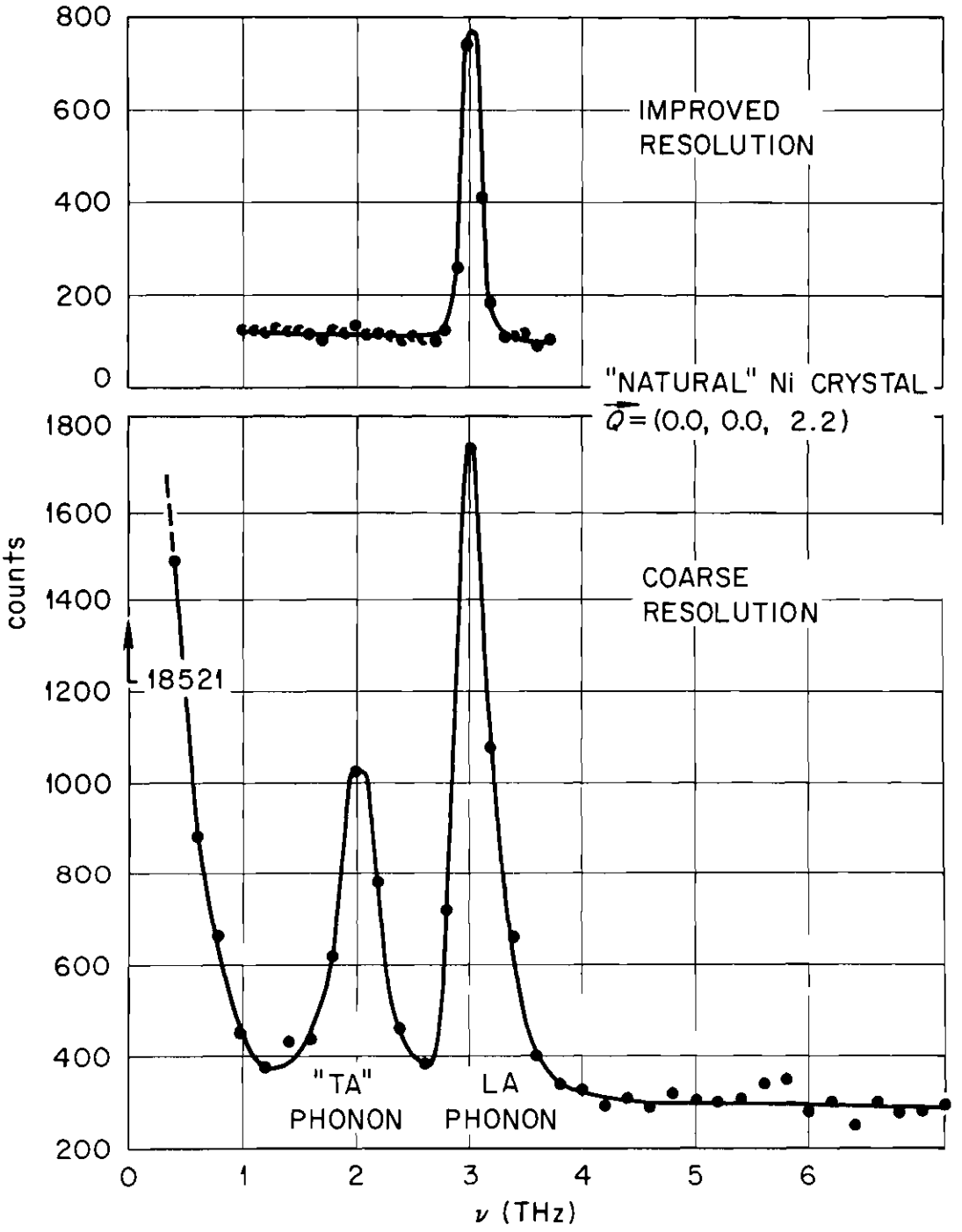

Figure 31. Comparison of Longitudinal Scans with Coarse Resolution and Good Resolution

completely eliminated when better resolution is employed.

Two scans along the zone boundary in the [111] direction are compared in Figure 32. The scan on the natural crystal indeed shows some additional scattering similar to that observed by Frikkee, and an approximate "decomposition" into two peaks, according to Frikkee, is shown. However, the detailed agreement between this scan and Frikkee's results is not very good. Most importantly, however, the scan on the ^{60}Ni crystal shows no evidence whatsoever of either the "mixed mode" or the "transverse" phonon. Note that the signal to noise ratio of the LA phonon is considerably better ($\sim$2.5 times better) for the ^{60}Ni, even though the coherent phonon scattering cross section is reduced by a factor of 13.3 (see Chapter III). Although the experimental running time for the scan on the ^{60}Ni was much longer, the background is less, and this reduction is due to the absence of the incoherent scattering. The elimination of this large background scattering is one of the principal advantages of using the ^{60}Ni for studies of the magnetic scattering.

If the mixed mode was really present, then it should be much more clearly visible in the ^{60}Ni scan. For example, if the cross section was proportional to $|b|^2$, as suggested by Frikkee, then the peak to background ratio should be more than twice as good. If the mixed mode had some magnetic character, for instance* $\sigma \sim$ pb, then the ratio

---

*p is the magnetic scattering amplitude, analogous to b in the nuclear case.

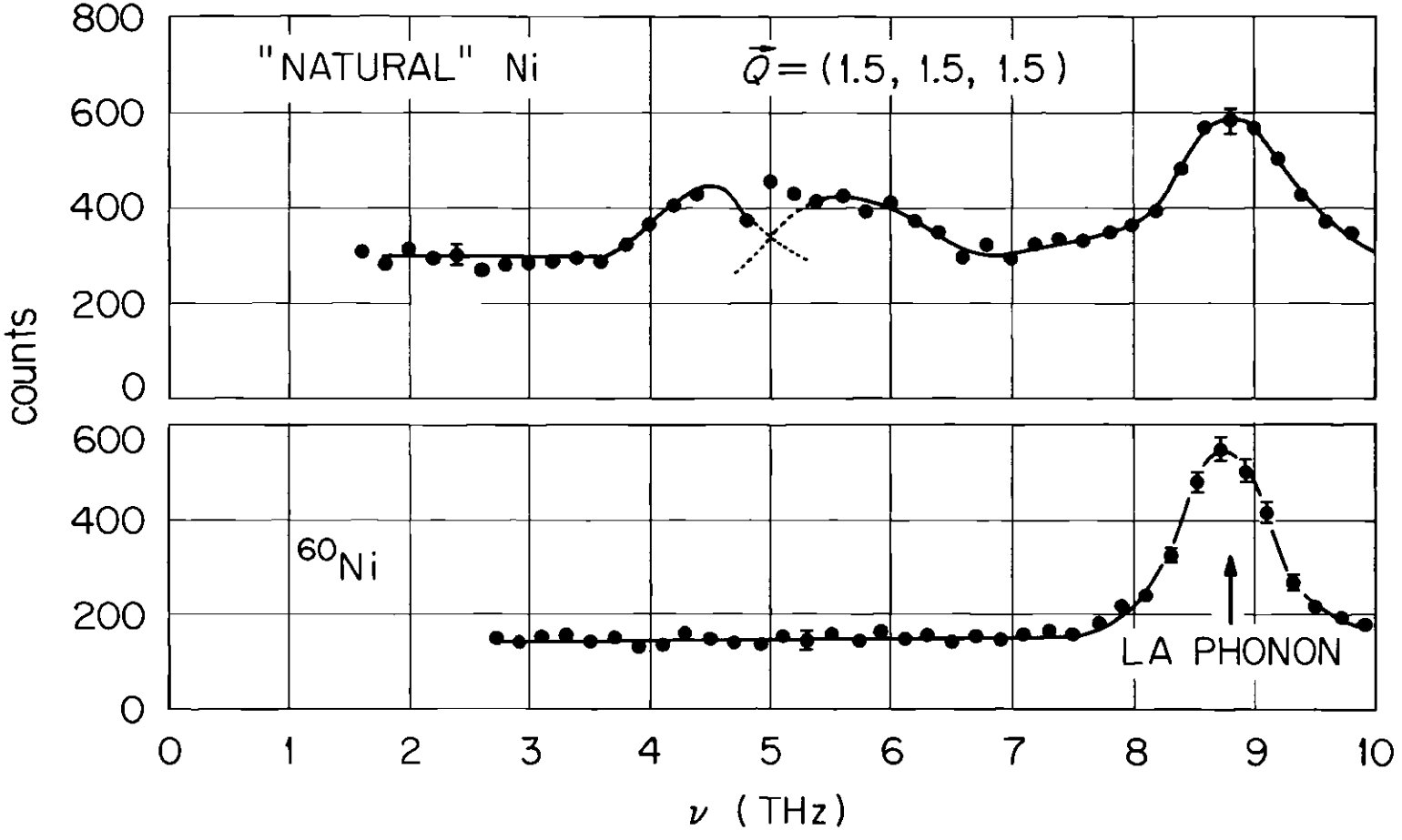

Figure 32. Longitudinal Scan at the Zone Boundary in a "Natural" Crystal of Nickel and a ^{60}Ni Crystal, Showing the Absence of the "Mixed Mode" and the "Forbidden" Phonon in the ^{60}Ni Crystal

should be ∿10 times larger. If the mixed mode was purely magnetic scattering, the observed peak should be ∿25 times larger.

With the large incoherent scattering present, one can expect additional scattering processes to occur. One such process is incoherent phonon scattering, in which the intensity is proportional to the phonon density of states. A peak in the one phonon density of states occurs in the 4 to 6 THz range,[92] and thus one might expect some scattering in this frequency range. This seems to be the most likely explanation of the additional scattering observed in Figure 32. Recall that since the incoherent phonon scattering is proportional to the density of phonon states, the energy dependence of the scattering will be independent of $\vec{Q}$. Hence if a peak occurs due to this process, the scattering will show no "dispersion."

The magnetic anisotropy of nickel is small, the spin wave dispersion relations are isotropic in $\vec{q}$, and the magnon-phonon coupling is negligibly small. These observations seem to be at variance with Frikkee's conclusion that the electron-nuclear systems are strongly enough coupled to give rise to new elementary excitations in the system, as well as to strongly perturb the phonons and magnons. In all the measurements that have been taken, no evidence has been found for the existence of either "mixed modes" (either by direct observation or through perturbations of the magnons or phonons), or of changes in the polarization vectors of the phonons from that required by cubic symmetry. It is therefore apparent that the scattering observed by Frikkee arises

from the already well-understood sources of scattering from the electrons and nuclei.

Discussion of Results

The neutron scattering results at low temperatures are best described by calculations of the generalized susceptibility based on band structures in which the electron correlations are treated as accurately as possible. For nickel, the most ambitious calculations to date are those of Cooke and Davis.[71] Their theory includes a momentum dependent spin splitting of the electronic energy bands as well as multi-band effects. From these calculations both the spin wave mode and its intersection with the Stoner continuum can be calculated. Their results are in excellent agreement with the energies of the spin wave modes, and correctly show that the Stoner states extend lowest in energy in the [111] direction and are highest in the [100] direction. The positions of the intersection points, though, occur at too high an energy. However, it is extremely difficult to take account of the electron correlations and numerically calculate the cross section with sufficient accuracy to give quantitative agreement, particularly when it is recalled that the band energies are of the order of rydbergs, whereas the spin wave energies are of the order of meV (1 meV = 0.000074 Ry). Nevertheless, the overall agreement between theory and experiment gives us confidence that the description of the excitation spectrum obtained from calculations of $\chi(\vec{q},\omega)$ based on band structures is at least qualitatively correct, and that the agreement will improve as the electron correlations are treated to better approximation. Similar calculations

of the dynamic susceptibility for iron should be forthcoming soon.

Temperature dependent calculations of $\chi(\vec{q},\omega)$ are much more difficult to do. Generally the low temperature theory is used, with the band splitting set proportional to the magnetization. The only temperature dependent calculations available are those of Lowde and Windsor[66] for nickel, which are based on the random-phase-approximation (RPA) for the susceptibility, and employ a rigid spin splitting of the energy bands which is proportional to the magnetization. Their calculations do correctly show that away from the immediate vicinity of the critical region the susceptibility evolves smoothly through T_C. But the detailed agreement between their calculations and these experimental results is poor. Above T_C the calculations show only a very diffuse "hump" in the scattering which is spread over the entire Brillouin zone, rather than a fairly well defined spin wave mode. At low temperatures the Stoner cutoff occurs at much too high an energy, and above T_C there is no cutoff at all, since there are no well-defined spin waves.

It is not really too surprising that this theory, which is based on a molecular field approximation to the band structure, does not give the correct spin dynamics above T_C. Certainly at these relatively low temperatures there is not enough thermal energy to break down the strong intra-atomic coupling of the electrons, which gives rise, for example, to the paramagnetic moments. Clearly, in order to bring theory into agreement with experiment, the electron correlations at elevated temperatures will need to be incorporated into the theory in a more realistic manner. It is encouraging to see that more theoretical work is ongoing.[93]

In comparing theory with experiment, one must keep in mind that as the temperature increases form T = 0, the χ^{zz} and χ^{+-} contributions to the scattering grow, and in fact above T_C all three components of the susceptibility are equal for an isotropic ferromagnet. Since there are propagating modes above T_C, there must be a propagating component of χ^{zz} as well as $\chi^{\pm\mp}$. As the susceptibility evolves from low temperatures, where the χ^{-+} part of the susceptibility dominates the scattering, the χ^{zz} part of the propagating mode must grow continuously into the spin wave mode. Just below T_C, on the other hand, the scattering is usually divided into scattering which is predominantely spin wave scattering ($\chi^{\pm\mp}$), and scattering which is predominately diffusive in nature (χ^{zz}). This diffusive scattering was expected to show up as a peak centered at $\omega = 0$, and this was clearly demonstrated experimentally[94] for $RbMnF_3$, which is an ideal Heisenberg antiferromagnet. For iron[60,64] and nickel,[64] however, no central mode was observed. This may be due to the long range spin correlations which persist in these ferromagnets. The fluctuations in χ^{zz} occur over a large spatial region, which means a small region in $\vec{q}$. This region is apparently too small for a central mode to be clearly discernible.

These short range spin correlations may also affect photoemission measurements. If many-body effects are indeed crucial to the interpretation of these types of experiments (see Chapter I), then the persistence of long range spin correlations will considerably modify the changes expected when comparing the energy distributions above and below T_C.

Spin waves have been observed above T_N in a number of antiferromagnetic materials,[94-100] many of which are highly anisotropic and therefore have magnetic properties of a lower dimensionality (one and two dimensional systems). Experiments on other ferromagnets, however, (for example, EuO[101] and Gd[102]) do not indicate the presence of either central modes below T_C, or propagating modes* above T_C. In particular, the behavior of EuO, which is considered to be an ideal Heisenberg ferromagnet, is considerably different from $RbMnF_3$. Perhaps the spin waves above T_C in iron and nickel could be explained in terms of a Heisenberg ferromagnet if the exchange interaction were extended to more distant neighbors. It would seem to be physically more appealing, though, to discuss such a long range exchange interaction in terms of the itineracy of the magnetic electrons. At any rate, it is clear that the Heisenberg model by itself cannot reproduce the sharp fall off of the spin wave intensity at any temperature.

Short wavelength excitations exist above the temperature at which long range order occurs in other systems also. For example, short wavelength phonons have been observed[104] in Rb just above the melting point. In liquids, however, the long wavelength phonons are well defined. Physically this is because there is a macroscopic field (the density) in which the excitations can propagate (i.e., $\lim_{t\to\infty} < \rho(\vec{r}',t)\ \rho(\vec{r},0) > = \text{constant}$). In the magnetic case, on the other hand, the field (the magnetization) in which the spin waves propagate vanishes

---

*This is also true of other heavy rare-earth metals.[103]

(i.e., $\lim_{t\to\infty} < \hat{S}(\vec{r}',t)\ \hat{S}(\vec{r},0) > \equiv 0$) above the ordering temperature. Thus there cannot be any long wavelength spin waves above T_C. The short wavelength spin waves exist in the fluctuations of the magnetization.

Finally, a few words are in order concerning the fall off of the spin wave intensity at high energies. This fall off is certainly no artifact of the spectrometer, since the spin wave intensities fall off at different energies in different symmetry directions of a crystal, and at considerably different energies in different samples. In particular, the spin wave fall off occurs at about 85 meV in the [111] direction in nickel, and at 115 meV in the [110] direction of Fe(12% Si), which is a difference of 30 meV. This is quite a large energy range, particularly when it is recalled that the entire spin wave spectra of most magnetic materials that have been studied by neutron scattering techniques do not span 30 meV.

The fall off of intensity has been interpreted in terms of the intersection of the spin wave modes with the Stoner continuum of excitations, and this certainly seems to be the most likely explanation. It is not the only one, however, and in view of the unusual temperature dependence of the cutoff, perhaps other alternatives should be examined more closely. For example, in the itinerant electron model there can also be optical spin wave modes. One of these might interact strongly with the acoustical mode, and under the right conditions this could essentially damp out the spin wave scattering.

Stearns[105] has suggested that the magnetism in the 3d metals arises from the indirect exchange coupling of a relatively few ($\sim$5%)

itinerant-d electrons to the (∿95%) localized-d electrons.* In this model the dominant spin-flip excitations which damp the spin waves are from the spin-up to spin-down spherelike itinerant-d Fermi surfaces centered at Γ, so that it is the difference in the wavevectors of these two (spin-split) spheres which determines where the cutoff occurs. As the temperature increases, however, the spin wave cutoffs are found to increase in $\vec{q}$ (see Figures 13 and 23), which would mean that the splitting between the itinerant electrons would increase with increasing temperature. This seems to be in the wrong direction.

*This model is similar to the Zener model. See ref. 92, and references therein.

Chapter V

CONCLUSIONS AND RECOMMENDATIONS

The neutron inelastic scattering technique has been used to study the temperature dependence of the magnetic excitations in iron and nickel from low temperatures to well above the ferromagnetic transition temperatures. Previous measurements in the small wavevector region have shown that the spin wave dispersion relations renormalize to zero as $T \rightarrow T_C$, with the spin waves becoming overcritically damped just below T_C. In contrast to this behavior, the spin waves at larger values of $\vec{q}$ are found to be only moderately renormalized up to T_C, and persist as well defined excitations up to the highest temperatures measured (1.4 T_C for iron and 2.0 T_C for nickel). No further renormalization is observed above T_C.

The spin wave intensities have been measured for Fe(Si) along the [110] direction. At room temperature the intensity decreases slowly with increasing energy until $\sim$100 meV, and then begins to rapidly decrease. The cause of this rapid decrease is interpreted in terms of the band model of ferromagnetism as the intersection of the spin wave spectrum with the Stoner continuum of spin-flip excitations. It was expected that with increasing temperature the Stoner continuum would lower in energy, but measurements up to 1.4 T_C show that within experimental error there is no change in the spin wave intensity cutoff.

These results are in disagreement with present theoretical estimates of the generalized susceptibility at elevated temperatures.

In addition to the spin wave energies and intensities, the linewidths in iron were also measured. With increasing temperature, the widths of the excitations rapidly increase up to T_C, but above T_C no further broadening occurs. For $E \gtrsim 8$ meV the ratios of the energy widths above T_C to the excitation energies were found to be less than one ($\Delta E/E < 1$), which has been used as a criterion for the definition of a spin wave excitation. The dynamic correlation range corresponds to a sphere with a diameter of $\sim$10 Å, and this correlation range is independent of temperature over the temperature range covered above T_C. With decreasing energy the scattering evolves smoothly into the critical scattering around the origin ($\vec{q} = 0$), and with increasing energy $\Delta E/E$ decreases. At energies just below the cutoff in intensity, $\Delta E/E \sim 0.33$.

The behavior of the spin wave intensities in nickel is similar to that in iron. The spin wave intensities in the [111] direction were measured at a series of temperatures, and the rapid decrease in the spin wave intensity at $\sim$85 meV was independent of temperature up to at least 1.2 T_C (the highest temperature that the high energy measurements were taken). Also the overall spin wave intensities for both iron and nickel were reduced at high temperatures.

The spin wave linewidths in nickel increase rapidly up to T_C and then continue to broaden slowly above T_C, in contrast to the behavior observed in iron. At 2.0 T_C, $\Delta E/E < 1$ for $E > \sim$35 meV. The spin wave

energies, as well as the linewidths, were found to be isotropic in $\vec{q}$ over the entire temperature range covered for both iron and nickel.

In addition to these temperature dependent measurements, a search was made for the "mixed modes" and "forbidden phonons" recently reported for nickel by Frikkee. His results indicated that there was a strong electronic-vibrational coupling. To compare with Frikkee's results, measurements were taken on a nickel crystal with the natural distribution of isotopes. The results showed scattering similar to that observed by Frikkee, but this scattering was completely absent in identical scans taken on the ^{60}Ni crystal. This suggests that the scattering is probably due to the large incoherent scattering found in the "natural" nickel, and in any case is certainly not due to any new phenomena. Furthermore, the temperature dependent results on both nickel and iron, as well as polarized beam experiments by other authors, show that the magnon-phonon coupling is negligible.

The overall agreement between the neutron scattering results for nickel at low temperatures and the calculations of the generalized susceptibility based on band structures gives us confidence that the picture of the excitation spectrum based on band structures is at least qualitatively correct and that quantitative agreement can be obtained by treating the electron interactions to better approximation. The electron correlations in iron are more difficult to deal with than for nickel. Calculations of the non-interacting susceptibility based on band structures have been performed, and the results indicate that the region of high density of Stoner states occurs at too high an energy

and increases too slowly with energy to explain the low temperature neutron scattering results for iron. Certainly more theoretical work is needed on this problem. The theory may need to be extended beyond the generalized Random Phase Approximation (RPA), and in any case the electron correlations need to be treated to better approximation.

Calculations of the generalized susceptibility at elevated temperatures are much more difficult to do accurately. One of the major problems with the theory stems from the use of the RPA, in which one sets the band splitting proportional to the magnetization. The only temperature dependent calculations available are the RPA calculations of Lowde and Windsor for nickel, which do seem to correctly show that the scattering outside the immediate vicinity of the critical region evolves smoothly through T_C. But the detailed agreement between these calculations and the experimental results is poor. The theory will have to be extended beyond the RPA, since in any molecular field theory the renormalization of the dispersion relations with temperature is independent of $\vec{q}$. Thus the long wavelength and short wavelength excitations renormalize in the same way, which is contrary to experiment. The electron correlations at elevated temperatures will need to be incorporated into the theory more accurately in order to produce the strong short range spin correlations necessary to support propagating modes above the ferromagnetic transition temperature. Clearly more theoretical effort will be needed in order to bring theory into agreement with experiment.

APPENDIX A

HIGH TEMPERATURE FURNACE

In order to carry out the measurements on iron and extend the measurements on nickel to higher temperatures, a high temperature vacuum furnace was constructed. The furnace was designed to fit on a six inch radius goniometer which in turn could be mounted on any of the neutron spectrometers at the High Flux Isotope Reactor. The blueprint drawings for the furnace are shown in Figures 33 and 34.

The heater element was made from tantalum foil curled in the shape of a cylinder, slit down the sides, and then welded at the top. The current to heat the element flows up one side and down the other, and the sample is then heated by radiation. Thermocouples were spot-welded to the sample to measure and control the temperature. The stability of the thermocouple readings was better than 1/2°K over a period of 48 hours.

The temperature gradients in the samples and heat losses to the outside container were minimized by surrounding the samples by six tantalum foil heat shields. The temperatures measured across the surfaces of the samples differed less than two degrees at 1000°C. The base of the furnace and the electrodes which attach to the heater element are water cooled. The heater was designed to have a small resistance, so that the power is supplied by a high current-low voltage arrangement.

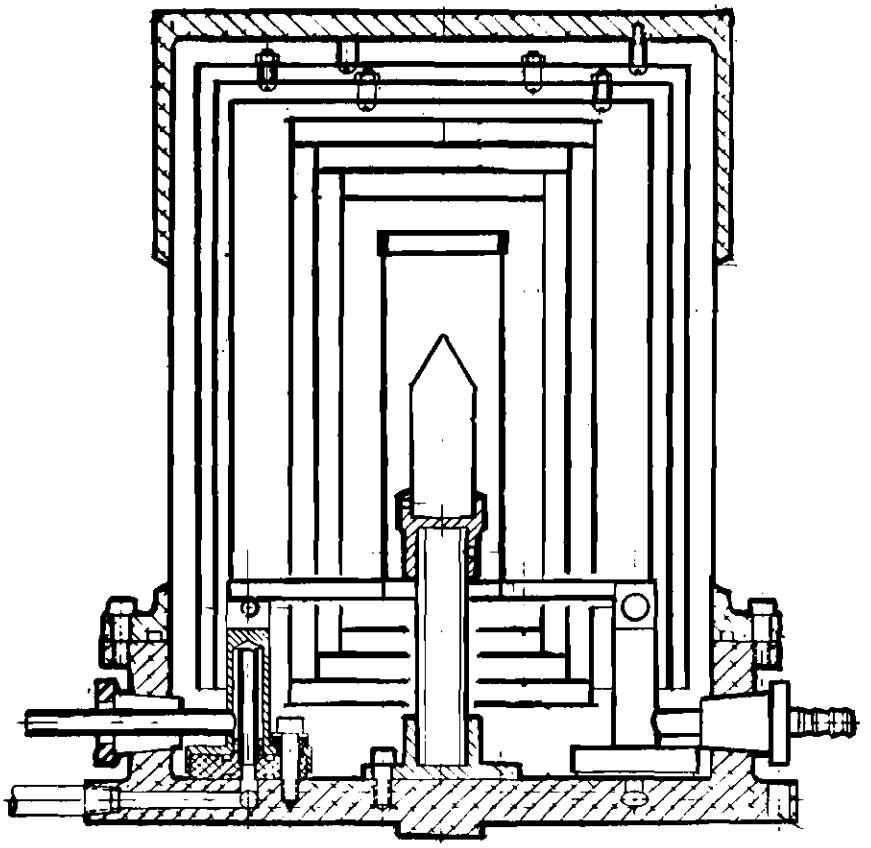

Figure 33. Furnace Drawing--Side View

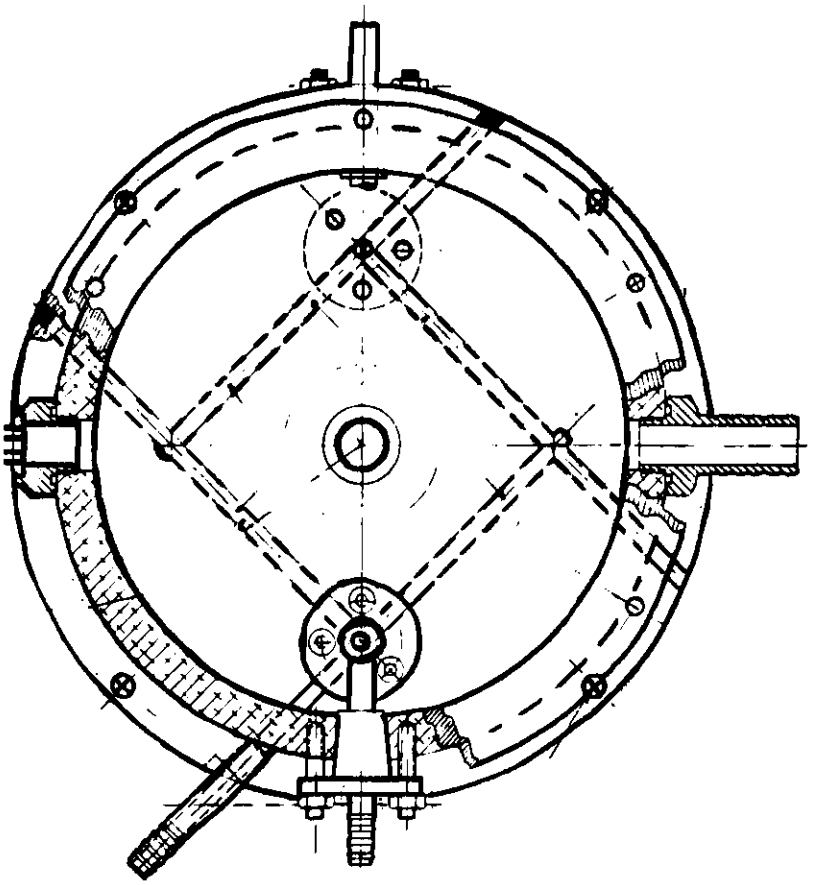

Figure 34. Furnace Drawing--Top View

The design is similar to that of an arc-welder, and very little current leaks through the cooling water. For the currents needed to achieve the highest temperatures, the magnetic field at the center of the sample was less than 10 Oe.

The outside container is made of aluminum, and the walls where the beam passes through were thinned to 0.05 inches. A diffusion pump was used to pump out the furnace and pressures of $\sim 5 \cdot 10^{-5}$ mm were attained. This pressure was more than adequate to prevent contamination of the surfaces of the samples.

BIBLIOGRAPHY

1. A thorough discussion of the experimental and theoretical considerations pertaining to these viewpoints as well as extensive references to the literature are given in the review by C. Herring, in Magnetism, ed. by G. T. Rado and H. Suhl (Academic, New York, 1967), Vol. 4.

2. C. G. Shull and Y. Yamada, J. Phys. Soc. Japan 17, Suppl. B III, 1 (1962); C. G. Shull, in "Electronic Structure and Alloy Chemistry of the Transition Elements," ed. by P. A. Beck (Wiley, New York, 1963), p. 69; C. G. Shull and H. A. Mook, Phys. Rev. Lett. 16, 184 (1966).

3. H. A. Mook, Phys. Rev. 148, 495 (1966).

4. R. M. Moon, Phys. Rev. 136, A195 (1964).

5. R. C. Maglic, AIP Conference Proceedings No. 5, 1420 (1971).

6. G. Caglioti, M. J. Cooper and V. J. Minkiewicz, J. Appl. Phys. 38, 1245 (1967).

7. F. Menzinger and A. Paoletti, Phys. Rev. Lett. 10, 290 (1963).

8. A review is given by G. Shirane, V. J. Minkiewicz and R. Nathans, J. Appl. Phys. 39, 383 (1968).

9. D. R. Baraff, Phys. Rev. B 8, 3439 (1973).

10. A. V. Gold, L. Hodges, P. T. Panouis and D. R. Stone, Int. J. Mag. 2, 357 (1971).

11. P. Goy and C. C. Grimes, Phys. Rev. B 7, 299 (1973).

12. D. C. Tsui, Phys. Rev. 164, 669 (1967).

13. L. Hodges, D. R. Stone and A. V. Gold, Phys. Rev. Lett. 19, 655 (1967).

14. D. C. Tsui and R. W. Stark, Phys. Rev. Lett. 17, 871 (1966).

15. A. S. Joseph and A. C. Thorsen, Phys. Rev. Lett. 11, 554 (1963).

16. J. Hubbard, Proc. Roy. Soc. A 276, 238 (1963).

17. E. P. Wohlfarth, Phys. Lett. 3, 17 (1962).

18. S. Foner, A. J. Freeman, N. A. Blum, R. B. Frenkel, E. J. McNiff, Jr., and H. C. Praddaude, Phys. Rev. 181, 863 (1969) and references therein.

19. G. Busch, M. Campagna and H. C. Siegmann, Phys. Rev. B 4, 746 (1971); U. Bänninger, G. Busch, M. Campagna and H. C. Siegmann, Phys. Rev. Lett. 25, 585 (1970); H. Alder, M. Campagna and H. C. Siegmann, Phys. Rev. B 8, 2075 (1973).

20. W. Gleich, G. Regenfus and R. Sizmann, Phys. Rev. Lett. 27, 1066 (1971).

21. P. M. Tedrow and R. Meservey, Phys. Rev. B 7, 318 (1973).

22. J. A. Hertz and K. Aoi, Phys. Rev. B 8, 3252 (1973).

23. B. A. Politzer and P. H. Cutler, Phys. Rev. Lett. 28, 1330 (1972).

24. N. V. Smith and M. M. Traum, Phys. Rev. Lett. 27, 1388 (1971).

25. P. W. Anderson, Philos. Mag. 24, 203 (1971); W. Baltensperger, Helv. Phys. Acta 45, 203 (1973); S. Doniach, AIP Conference Proc. No. 5, 549 (1972).

26. C. S. Fadley and D. A. Shirley, Phys. Rev. Lett. 21, 980 (1968).

27. A. J. McAlister, J. R. Cuthill, R. C. Dobbyn and M. L. Williams, Phys. Rev. Lett. 29, 179 (1972).

28. J. E. Rowe and J. C. Tracy, Phys. Rev. Lett. 27, 799 (1971).

29. D. T. Pierce and W. E. Spicer, Phys. Rev. B 6, 1787 (1972).

30. W. Marshall and S. W. Lovesey, Theory of Thermal Neutron Scattering (Oxford Press, London, 1971).

31. T. Izuyama, Phys. Rev. B 5, 190 (1972).

32. At least in cases where antisymmetric exchange vanishes. See R. L. Melcher, Phys. Rev. Lett. 30, 125 (1973).

33. M. K. Wilkinson and C. G. Shull, Phys. Rev. 103, 516 (1956).

34. H. A. Gersch, C. G. Shull and M. K. Wilkinson, Phys. Rev. 103, 525 (1956).

35. R. D. Lowde, Rev. Mod. Phys. 30, 69 (1958).

36. M. Ericson and B. Jacrot, J. Phys. Chem. Solids 13, 235 (1960).

37. G. M. Drabkin, E. I. Zabidarov, Ya. A. Kasman, A. I. Okorokov and V. A. Trunov, JETP 20, 1548 (1964).

38. L. Passell, K. Blinowshi, T. Brun and P. Nielsen, Phys. Rev. 139, A1866 (1965).

39. G. Shirane, R. Nathans, O. Steinsvoll, H. A. Alperin and S. J. Pickart, Phys. Rev. Lett. 15, 146 (1965).

40. J. Konstantinovic, Solid State Commun. 4, 425 (1966).

41. S. Spooner and B. L. Averbach, Phys. Rev. 142, 291 (1966).

42. D. Bally, B. Grabcev, A. M. Lungu, M. Popovici and M. Totia, J. Phys. Chem. Solids 28, 1947 (1967).

43. D. Bally, M. Popovici, M. Totia, B. Grabcev and A. M. Lungu, Phys. Lett. 26A, 396 (1968).

44. J. Gordon, E. Kisdi-Koszó, L. Pál and I. Visi, Neutron Inelastic Scattering, Vol. II (IAEA, Vienna, 1968), p. 55.

45. K. Blinowshi and R. Ciszewshi, Phys. Lett. 28A, 389 (1968).

46. R. Ciszewski and K. Blinowshi, Phys. Lett. 29A, 513 (1969).

47. B. Antonini, F. Menzinger, A. Paoletti and A. Tucciarone, Phys. Rev. 178, 833 (1969).

48. J. Gordon and M. Popovici, Phys. Lett. 32A, 341 (1970).

49. H. Bourdonnay, A. Bousquet, J. P. Cotton, D. Cribier, B. Farnoux, R. Feuillatre, B. Hennion, J. Jacquier, G. Jannink, R. Kahn, D. Mons, J. Mons, G. Parette, G. Pepy, L. Rouleau, J. P. Trotin, M. Moussa and M. Tournarie, Phys. Lett. 31A, 561 (1970).

50. M. Popovici, Phys. Lett. 34A, 319 (1971).

51. E. Gürmen, S. A. Werner and A. Arrott, AIP Conf. Proc. No. 5, Part II, 1340 (1972).

52. M. W. Stringfellow, J. Phys. C 1, 950 (1968).

53. B. Jacrot, J. Konstantinovic, G. Parette and D. Cribier, Inelastic Scattering of Neutrons in Solids and Liquids (IAEA, Vienna, 1963), p. 317.

54. D. Cribier, B. Jacrot, and G. Parette, J. Phys. Soc. Japan Suppl. 17, 67 (1962).

55. G. M. Drabkin, E. I. Zabidarov, Ya. A. Kasman and A. I. Okorokov, JETP Lett. 2, 336 (1965).

56. T. Riste, G. Shirane, H. A. Alperin and S. J. Pickart, J. Appl. Phys. 36, 1076 (1965).

57. A. Furrer, T. Schneider and W. Halg, Sol. State Commun. 4, 99 (1966).

58. S. J. Pickart, H. A. Alperin, V. J. Minikiewicz, R. Nathans, G. Shirane and O. Steinsvoll, Phys. Rev. 156, 623 (1967).

59. G. Maier and N. Stump, Z. Physik 238, 389 (1970).

60. M. F. Collins, V. J. Minkiewicz, R. Nathans, L. Passell and G. Shirane, Phys. Rev. 179, 417 (1969).

61. V. J. Minkiewicz, M. F. Collins, R. Nathans and G. Shirane, Phys. Rev. 182, 624 (1969).

62. B. I. Halperin and P. C. Hohenberg, Phys. Rev. 177, 952 (1969); Phys. Rev. 188, 898 (1969).

63. The Fe measurements were shown to be outside the hydrodynamic region; J. Als-Nielsen, Phys. Rev. Lett. 25, 730 (1970); V. J. Minkiewicz, Int. J. Mag. 1, 149 (1971). A later experiment showed that in the hydrodynamic region Λ varies as predicted by the dynamic scaling theory; R. Kahn and G. Parette, J. de Phys. 32, 523 (1971).

64. Borankay and Collins, Int. J. Mag. 4, 205 (1973).

65. J. W. Cable, R. D. Lowde, C. G. Windsor and A. D. B. Woods, J. Appl. Phys. 38, 1247 (1967); S. Komura, R. D. Lowde and C. G. Windsor, Neutron Inealstic Scattering (IAEA, Vienna, 1968), p. 101.

66. R. D. Lowde and C. G. Windsor, Adv. Phys. 19, 813 (1970), and references therein.

67. H. A. Mook and R. M. Nicklow, Phys. Rev. B 7, 336 (1973); H. A. Mook and R. M. Nicklow, J. de Phys. 32, 1177 (1971).

68. H. A. Mook, R. M. Nicklow, E. D. Thompson and M. K. Wilkinson, J. Appl. Phys. 40, 1450 (1969).

69. H. A. Mook, J. W. Lynn and R. M. Nicklow, Phys. Rev. Lett. 30, 556 (1973).

70. J. F. Cooke, Phys. Rev. B 7, 1108 (1973).

71. J. F. Cooke and H. L. Davis, AIP Conf. Proc. No. 10, 1218 (1972).

72. See the review by E. D. Thompson, Adv. Phys. 14, 213 (1965), and also Ref. 1.

73. J. C. Slater, Phys. Rev. 52, 198 (1937); C. Herring and C. Kittel, Phys. Rev. 81, 869 (1951); Ref. 1.

74. C. Herring, Phys. Rev. 87, 60 (1952).

75. T. Izuyama, D. Kim and R. Kubo, J. Phys. Soc. Japan 18, 1025 (1963).

76. H. E. Stanley, Introduction to Phase Transitions and Critical Phenomena, (Oxford Press, New York, 1971); M. R. Bhagavan and C. Blomberg, J. Phys. C 6, 2882 (1973) and references therein.

77. S. W. Lovesey and C. G. Windsor, Phys. Rev. B 4, 3048 (1971).

78. A thorough discussion of thermal neutron scattering, with particular attention to itinerant electron systems, is given by W. Marshall and S. W. Lovesey, Ref. 30; see also Refs. 66, 70 and 75; J. B. Sokoloff, Phys. Rev. 180, 613 (1969).

79. Yu. A. Izyumov, Sov. Phys. U.S.P. 16, 359 (1963).

80. P. O. Löwdin, J. Chem. Phys. 18, 365 (1950).

81. E. D. Thompson and H. A. Mook, J. Appl. Phys. 41, 1227 (1970).

82. J. C. Slater and G. F. Koster, Phys. Rev. 94, 1498 (1954).

83. G. Gilat and L. J. Raubenheimer, Phys. Rev. 144, 390 (1966).

84. J. H. Wood, Phys. Rev. 126, 517 (1962).

85. G. F. Koster, in Solid State Physics, ed. by F. Seitz and D. Turnbull (Academic, New York, 1957) Vol. 5, p. 173.

86. M. K. Wilkinson, H. G. Smith, W. C. Koehler, R. M. Nicklow and R. M. Moon, in Neutron Inelastic Scattering (IAEA, Vienna, 1968), Vol. II, p. 253.

87. M. J. Cooper and R. Nathans, Acta Cryst. 23, 357 (1967).

88. B. N. Brockhouse, L. N. Becka, K. P. Rao and A. D. B. Woods, in Second Symposium on Inelastic Scattering of Neutrons in Solids and Liquids (IAEA, Vienna, 1963), Vol. II, p. 23.

89. M. Hansen, Constitution of Binary Alloys, 2nd edition.

90. E. Frikkee, Phys. Lett. 34A, 23 (1971); Ph.D. Thesis (unpublished).

91. H. A. Mook, J. W. Lynn and R. M. Nicklow, AIP Conf. Proc. (to be published); J. W. Lynn, Bull. Am. Phys. Soc. 19, 231 (1974).

92. R. J. Birgeneau, J. Cordes, G. Dolling, and A. D. B. Woods, Phys. Rev. 136, A1359 (1964).

93. L. C. Bartel, Phys. Rev. B 8, 5316 (1973); J. B. Sokoloff, Phys. Rev. Lett. 31, 1417 (1973); B. H. Brandow, Bull. Am. Phys. Soc. 19, 370 (1974).

94. R. Nathans, F. Menzinger and S. J. Pickart, J. Appl. Phys. 39, 1237 (1968).

95. S. K. Sinha, S. H. Liu, L. D. Muhlestein and N. Wakabayashi, Phys. Rev. Lett. 23, 311 (1969).

96. P. A. Fleury, Phys. Rev. 180, 591 (1969).

97. J. Skalyo, Jr., G. Shirane, R. J. Birgeneau and H. J. Guggenheim, Phys. Rev. Lett. 23, 1394 (1969).

98. P. A. Fleury and H. J. Guggenheim, Phys. Rev. Lett. 24, 1346 (1970).

99. M. P. Schulhof, R. Nathans, P. Heller and A. Linz, Phys. Rev. B 4, 2254 (1971).

100. M. J. Hutchings, G. Shirane, R. J. Birgeneau and S. L. Holt, Phys. Rev. B 5, 1999 (1972).

101. C. S. Glinka, L. Passell and V. J. Minkiewicz, AIP Conf. Proc. (to be published).

102. H. R. Child and R. M. Nicklow, Bull. Am. Phys. Soc. 19, 206 (1974).

103. R. M. Nicklow (private communication).

104. J. R. D. Copley and J. M. Rowe, Phys. Rev. Lett. 32, 49 (1974).

105. M. B. Stearns, Phys. Rev. B 8, 4383 (1973).

VITA

Jeffrey Whidden Lynn was born in Hackensack, New Jersey, on March 2, 1947. He attended public schools in New Rochelle, New York, and Sarasota, Florida, and graduated from Sarasota High School in 1965. He entered the Georgia Institute of Technology in 1965, and received the degree of Bachelor of Science in Physics in 1969. He entered graduate school at the Georgia Institute of Technology in 1969, and received the degree of Master of Science in Physics in 1970. He then received an Oak Ridge Associated Universities Graduate Participantship to carry out his thesis research at the Oak Ridge National Laboratory, and received the degree of Doctor of Philosophy in Physics in June 1974. He is a member of the American Physical Society and the American Institute of Physics. He married the former Miss Linda Mayo of Sarasota, Florida, and they now have two children.